INVESTIGATIONS OF 2D MATERIALS TOWARDS THZ SOURCE AND DETECTOR APPLICATIONS

A THESIS SUBMITTED TO
THE GRADUATE SCHOOL OF NATURAL AND APPLIED SCIENCES
OF
MIDDLE EAST TECHNICAL UNIVERSITY

BY

YUSUF SAMET AYTEKIN

IN PARTIAL FULFILLMENT OF THE REQUIREMENTS
FOR
THE DEGREE OF DOCTOR OF PHILOSOPHY
IN
CHEMISTRY

MARCH 2024

Approval of the thesis:

INVESTIGATIONS OF 2D MATERIALS TOWARDS THZ SOURCE AND DETECTOR APPLICATIONS

submitted by **YUSUF SAMET AYTEKIN** in partial fulfillment of the requirements for the degree of Doctor of Philosophy i**n** Chemistry**, Middle East Technical University** by,

Prof. Dr. Naci Emre Altun
Dean, **Graduate School of Natural and Applied Sciences** _____

Prof. Dr. Ali Çırpan
Head of the Department, **Chemistry** _____

Prof. Dr. Okan Esentürk
Supervisor, **Chemistry, METU** _____

Examining Committee Members:

Prof. Dr. İrem Erel Göktepe
Chemistry, METU _____

Prof. Dr. Okan Esentürk
Chemistry, METU _____

Prof. Dr. Hakan Altan
Physics, METU _____

Prof. Dr. Halime Gül Yağlıoğlu
Physical Engineering, Ankara University _____

Prof. Dr. Seha Tirkeş
Chemical Engineering, Atılım University _____

Date: 08.03.2024

I hereby declare that all information in this document has been obtained and presented in accordance with academic rules and ethical conduct. I also declare that, as required by these rules and conduct, I have fully cited and referenced all material and results that are not original to this work.

Name Last name : Yusuf Samet Aytekin

Signature :

ABSTRACT

INVESTIGATIONS OF 2D MATERIALS TOWARDS THZ SOURCE AND DETECTOR APPLICATIONS

Aytekin, Yusuf Samet
Doctor of Philosophy, Chemistry
Supervisor : Prof. Dr. Okan Esentürk

March 2024, 169 pages

The work investigates static and dynamic properties of 2D materials, graphene to transition metal dichalcogenides, for their possible use as a Terahertz source or detector. The static properties in THz domain were carried out with Time-Domain THz Spectroscopy (THz-TDS), while dynamic properties were investigated via Time-Resolved Terahertz Spectroscopy (TRTS) systems. The initial part of the studies was optimization of the terahertz systems thus after the optimizations the bandwıdth was expanded and S/N have been improved at maximum terahertz amplitude. The systems were used to measure the static and dynamic properties of 2D materials. The single-layer graphene (SLG) on various substrates were monitored to check the polymer substrates and growth/transfer effects on graphene. The multilayer graphene (MLG) samples on polymer and quartz substrates were investigated. Finally, the transition metal dichalcogenide samples were also analysed. The investigation of the static properties of the samples and the substrates showed low insertion losses for polymers compared to semiconductor or quartz substrates. The dynamic responses of SLG samples on polymer substrates showed a

metallic-like property, as fast initial rise (carrier generation and quick decay of the observed THz response. Unlike the SLG on polymer samples, the SLG grown/transferred on semiconducting samples revealed a rather weak response dominated by the substrate responses making the extraction of graphene response rather difficult. MLG samples, however, showed an increased THz photoconductivity upon optical excitation with 400nm and 800nm light. TMDC samples of $MoSe_2$/$PtSe_2$ and WSe_2 were studied for their THz conductivity properties as a high mobility candidate for plasmon resonance amplification of terahertz radiation. The responses of both samples upon optical excitation with 400nm adn 800nm light showed a fast initial rise and very fast decay for their potential use as high-speed applications requiring fast and reliable switching.

Keywords: 2D materials, Transition Metal Dichalcogenides, Graphene, Time-Resolved Terahertz Spectroscopy, Optical Pump Terahertz Probe Spectroscopy

ÖZ

2D MATERYALLERİN TERAHERTZ KAYNAK VE DEDEKTÖR UYGULAMALARINA YÖNELİK İNCELENMESİ

Aytekin, Yusuf Samet
Doktora, Kimya
Tez Yöneticisi: Prof. Dr. Okan Esentürk

Mart 2024, 169 sayfa

Bu çalışma grafenden geçiş metali dikalkojenlerine kadar çeşitli 2 boyutlu (2B) malzemelerin Terahertz kaynak ve dedektör olma potansiyellerini araştırmıştır. Zamana dayalı durağan özellikler Terahertz Zamana Dayalı Spektroskopisi (THz-ZDS) yardımıyla incelenirken dinamik özellikler Zaman Çözülümlü Terahertz Spektroskopisi (ZÇTS) sistemiyle incelenmiştir. Çalışmanın ilk kısmı THz-ZDS ve ZÇTS sistemlerinin optimizasyonuyla ilgilenmiştir ve optimizasyon sonucunda bant aralığı artırılıp maksimum terahertz genliğinde S/N oranı geliştirilmiştir. Optimize edilen sistemler 2B malzemelerin durağan ve dinamik özelliklerini incelemede kullanılmıştır. Birinci örnek setinde çeşitli polimer ve yarı-iletken alttaşlarda kaplı tek katmanlı grafenlerde (TKG) alttaşın ve transfer işleminin etkileri incelenmiştir. Ikinci set örnekler ise polimer ve kuvars üzerine transfer edilmiş çok katmanlı grafen (ÇKG) örnekleridir. Son örnek seti ise geçiş metali dikalkojen (GMD) örnekleridir.

Grafen örneklerinin durağan özellikleri polimer alttaşlar için diğer yarıiletken ve kuvars alttaşlara kıyasla daha düşük eklenme kaybı vermiştir. Polimer üzerindeki TKG örneklerinin dinamik özellikleri hızlı yükselme ve sönümlenme zamanına

sahiptir. Polimer alttaşlı TKG örneklerinden farklı olarak yarıiletken alttaşlı TKG örnekleri daha zayıf ve çoğunlukla alttaş tepkisi tarafından baskılanmış bir sinyal tepkisi vermiştir ki, bu da salt TKG tepkisini izole elde etmeyi oldukça zorlaştırmıştır. Diğer yandan ÇKG örnekleri 400nm ve 800nm optik uyarılmaya bağlı olarak THz iletkenliğinde bir artış göstermiştir. Oluşan taşıyıcıların sönümlenme süreleri incelendiğinde uzun ömürlü oldukları tespit edilip ortalama ömürlerinin 500ps'den fazla olduğu gözlemlenmiştir. Mika alttaş üzerindeki GMD örnekleri ise iyi mobilite özellikleri olduğundan ve terahertz ışığının plazmon rezonans yükseltilmesinde kullanılmak üzere iyi aday olduklarından THz iletkenlik özellikleri çalışılmıştır. Örnekler yine 400nm ve 800nm ışık ile optik olarak uyarılmışlardır. Her iki örnek de uyarılma sonrası çok hızlı yükselme ve çok hızlı sönümlenme göstermiştir. Bu örnekler de yüksek hızla değiştirme gerektiren uygulamalarda kullanılmaya uygundur.

Anahtar Kelimeler: 2D malzemeler, Geçiş Metal Dikalkojenleri, Grafen, Zaman Çözülümlü Terahertz Spektroskopisi, Optik Pompa Terahertz Belirleme Spektrokopisi

Dedicated to my Beloved Parents

ACKNOWLEDGMENTS

First and foremost, I am extremely grateful to my Ph.D. and master's supervisor, Prof. Dr. Okan Esentürk, for all of his support, advice, and patience during this long journey. Through his countless hours of guidance in our laser lab, UNAM's laser lab, TARLA's laser lab, in his office, on the phone, while trekking in the METU campus or in the forest, I have benefited to a great extent both scientifically and personally. It has been a great opportunity and honor to learn about THz research from him and being part of our Laser Spectroscopy Research Group.

I would like to sincerely thank my Thesis Monitoring Committee members, Prof. Dr. Irem Erel Göktepe and Prof. Dr. Seha Tirkeş, for their invaluable support, understanding, encouragement, and insightful comments throughout this journey.

I am very thankful to the TARLA administration and especially to Prof. Dr. H. Gül Yağlıoğlu for her valuable effort to move our THz system into the TARLA facility and her endless support during my studies over there. I am also thankful to her Ph.D. students, F. Gülşah Akça and especially E. Uzay Karakaya, for their friendship, support, and understanding. Owing to Uzay's endeavor to increase the output power and stability of the amplified laser system, I managed to expand our THz system's signal capabilities even further.

I would like to express my sincere gratitude to Prof. Dr. Hakan Altan, along with Prof. Dr. Okan Esentürk, for his valuable scientific and personal support for getting me back on track.

I am very thankful to all of my friends, former and current LSG members especially M. Gencay Çelik, Ö. Ceren Hızal, Majid Akbar, Ali Ekber Karabağ, Elif Demir Arabacı, Şevkican Cevher, Mustafa Yaşa, Dilara Gündoğdu, Aslı Beyler Çiğil,

Bahar Atik Eroğlu, T. Orçun Şengöz, Asena Gürpınar, İrem Türker, Kerem Baydemir, Nazım M. Trabzon, Yasemin Ekiz, Duru Tosunoğlu, Şenel Yıldırım.

I am also grateful research group of Assoc. Prof. Dr. Seval Kinden from Eskişehir Teknik Üniversitesi, for Single Layer Graphene (SLG) on polymer samples, research group of Prof. Dr. Cem Çelebi from İzmir Yüksek Teknoloji Enstitüsü for SLG on SiC samples, research group of Prof. Dr. Coşkun Kocabaş from Ulusal Nanoteknoloji Araştırma Merkezi-Bilkent University for the multilayer graphene on polymer and quartz samples.

I gratefully acknowledge that part of this thesis has been funded by the European commission under the program of Horizon EIC Pathfinder Open 2022 PLASNANO project (101099552).

TABLE OF CONTENTS

LIST OF TABLES

LIST OF FIGURES

LIST OF ABBREVIATIONS

2D	Two dimensional
6G	Sixth generation
Al_2O_3	Sapphire
API	Active Pharmaceutical Ingredients
BBO	Beta Barium Borate
BP	Black phosphorus
CVD	Chemical Vapour Deposition
Far-IR	Far-infrared
EM	Electromagnetic
ESTÜ	Eskişehir Teknik Üniversitesi
EOS	Electro-optic sampling
GeS	Germanium Selenide
InSe	Indium Selenide
İYTE	İzmir Yüksek Teknoloji Enstitüsü
Laser	Light amplification by stimulated emission of radiation
LIA	Lock-in amplifier
MLG	Multilayer graphene
MRI	Magnetic resonance imaging
MoSe	Molybdenum Diselenide
NIR	Near-infrared

OPTP	optical pump terahertz probe
P3HT	Poly(3-hexylthiophene)
PDMS	Polydimethylsiloxane
PE	Polyethylene
PET	Polyethylene terephthalate
PMMA	Polymethylmethacrylate
PVC	Polyvinylchloride
PtSe	platinum diselenide
QWP	Quarter waveplate
SHG	Second-harmonic generation
SLG	Single layer graphene
Si/SiO_2	Silicon/Silicon Dioxide
S/N	Signal-to-Noise
TARLA	Turkish Accelerator and Radiation Laboratory
TAS	Transient Absorption Spectroscopy
THz	Terahertz
THz-TDS	Time-Domain THz Spectroscopy
Ti:Sa	Titanium: Sapphire
TMDC	Transition Metal Dichalgogenide
TOPAS	Commercial name for Optical Parametric Amplifier
TRTS	Time-Resolved Terahertz Spectroscopy

TPS	THz pulsed spectroscopy
UNAM	Ulusal Nanoteknoloji Araştırma Merkezi
UV-VIS	Ultraviolet - visible
vdWs	van der Waals
WSe_2	Tungsten /diselenide
ZnTe	Zinc telluride

LIST OF SYMBOLS

σ^{intra}	: intraband conductivity
e	:charge of the electron
ω	: radiation frequency
k_B	: Boltzmann constant
I	: imaginary number
$\hbar$	: reduced Planck's constant
T	: temperature
μ	: mobility
Γ	: dispersion rate
E_f	: Fermi energy
τ	: relaxation time
n_s	: surface electron concentration
v_F	: Fermi velocity

CHAPTER 1

INTRODUCTION

Two-dimensional (2D) materials have emerged as a cornerstone in the advancement of material science and technology, offering a plethora of unique and superior properties compared to their three-dimensional counterparts. The significance of 2D materials lies in their atomic thickness and their diverse range of characteristics, including exceptional electronic, optical, mechanical, and chemical behaviors.[1–3] For instance, graphene is renowned for its remarkable electrical conductivity and mechanical strength.[4] Beyond graphene, the family of 2D materials has expanded to include semiconductors like MoS_2, insulators like hexagonal boron nitride, and even materials with magnetic and superlubricity properties[1,2]. These materials have opened up new avenues in various applications, from high-performance electronics and spintronic devices to energy storage, catalysis, and even healthcare.[5–7] The ability to engineer van der Waals heterostructures by stacking different 2D materials has further multiplied their potential, leading to novel devices with functionalities unattainable with traditional materials.[4] Moreover, the ongoing development of synthesis and processing techniques promises to transition these materials from laboratory to real-world applications, marking a transformative period in the fields of nanotechnology and advanced materials.[3]

Two-dimensional (2D) materials have emerged as a cornerstone for advancements in terahertz (THz) science and technology due to their unique electronic and optical properties. The ability of 2D materials such as graphene, black phosphorus (BP), and transition metal dichalcogenides (TMDCs) to manipulate THz waves has opened up new possibilities for the development of devices in this frequency range, which is known for its potential in high-speed data transmission, non-invasive screening, and materials characterization.[8] In communications, higher bandwidths are in demand

with new interconnecting digital technologies in our daily lives, from fridges to the cars and environments we interact with. High-power THz sources will enable to map out defects in the composite rocket insulations, something that is not possible with other imaging techniques. In medicine, production line check or expiration check while the drug is in the box[9] is a necessity but requires high energy broadband THz radiation. The integration of 2D materials with metamaterials has further enhanced the dynamic modulation and manipulation of THz radiation, leading to innovative applications in THz photonics.[10] Moreover, the atomically thin nature of these materials, combined with their diverse electronic behaviors, makes them ideal for creating optoelectronic devices that can operate efficiently in the THz regime.[11,12] The development of THz modulators, detectors, and generators based on 2D materials is not only pushing the boundaries of current technology but also holds promise for future applications in wireless communications, such as 6G and beyond, as they offer solutions to the challenges of efficient transmission and detection of THz waves, and biomedical fields. [13–17] The unique properties of 2D materials like graphene and TMDCs are being explored for their potential to create novel high-frequency THz sources and detectors, which could be integral to the development of THz-band communications hardware. In health, on the other hand, the current application of THz imaging is limited due to the power of the THz source. An increase in the generated THz powers will enable imaging of the cancerous cells during the surgery. Therefore, the development of such high-power sources and sensitive detectors is critical.

In this study, our Terahertz spectroscopic systems were utilized to investigate the static and dynamic properties of 2D materials towards the development of new sources and detectors. Within this scope, the instruments available were modified to work with high-power laser systems available in the Turkish Accelerator and Radiation Laboratory (TARLA) and, most notably, to increase the signal-to-noise ratio. 2D materials ranging from graphene to TMDCs were analyzed for their dielectric properties and charge carrier properties suggesting their potential to be used as a Terahertz source or detector. The graphene samples were analyzed for their

THz carrier mobilities and decay dynamics to observe the carrier lifetime change for being single or multilayer and also the conductivity behavior of metallic like or not. The substrate effect on THz conductivity was also observed, whether polymeric, semiconductor, or quartz as a substrate. Another class of materials, the TMDCs, coated onto mica substrates, were also investigated for their THz conductivity properties along with their rise and decay times.

CHAPTER 2

LITERATURE REVIEW

2.1 Terahertz Spectroscopy

Terahertz (THz) spectroscopy is a scientific method that analyses the interaction between materials and electromagnetic radiation within the terahertz frequency range. This relatively new technique is utilized to explore the electromagnetic spectrum between the microwave and infrared regions, spanning from 0.1 to 10 THz, corresponding to wavelength range between 3 millimeters (3.33 cm^{-1}) to 30 micrometers (333 cm^{-1}). This portion of the electromagnetic spectrum is the home to a wide array of captivating and exceedingly intricate exchanges between THz radiation and substances in physical, chemical, and biological systems.[18] Generating and identifying electromagnetic radiation within the THz range has long time posed a persistent challenge stemming from technical complexities on the electromagnetic spectrum's electronic and optical parts.

The THz technique utilizes short-pulsed lasers with pulse durations ranging from approximately 100 to around 10 femtoseconds, introducing a novel aspect in generating and detecting THz pulses. This element sets THz studies apart from traditional far-infrared (far-IR) investigations.[19] The distinctive feature lies in conducting time-resolved far-IR studies with sub-picosecond temporal precision. On the contrary, conventional far-infrared sources such as arc lamps or globars emit continuous radiation. In contrast, pulsed sources like free electron lasers or synchrotrons usually generate far-IR pulses that endure for approximately 3 picoseconds or longer.[20] A noteworthy advantage of THz spectroscopy is its capability to measure the transient electric field directly, beyond the assessment of intensity alone.[21] While conventional far-IR techniques mainly present the frequency-dependent absorption coefficient without giving the refractive index

information, the THz technique yields valuable information about the amplitude and phase of each spectral component comprising the pulse. By using the amplitude and phase of the obtained electric field, one can extract the complex-valued permittivity of the sample without having to carry out a Kramers-Kronig analysis.[22] Conventional far-IR techniques mainly present the frequency-dependent absorption coefficient without giving the refractive index information.

THz spectroscopy is a technique that involves using far-infrared radiation, specifically in the terahertz (THz) frequency range, to obtain molecular spectral information. This part of the electromagnetic spectrum, which lies between the microwave and infrared regions, was previously difficult to access but has become increasingly exploitable due to technological advancements.[23] The technique is noninvasive and nonionizing, making it particularly suitable for various applications, including biomedical research. It has shown unprecedented sensing abilities, allowing for the study of biomolecules such as DNA/RNA, amino acids, proteins, and carbohydrates, as well as cells and tissues.[24] THz spectroscopy is also valuable in characterizing materials like semiconductors.[23] One of the methods used in THz spectroscopy is terahertz time-domain spectroscopy (THz-TDS), which measures the interaction of light and matter and thus provides information on absorption spectra and refractive indices of materials. These key properties then enable us to calculate the dielectric behavior of the materials in this range, providing insights into their valuable properties, including static conductivities. This method has been applied to nonpolar amorphous materials, including glasses, lubricating oils, and polymers.[25,26] In the pharmaceutical industry, THz pulsed spectroscopy (TPS) and THz pulsed imaging (TPI) have been used for various applications, such as the discrimination and quantification of polymorphs/hydrates, analysis of solid form transformation dynamics, qualitative and quantitative characterization of tablet coatings and also quantitative and qualitative analysis of Active Pharmaceutical Ingredients (API).[9,27] THz spectroscopy provides unique insights into intermolecular bonding and crystalline matter, making it an invaluable chemical science tool. Its transition from a technology developed by physicists and engineers to one used by chemists,

materials scientists, and biologists is facilitated by the increasing availability of commercial THz spectrometers.[28] Astronomy is another field in which THz spectroscopy makes an impact. It is used to observe spectral signatures of ions, atoms, and molecules that are crucial for understanding the composition and origin of the Solar System, the evolution of matter in our Galaxy, and the star formation history of galaxies.[29] In security and defense, THz spectroscopy has been recognized for its potential in the nondestructive and nonintrusive detection of explosives[30] and drugs. It can penetrate dielectrics such as clothing materials, plastics, and cardboard, allowing for personnel screening and through-container screening.[31,32] Lastly, terahertz technology has also been applied to detect proteins, with research focusing on protein conformational changes, molecular interactions, and quantitative analysis of protein content. Despite its potential, some challenges must be addressed to further its application in clinical settings.[33,34]

The application of THz-TDS extends beyond the list of examples given above. It has potentially vast applications across many fields because it provides detailed spectral information about materials. It is particularly useful for characterizing nonpolar amorphous materials, such as glasses, lubricating oils, gasoline, and polymers,[25,35] THz-TDS is emerging as a powerful tool for process monitoring and quality control in the food industry, offering non-destructive testing methods to ensure product safety and integrity.[36] The technique is also extensively used for analyzing solid samples, including those related to security, pharmaceuticals, dental sciences, biological samples, and polymers, with commercial instrumentation available for a broad range of applications.[26,37] In biological contexts, THz-TDS enables the non-invasive assessment of water content in samples such as tree leaves and pork muscles, providing high-accuracy measurements comparable to traditional gravimetric methods.[38] The spectroscopic characterization of gases, liquids, and solids in the terahertz frequency range is another area where THz-TDS excels, aiding in material identification and sensing.[39] Additionally, the technique has been refined for high precision through interferometry-aided systems, which is particularly useful in harsh environments.[40] THz-TDS has also been applied to study water vapor,

leading to highly accurate measurements of absorption cross sections.[41] The determination of optical constants and sample thickness has been enhanced by THz-TDS, allowing for fast and broadband measurements.[42] High-resolution spectroscopy is achievable with the development of terahertz waveguides, which are instrumental in obtaining fingerprint absorption spectra of molecular solids.[9,43] Lastly, THz-TDS has significant applications in security, such as mail inspection, where it can detect materials concealed by opaque objects.[44]

Time-resolved THz Spectroscopy (TRTS) is an advanced version of THz-TDS and is an excellent technique for measuring non-equilibrium phenomena involving a third beam path for optical pump arm obtained from the same or different laser sources. Charge carriers are generated when a femtosecond optical pulse is applied to the sample. The charge carriers dynamics could be traced with ps time resolution by changing the time delay between the optical and THz pulses. The pulses coincide in space by varying relative pump-probe times providing information about generation process of carriers in time scale, as well as their decay dynamics such as cooling behaviors, trapping, and recombination.[45–47] Additionally, the dynamics of quasiparticles such as excitons can also be studied using this technique.[48,49]

TRTS is an analysis technique for photoinduced conductivity with sub-picosecond time resolution at low electric fields (kV/cm).[21] The system's time resolution is a unique property that provides unique information about the carrier evolution properties of samples upon optical excitation. Although conventional pump-probe analysis techniques are known for their high time resolution, they are limited in their ability to provide insight into the transport mechanisms of charge. These techniques can only detect the occupation of probed states and do not offer any fingerprint information regarding the underlying charge transport mechanisms. Therefore, it is important to consider alternative methods that can provide a more comprehensive understanding of charge transport processes..[50] The acquisition of transport mechanism data can be accomplished via two methods, namely time of flight or time-resolved microwave conductivity. Nevertheless, it is worth noting that the resolution

of these methods is in the order of nanoseconds..[51] Transient Stark Spectroscopy (TSS) is renowned for its high temporal resolution in picoseconds and sensitivity to transport properties. However, its reliance on high electric fields, in the range of megavolts per centimeter, can significantly influence charge mobility. Consequently, the technique has become less desirable in some applications..[52]

Recently, TRTS has become popular for studying the physical properties of semiconductor nanostructures such as nanowires,[53,54] and nanoparticles[55]. TRTS has a significant advantage in distinguishing between free and localized carriers, excitons, and surface plasmon resonances, each having a distinct photoconductivity signature.[49] However, creating Ohmic contacts for nanomaterials could be difficult due to their small size. This can affect electrical measurements.[56] It is essential to have a contact-free nature technique. By using the TRTS technique, it is possible to determine the THz probe wave based on the delay time between pump and probe..[57]

THz waves are commonly used to study the transient and ultra-fast photoconductivity and the charge carrier dynamics of different materials. Information about charge carriers' decay dynamics is crucial in developing various electronic and optoelectronic devices. THz waves also aid in investigating carrier behavior, which is essential in optimizing materials for multiple applications, including organic solar cells.[45,46].

2.2 Optical Rectification for Terahertz Generation

Optical rectification is a nonlinear process where an intense laser beam interacts with a second-order nonlinear crystal, inducing a polarization within the material. Unlike linear processes, where the resulting polarization is proportional to the incident electric field, optical rectification produces a polarization that is the difference of the individual frequencies involved in the interaction. In other words, it’s analogous to frequency doubling, but instead of summing the frequencies, we subtract them. Zinc telluride (ZnTe) is a zinc-blende crystal that exhibits strong second-order

susceptibility (χ^2). This property makes it suitable for optical rectification. When a high-intensity laser pulse interacts with ZnTe, it generates terahertz (THz) radiation through optical rectification. THz pulse energies were achieved using ZnTe crystals, contributing to advancements in time-domain spectroscopy, imaging, and more. [58]

2.3 Electro-optic Sampling For Terahertz Detection

Electro-optic sampling is a powerful technique employed to measure ultrafast electrical signals in the time domain. The fundamental principle involves the interaction of an intense laser pulse with a material (such as ZnTe). The material exhibits the electro-optic effect, wherein its refractive index changes in response to an applied electric field. We can detect these refractive index changes by probing the laser pulse with a second, delayed laser beam. Essentially, this process converts the temporal information of the electrical signal into spatial information that we can measure optically. ZnTe is optically isotropic under vanishing fields. However, when subjected to a strong electric field, ZnTe becomes birefringent, thanks to the electro-optic effect. This unique property makes ZnTe an excellent candidate for electro-optic sampling.[59]

2.4 2D Thin Films

Two-dimensional (2D) materials are characterized by their atomic thickness and absence of dangling bonds on the surface.[60] These materials exhibit unique properties, such as predominant quantum effects with confinement due to losing one dimension. Thus, they are highly promising materials for various optics, electronics, magnetics, and mechanics applications.[61] The development of 2D materials is anticipated to enhance current device technology, with their novel transport and topological properties offering opportunities for advancements in spintronic devices and quantum computing.[62] Additionally, 2D materials have attracted significant

research interest in optical-electronic devices, catalysis, and solar-energy conversion due to their exceptional mechanical, optical, and electronic properties.[63] One exciting property of 2D materials is piezoelectricity, enabling energy conversion between electrical and mechanical forms.[64] The future outlook for 2D materials is optimistic, with discussions focusing on enhancing research and performance to broaden their applications in the electrical and electronics industries.[65] Overall, 2D materials represent a diverse and promising class of materials with a wide array of potential applications and properties that continue to be explored and developed.

The THz region has continued to gain interest due to the plethora of applications encompassing research interests across various engineering and basic science disciplines. The development of source and detector technologies has been crucial for the global THz market in areas such as security, health care, non-destructive testing, and material science, which so far has only been limited by the power and sensitivity of these technologies concerning manufacturing costs and ease of implementation. With the recent allocation of frequency bands up to 0.3 THz and the potential for the development of technologies based on all-electronic systems that utilize frequencies towards 1 THz, a recent surge is driving the need to develop better sources and detectors for communication technologies, which, as a market is expected to make exponential gains in the near future. The region from 0.5 to 3 THz, especially near the 1 THz band, is still referred to as a gap since the power of all electronic sources falls off rapidly within this range due to limitations in semiconductor devices.[20] Powerful all-electronic sources are needed to achieve the desired high bandwidth, especially for frequencies above 0.5 THz, where atmospheric water vapor's absorption is detrimental to long-distance applications.[41] 2D material-based devices can offer the necessary solution to bridge the gap in this frequency region.

2.5 2D Materials

Traditional semiconductors are approaching their physical limits, leading to further changes in the approaches to advanced electronics. Recently, 2D materials have offered unprecedented attributes that could make them viable for technologies based on bulk semiconductors. Graphene, a one-atom-thick planar sheet of honeycomb-structured 2D material, has attracted considerable attention due to its unique carrier transport and optical/terahertz properties.[66] Electrons in graphene hold a linear dispersion relation with zero bandgap, resulting in peculiar features such as massless relativistic Fermions with ultrafast transport[67] and negative-dynamic conductivity in the THz spectral range under optical and/or electrical pumping.[68] These attributes have contributed to the development of fast, switchable devices. One realization has been graphene-channel transistors with cutoff frequencies approaching the terahertz range[69]. In contrast, graphene photodetectors have demonstrated high-speed operation[70] in the mid-infrared range, extending down to the THz range.[71] Graphene plasmonic terahertz oscillators[72] and graphene terahertz lasers[68] have also been proposed and recently demonstrated.[73] THz modulators based on intraband absorption in graphene have also been demonstrated for the last decade.[74,75] On the other hand, novel two-dimensional (2D) layered semiconductors as alternatives to graphene have emerged in recent years due to their atomic thin property and, more importantly, the weak van der Waals (vdWs) force between the layers and the feasibility of transfer to an arbitrary substrate. This will enable a novel approach to building artificial vdWs heterostructures.[76]

2.6 Progress in 2D-based Material Electronics

Recent developments in 2D materials have opened up an exciting new area for investigations, which have shown that such materials can show similar or better performances when compared to graphene in these attributes above, making them novel media that can be used to detect THz waves.[77] Initial investigations focused

on transition metal dichalcogenides (TMDCs) have now expanded to other layered 2D materials (topological insulators – TIs, black phosphorous – BP, silicene, thin compound semiconductors – InSe, GeS, etc.). For THz purposes, particular attention should be given to 2D materials with high mobility, such as graphene and TMDCs. Various promising techniques have been proposed in manufacturing 2D materials, such as Molecular Beam epitaxy (also called vdW epitaxy), liquid exfoliation, or solution-based dispersion and vapor deposition.[76] The remarkable qualities of 2D layered materials, such as wide spectral coverage, high strength, and excellent flexibility, mean that these materials will have the potential to meet the amplification of THz waves for frequencies up to and beyond 1 THz.

Esenturk et al.[46] discuss the use of THz spectroscopy to measure the photoconductivity of high-mobility polymeric materials, focusing on the effects of various factors on the photoconductivity of P3HT polymers and highlighting the potential of THz spectroscopy as a rapid material screening approach. The study aims to correlate THz measurements with electrical device test values and emphasizes the benefits of THz spectroscopy for simplifying the testing of solution-processed devices before device fabrication. The methodology used in the study involved TRTS to measure the photoconductivity of high-mobility polymeric materials. The study successfully correlated photoinjected carrier mobility with P3HT molecular weight, observed a fourfold increase in mobility with increasing molecular weight, and investigated various factors affecting photoconductivity in P3HT films.

The most remarkable thing about graphene probably is that the electrons move with little over huge (submicron) distances. Whereas electronic properties of other materials are commonly described by quasi-particles that obey the Schrödinger equation, electron transport in graphene is different. It is governed by the Dirac equation so that the charge carriers in graphene mimic relativistic particles with zero rest mass. Graphene plasmons provide a suitable alternative to noble-metal plasmons since graphene is a very absorbent material that is used in studying plasmons. In

general, the optical properties of plasmons on graphene are relevant in many ways, similar to those of surface plasmons propagating on a dielectric-metal interface. Plasmons in graphene can be tuned due to the possibility of carrier density tuning in graphene by an applied electrical field, optical stimulation, or chemical doping. Current graphene plasmon applications include frequency modulators, efficient photocells, sensors, and displays [78–81]. They are seen as a probable successor to liquid crystals due to the speed of graphene's response.[82] Recently, the use of graphene plasmons for THz light amplification has brought about a new era of device development.[83]

Single-layer graphene, a purely covalently bonded carbon in a honeycomb lattice, is actually a one-atom-thick layer that can be detached from graphite and/or grown by conventional chemical vapor deposition (CVD) methods. The layers are extremely strong in tension and can bend very easily without cracking. They are notably good conductors of heat and electricity. To the first approximation, graphene is *intrinsically a semi-metal* with a zero bandgap. The Fermi energy level is located at the intersection of conduction and valence bands located at the charge neutral point or the Dirac point and can be shifted in pure material to make it p- or n-type by an electric field or by chemical doping. The Fermi velocity, vF, is approximately 1.0 m/s for all carriers within a few tenths of an electron-volt (eV) of the neutral point energy.[84] CVD-grown graphene mobility has improved, and by using an optimized transfer process that allows the reuse of the copper substrate for the CVD growth devices with mobilities as high as 350,000 cm^2/Vs can be realized.[85]

Dawlaty et al. [86] discuss measuring carrier relaxation times in epitaxial graphene layers, highlighting two distinct time scales in the relaxation of photogenerated carriers and comparing the properties of epitaxially grown graphene to bulk graphite and single-layer graphene. A model is proposed to explain the observed transmissivity transients. The methodology involved using ultrafast optical pump-probe spectroscopy to measure carrier relaxation times in epitaxial graphene layers grown on SiC wafers. Epitaxial graphene samples were grown on semi-insulating

6H-SiC wafers, and a Ti: sapphire mode-locked laser was used for the spectroscopic measurements. They point out that the relaxation of nonequilibrium photogenerated carriers in epitaxial graphene layers occurs in two distinct time scales: a fast relaxation transient in the 70–120fs range and a slower relaxation process in the 0.4–1.7ps range with the slower relaxation time is influenced by the degree of crystalline disorder in the graphene layers. Also, the measured fast and slow time constants are attributed to specific carrier-carrier and carrier-phonon scattering processes in graphene.

Strait et al. [87] discuss the relaxation dynamics of photoexcited carriers in graphene at different substrate temperatures, attributing the observed transients to carrier cooling via phonon emission with a model that aligns with experimental observations and emphasizes the importance of understanding relaxation dynamics over longer time scales. The differential THz transmission transients show long relaxation times at low temperatures, attributing the slow cooling at low temperatures to inefficient intraband and interband scattering of carriers via optical phonon emission.

Zhou et al. [88] demonstrate a method using reflection-mode THz time-domain spectroscopy to accurately determine the conductivity of graphene on thin-film polymer substrates, with results validated by transmission-mode measurements, showing strong non-linear conductivity suppression under high incident THz electrical field strengths. The paper also discusses the potential of graphene in electronics and the challenges in measuring its electrical properties. The study emphasizes the potential of graphene for next-generation electronics and the necessity for improved measurement techniques. Also, the air-plasma-based THz-TDS method enhances accuracy in phase correction and enables quantitative extraction of graphene's electrical properties.

Mics et al. [89] discuss how ultrafast charge transport in graphene is determined by a thermodynamic balance within the graphene electronic system, converting electric field energy into thermal energy of the charge carrier population, impacting the conductivity properties of graphene. They used nonlinear ultrafast THz spectroscopy

for conductivity sampling, characterizing the graphene sample, analyzing experimental results, examining thermal distribution functions, and applying equations to describe conductivity spectra and calculate electron heating efficiency. A thermodynamic balance within the electronic system determines the charge transport in graphene on an ultrafast timescale, acting as a thermalized electron gas. The conductivity of graphene on this timescale is defined by the interplay between the heating and cooling of the electron gas, dependent on the dynamics and strength of the applied electric fields. The efficiency of energy transfer from ultrafast electric fields to electron heat in graphene can be quantified, showing the power absorption of graphene as a function of peak THz electric field. The efficiency of energy transfer from ultrafast electric fields to electron heat of graphene, the high-energy tail of the hot-carrier distribution extending to energies well above the Fermi level of graphene at 300 K.

Cinquanta et al.[90] In this study, Cinquanta provides a comprehensive overview of the ultrafast response of 2D materials at THz frequencies. The study highlights the unique properties of these materials and their potential for use in nano-electronic and nano-photonic devices. The experimental methods used for investigating the ultrafast response of 2D materials in the THz range are also discussed, providing valuable insights into the underlying physics. The study reviews the THz ultrafast signatures of charge carriers and exciton dynamics in a range of 2D materials, including graphene, TMDs, and 2D perovskites. This analysis sheds light on the mechanisms that govern the ultrafast response of these materials, and provides crucial information for the development of future electronic and photonic devices. It discusses the emerging tools for characterizing ultrafast THz dynamics at the nanoscale. Electron or hole relaxation mainly involves nonradiative electron-electron scatterings, depending on the excitation energy. Electron-electron interaction dominates at high energy, redistributes the electrical or optical power within the electron gas, and builds up a hot carrier population. Electron-phonon interaction operates on a longer time scale to equilibrate the electron and phonon temperatures and to cool the hot carriers. The hot carrier dynamics in heavily doped

graphene on polyethylene terephthalate (PET) substrate are less sensitive to the substrate's extrinsically charged impurity and surface polar phonons. The electron-optical phonon interactions dominate them. Graphene has demonstrated an exceptional ability to respond rapidly to terahertz (THz) driving fields, which is attributed to its interaction with mass-less Dirac electrons. This interaction results in a non-linear response via intraband conductivity. The cooling dynamics of hot charge carriers in graphene have been extensively investigated, leading to the development of a range of THz applications, such as broadband detection, THz modulation, and saturable absorption for pulse generation. These unique properties of graphene make it an attractive material for THz applications in various fields, including communication, sensing, and imaging. Graphene's remarkable features pave the way for the development of new and innovative technologies in the future. The study of the ultrafast thermalization of photoexcited undoped graphene has revealed the effectiveness of the collective response of Dirac electrons in converting THz fields into electronic heat. This results in strong THz nonlinearities across a broad range, which can be utilized for nonlinear wave conversion and efficient THz high harmonics generation. These findings highlight the adjustability of graphene's ultrafast response, which is ultimately limited by the strong coupling of the hot electrons to graphene optical phonons.

2.7 Terahertz Conductivity, Mobility, and Scattering Time

The intraband and interband electronic transitions are intrinsic mechanisms behind the broadband optical absorption of graphene.

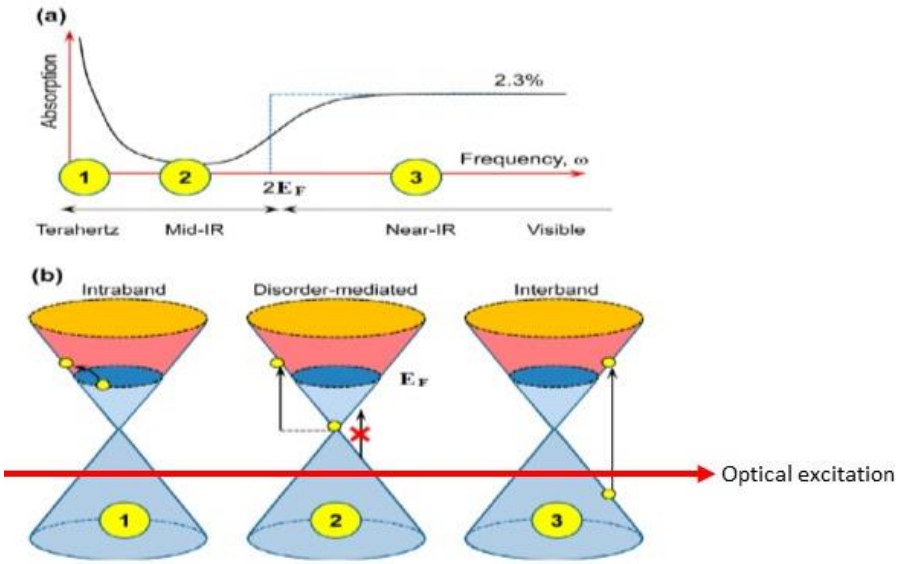

Figure 2.1. (a) The absorption spectrum of graphene at finite doping (b) Optical transition processes, namely intraband, disorder-mediated, and interband transition [adapted from 79].

Figure 2.1 shows the conductivity and excitation properties of Graphene in different parts of the electromagnetic spectrum. Figure 2.1(a) represents the characteristic absorption spectrum of graphene at finite doping. It has characteristic features such as a Drude peak at THz frequencies, minimal absorption in the mid-infrared frequencies due to Pauli blocking, and a transition to the universal 4% insertion loss beyond the far-infrared. On the other hand, Figure 2.1(b) reveals the various optical transition processes. Transitions occur via intraband processes at a small ω less than the thermal energy. At finite $\omega < 2 E_F$, disorder plays an important role in imparting the momentum for the optical transition. A transition occurs around $\omega \approx 2 E_F$, where direct interband processes lead to a universal 4% insertion loss.[79]

The conductivity of graphene is derived from the Kubo formula in the literature.[91,92] For the linear response of graphene to a uniform external electric field, the intraband conductivity contribution significant for the THz range given as a function of temperature, T, is provided by (in various notations)[93]:

$$\sigma^{intra}(\omega) = i\frac{2Te^2 \ln\left[2\cosh\left(\frac{E_F}{2T}\right)\right]}{\pi\hbar^2\omega\left[1+\frac{i}{\omega\tau}\right]} \quad (1a)$$

$$\text{or} \quad \sigma^{intra}(\omega) = i\frac{2e^2}{\pi\hbar^2}\frac{k_BT}{\omega+i\Gamma}\ln\{2\left[1+\cosh\left(\frac{\mu_c}{k_BT}\right)\right]\} \quad (1b)$$

where σ^{intra}: intraband conductivity; e: charge of the electron; ω: radiation frequency; k_B: Boltzmann constant; i: imaginary number; $\hbar$: reduced Planck's constant; T: temperature; μ: mobility; Γ: dispersion rate

Which can also be written as

$$\sigma^{intra}(\omega) = i\frac{2e^2}{\pi\hbar^2}\frac{k_BT}{\omega+i\Gamma}\left[\frac{E_f}{2k_BT} + \ln\left(1+e^{-\frac{E_f}{k_BT}}\right)\right] \quad (2)$$

where E_f: Fermi energy or chemical potential

In the semi-classical limit, where $E_F >> k_bT$

$$\sigma(\omega) = \frac{e^2E_F}{\pi\hbar^2}\frac{i}{\omega+i\tau^{-1}} \quad (3)$$

where τ: relaxation time

graphene surface electron concentration, n_s depends on the Fermi level energy, E_F (from now on, this energy is denoted as Fermi level)

$$n_s = \frac{E_F^2}{\pi v_F^2\hbar^2} \quad (4)$$

where v_F: Fermi velocity

and, since

$$\mu = \frac{ev_F^2\tau_m}{E_F} \quad (5)$$

and since the optical conductivity of graphene depends on the electron relaxation time τ, whereby the τ value is estimated from the DC mobility, μ

$$\tau = \frac{\mu \hbar \sqrt{\pi n_s}}{e\, v_F} \quad (6)$$

Fermi level increase from 0.1 eV to 0.5 eV leads to a τ value increase from 0.1 ps to 0.5 ps.

For having high-power THz sources and sensitive detectors, the 2D materials need to be studied for their charge carrier properties. These properties correspond to ultrafast phenomena with lifetimes in the order of ps or even shorter. They should be traced by an ultrafast technique for which TRTS suits the best for its unique properties. The technique powerfully combines the utilization of optical photoexcitation with ultrashort fs pulses for charge carrier generation by tracing the charge carriers whose interaction could be probed by THz light.

CHAPTER 3

EXPERIMENTAL

Our investigations employed two THz systems to analyze materials' static and dynamic properties. Since these systems are custom-built, we provide detailed descriptions and characteristics in this chapter. Both systems operate in transmission mode to ease the measurement and data processing. As part of her Ph.D. thesis study, the system was initially built at Ulusal Nanoteknoloji Araştırma Merkezi (UNAM) at Bilkent University by our previous lab member, Dr. Emine Kaya.[94]

During our studies, the adopted changes in UNAM for installing a previously inactive Optical Parametric Amplifier (TOPAS) resulted in an altered beam profile that caused an appreciable decrease of S/N to our system. Hence, we moved our THz system to the TARLA facility. We improved the system's overall performance for better analysis of our 2D material samples.

3.1 Laser systems

A laser is a highly sophisticated device that produces a beam of coherent light through an optical resonator and an amplification unit. The optical resonator comprises two parallel mirrors that reflect the light back and forth, amplifying it with each pass. On the other hand, the amplification unit is responsible for boosting the intensity of the light to compensate for any losses that may occur, such as light transmitted to the user. This amplification mechanism is known as "light amplification by stimulated emission of radiation," or LASER. The term "stimulated emission" refers to the process in which atoms or molecules are excited by an external energy source and then release that energy in the form of light with external stimuli. This process is repeated repeatedly within the laser,

resulting in the highly focused and powerful beam of light that we commonly associate with the technology.

Mode-locked Titanium: Sapphire (Ti:Sa) lasers are highly efficient, commercially available, and tunable lasers that use a lasing medium made of sapphire (Al_2O_3) crystal doped with Ti^{3+} ions. The Ti:Sa laser is a solid-state laser that uses a crystalline medium to amplify light instead of a gas or liquid medium. The Ti:Sa laser has become a popular choice for various applications, including medical, scientific, and industrial, due to its excellent performance and versatility. The Ti:Sa laser gets its name from using titanium (Ti) and sapphire (Sa) crystals. The Ti^{3+} ions are introduced into the sapphire crystal by doping, resulting in the ions' octahedral coordination. This process makes the sapphire crystal an excellent host for the Ti^{3+} ions, allowing for efficient lasing.

What makes Ti:Sa lasers unique is their solid-state active medium, which allows for extended operation time and compactness. Sapphire is an excellent lasing medium due to its high thermal conductivity, extraordinary chemical inertness, and mechanical resistance. The high thermal conductivity of sapphire ensures that the heat generated by the lasing process is efficiently dissipated, reducing the risk of thermal damage to the crystal. The extraordinary chemical inertness of sapphire makes it resistant to corrosion and chemical attack, ensuring that the laser's optical properties remain stable over time. Ti:Sa lasers can provide a broad light spectrum, extending the wavelength range over 400 nm between 670 and 1050 nm.[95] This makes them ideal for various applications, including spectroscopy, microscopy, and optical coherence tomography. Their tunable nature also makes them useful in ultrafast optics, where they generate ultrashort laser pulses for applications such as femtosecond laser surgery and micromachining. Therefore, Ti:Sa lasers are a precious tool in the field of optics, thanks to their solid-state active medium, efficiency, versatility, and tunability. Their ability to provide a broad spectrum of light makes them ideal for many different applications, and their compactness and reliability make them a popular choice for industrial and scientific uses.

In optical experiments, particularly pump-probe experiments, it is necessary to use laser-pulse energies much higher than those generated by the MHz oscillator mentioned earlier. The MHz oscillator pulses are amplified in another Ti:sapphire crystal to achieve more considerable pulse energies. To increase the energy per pulse, the MHz repetition rate of the oscillator must be reduced to the kHz range, where a thousand pulses share the total power instead of a million pulses. Therefore, pulse pickers, such as a Pockels cell, reduce the pulse repetition rate to the kHz range. The seed-laser pulses are temporally stretched before entering the amplification stage to ensure that the optical components are not damaged, and that undesired nonlinear effects are avoided. This technique helps to prevent high peak intensities that could cause damage or unwanted effects. Once the laser pulses are amplified several times, they are temporally compressed to ensure that they are of the desired length and intensity. Producing high-energy laser pulses involves multiple steps, including amplification and compression, and careful control of pulse repetition rates and peak intensities to ensure accurate and reliable results in optical experiments.

3.2 THz Spectroscopy Systems

Schemes of the experimental setup used for Terahertz Time-Domain Spectroscopy (THz-TDS) and Time-Resolved Terahertz Spectroscopy (TRTS) purposes are shown in Figure 3.1 and Figure 3.2. A Ti:sapphire regenerative amplifier (Spitfire ACE, Spectra-Physics/Newport) is used as a laser source of the experiment with 5 mJ pulse energy, 1 kHz repetition rate, ~ 60 fs pulse length, and central wavelength λ = ~800 nm. The primary beam is initially directed through 800 nm beam splitters, which divide it into three beams. Two of these beams are utilized for THz generation and detection, while the third beam is used for photoexcitation of the sample. The first two beams, the probing and sampling beams, have a pulse energy of approximately 0.6 mJ in total. These beams are responsible for generating and detecting THz radiation. The third beam, the pumping beam, has a remaining portion of around 0.5mJ and is used to excite the sample. Another option for the excitation wavelength is 400nm, produced

by a non-linear crystal, Beta-Barium Borate, which provides an output power of ~25 mW. The system is also purged by dry air to eliminate water vapor, diminishing the effect of THz light. The humidity was kept below 1% during an entire measurement course.

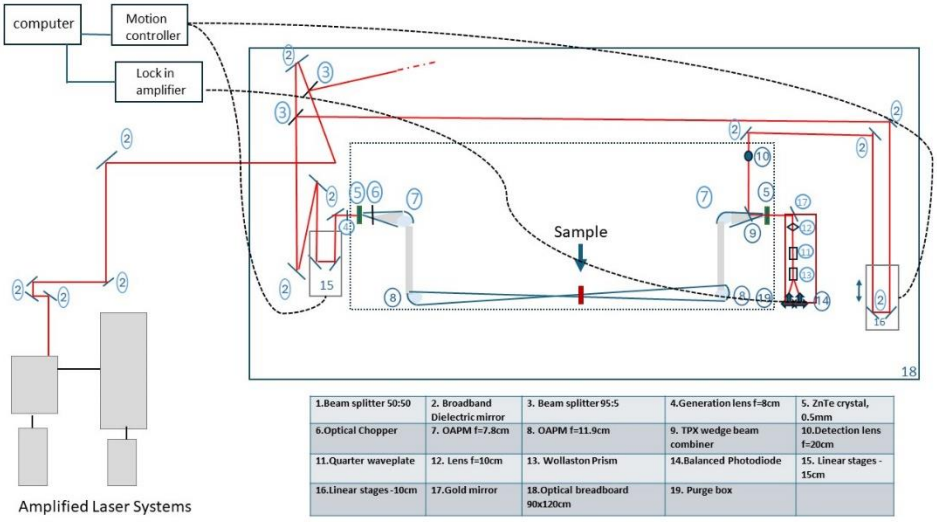

1.Beam splitter 50:50	2. Broadband Dielectric mirror	3. Beam splitter 95:5	4.Generation lens f=8cm	5. ZnTe crystal, 0.5mm
6.Optical Chopper	7. OAPM f=7.8cm	8. OAPM f=11.9cm	9. TPX wedge beam combiner	10.Detection lens f=20cm
11.Quarter waveplate	12. Lens f=10cm	13. Wollaston Prism	14.Balanced Photodiode	15. Linear stages - 15cm
16.Linear stages -10cm	17.Gold mirror	18.Optical breadboard 90x120cm	19. Purge box	

Figure 3.1. THz-TDS setup in TARLA

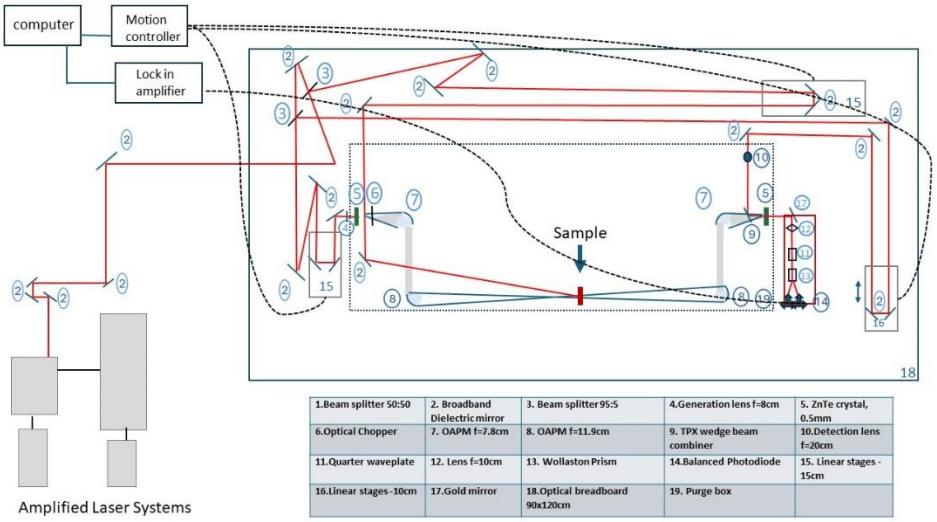

1.Beam splitter 50:50	2. Broadband Dielectric mirror	3. Beam splitter 95:5	4.Generation lens f=8cm	5. ZnTe crystal, 0.5mm
6.Optical Chopper	7. OAPM f=7.8cm	8. OAPM f=11.9cm	9. TPX wedge beam combiner	10.Detection lens f=20cm
11.Quarter waveplate	12. Lens f=10cm	13. Wollaston Prism	14.Balanced Photodiode	15. Linear stages - 15cm
16.Linear stages -10cm	17.Gold mirror	18.Optical breadboard 90x120cm	19. Purge box	

Figure 3.2. TRTS setup in TARLA

3.3 Samples

The samples had 3 types depending on their preparation method: CVD-grown and epitaxially grown ones.

3.3.1 CVD-grown samples

The first set of samples was received from Eskişehir Teknik Üniversitesi (ESTÜ). Those samples were single-layer samples on different polymer substrates. The graphene was first grown on Cu substrate and then transferred onto a variety of polymer substrates, namely Polydimethylsiloxane (PDMS), Polyethylene terephthalate (PET), and a blend of two different polymers, Polydimethylsiloxane (PDMS), and Polymethyl methacrylate (PMMA).

A second graphene sample was obtained commercially and formed by transferring the SLG layer on top of the Si/SiO_2 substrate.

Besides the SLG samples, a set of Multi-layer graphene samples were transferred onto quartz substrate, namely MLG850, MLG900, MLG950, and MLG1000. The numbers indicate the growth temperature related to the samples' thickness with the following layer numbers: MLG850 with 30 layers, MLG900 with 50 layers, MLG950 with 70 layers, and MLG1000 with 100 layers.

In addition to graphene, 2D samples were extended further with collaboration through the PlasNano project. Within this set, there were also 2 other samples of Transition Metal Dichalcogenide (TMDC) films directly grown on mica substrates. The first sample had 1 layer of $MoSe_2$ on the mica and 2 layers of $PtSe_2$ (code 2705) on the top. The second sample, on the other hand, contained 3 layers of WSe_2 (code 2706) on mica. The thicknesses were 150µm for mica reference, 170µm for 2705, and 90µm for 2706.

3.3.2 Epitaxially-Grown Samples

This set of samples was obtained from İzmir Yüksek Teknoloji Enstitüsü (İYTE). The samples were grown on 4-H SiC substrate from the Si side at high temperatures ~1500 °C. During graphene formation, Si atoms are removed, and an interface layer is formed that contains different phases of C and Si atoms. The graphene is formed on top of this layer. There were two samples of the same batch having similar properties as informed.

CHAPTER 4

TRTS SYSTEM OPTIMISATION STUDIES AND ADAPTATION TO TARLA ENVIRONMENT

The primary objective of this chapter is to optimize the THz system to achieve the highest Signal-to-Noise (S/N) ratio for sensitive measurements of 2D materials. To achieve this, we conducted thorough optimization studies, examining various parameters of the system components, including the chopper, detector, and lock-in amplifier. We performed multiple tests and measurements to determine the best possible settings for each element, allowing us to maximize the S/N ratio of the system. The optimization process involved carefully examining the system's components to choose the least sources of noise or interference. We tested different chopper frequencies, detector sensitivities, and lock-in amplifier settings to determine the optimal parameters for each component. Once we determined the optimal settings for the system, we used a known sample, Si/SiO_2, to establish the zero position for the pump-probe experiments. This step was essential to ensure the pump-probe experiments were accurate and reliable. We carefully measured the sample's properties and used this information to calibrate the system, ensuring our results were accurate and precise. Overall, our efforts to optimize the THz system and establish the zero position for the pump-probe experiments have been successful. We have achieved the highest possible S/N ratio for the system, and we are confident in the accuracy and reliability of our results. Our detailed optimization process ensures that the system is functioning optimally and that we are obtaining accurate and precise data.

4.1 Scan Parameters And Settings Study

Collecting data from a sample is a critical process in scientific research. The scanning parameters play a crucial role in obtaining the required data accurately and efficiently. The "step size" is the distance the scanning stage moves between two consecutive measurement points. The resolution of the data depends on the step size, as it determines the level of detail captured in the terahertz pulse profile, carrier lifetime, or dynamics. A smaller step size allows for higher resolution but requires more time to scan the sample. A larger step size leads to a lower resolution but can cover the sample more quickly. The "wait time" is the time between one step of the stage and the time for averaging data before the next step. This duration is crucial as it allows the terahertz signal to settle and stabilize before taking the subsequent measurement. A longer wait time leads to more stable and accurate data and increases the overall scan time. The step size and wait time determine the level of resolution, accuracy, and scan time. Therefore, it is essential to choose the appropriate parameters based on the sample's properties and the required level of detail and accuracy. Table 1 shows different scanning parameters for extraction of static and dynamic properties of materials studied after careful studies were done and measurements were compared for accurate and verified measurements achieved.

Table 1. Sampling parameters for extracting static and dynamic properties

	For Static properties	For Dynamic Properties
Step size	0.005mm	0.02mm for short scan, 1mm for long scan
Lock-in time constant	50 ms	50ms
Wait time	150ms	150ms

As presented in Table 1, the lock-in time constant and wait time are the same for static and dynamic properties. They are 50ms and 150ms, respectively. On the other

hand, the step size for static properties is 0.005mm, and 0.02mm is used to extract dynamic properties.

4.2 Detector Power Supply Settings Study

Electro-optic sampling (EOS) is a highly precise technique used to measure the evolution of electric fields in laser pulses with up to attosecond precision. This technique is extensively used in ultrafast science and solid-state physics to study electron phenomena in materials like metals, semiconductors, and insulators. By analyzing the change in polarization of a probe pulse, researchers can gain valuable insights into the behavior of electrons in these materials. This, in turn, can lead to the development of new materials and electronic devices. However, detecting THz fields that oscillate rapidly requires ultrafast detectors that are not currently available. In that sense, balanced photodetectors are essential in extending the detection range to shorter wavelengths in EOS. These photodetectors are designed to minimize common-mode noise in a detection system's signal and reference channels. The photodetectors operate based on the balanced bridge configuration, which involves connecting two identical photodiodes differentially. As both photodiodes receive the laser light simultaneously, the final output is the difference between their photocurrents. This arrangement cancels out common-mode noise, which in turn enhances the sensitivity of the photodetector.

The detector has different settings that affect its sensitivity depending on the intensity of the incoming laser light. These settings should be arranged appropriately to have an optimum S/N. Figure 4.1 shows the resultant THz signal profile changing with different detector settings. The obtained signals were calculated for their S/N by having the ratio of THz peak power and noise level average for 20-30 data, whose results are in Table 2. According to the results, the highest S/R is achieved when the detector power supply is off, the detector itself is off, and the detector amplifier is set at low reserve normal noise.

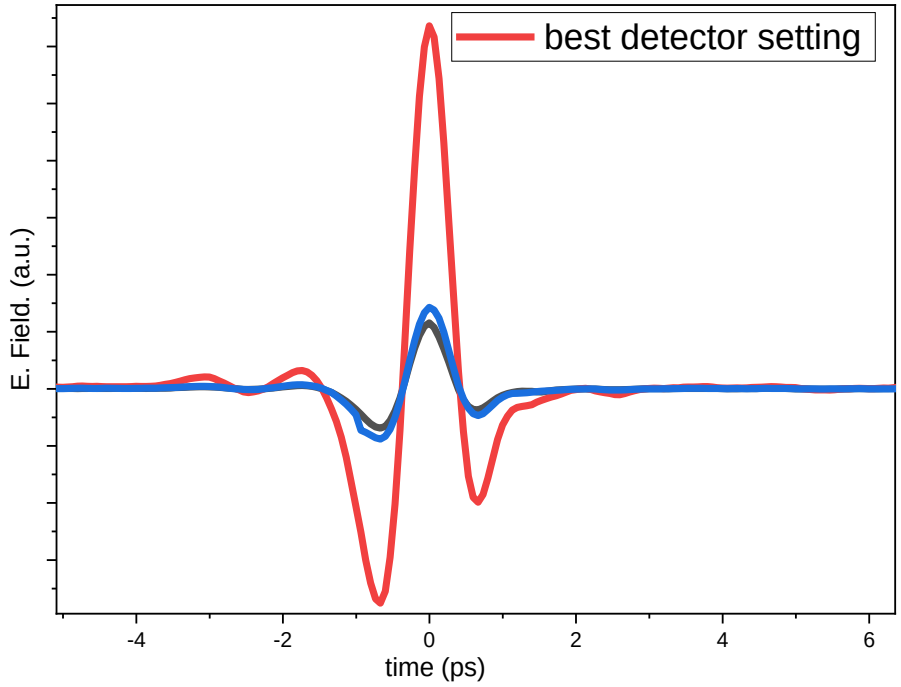

Figure 4.1. THz signal profile with different detector settings

Table 2 Calculated S/N for different detector settings

Setting	Peak THz signal	Std dev. of noise level	S/N
det pow supp on, det off, det amp low (reserve normal noise)	5.7×10^{-5}	2.6×10^{-7}	217
-det pow supp off, det off, det amp low (reserve normal noise)	3.1×10^{-4}	1.1×10^{-6}	294
-det pow sup on, det on, det amp low (reserve-low noise)	7.1×10^{-5}	2.4×10^{-7}	293.7

4.3 Chopper Phase Adjustment Study

Various optical chopper devices, such as laser beams, are available for interrupting and transmitting light beams mechanically. These devices are commonly used for periodically modulating a beam's optical power. Optical choppers are crucial in many applications, such as spectroscopy, optical communications, and laser ranging. The modulation of light energy is achieved by the periodic interposition of a rotating disk with alternating opaque and transparent sectors. The device is designed such that the opaque sectors block the light beam while the transparent sectors allow the light beam to pass through. The number of sectors on the disk and the rotational speed of the disk determines the modulation frequency of the chopper. It is worth noting that the choice of optical chopper device depends on the specific application requirements such as frequency response, power handling, and spectral range.

Our system uses a Thorlabs chopper with model number MC2000 having 10 slot chopper blades. The chopper phase setting was analyzed for causing the slightest noise. Figure 4.2 represents the peak THz amplitude fluctuations corresponding to different phase angles from 45 to 70°, and Table 3 gives the calculated standard deviation of the noise level. As the figure and the table suggest, the 45° resulted in the best S/N with the lowest noise of 4.2 x10^{-7}.

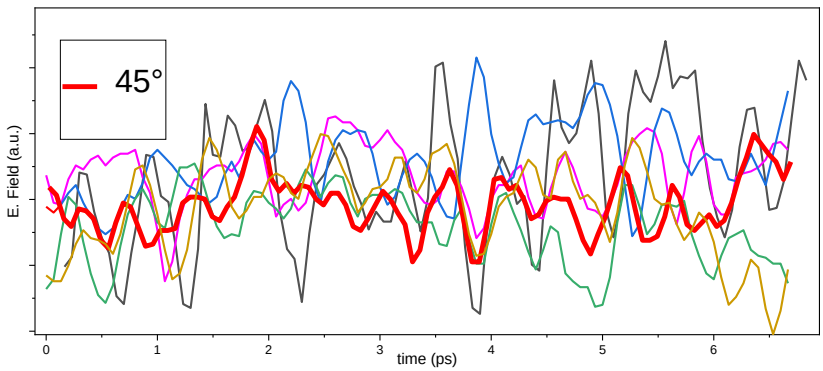

Figure 4.2. Phase settings of different rotation angles, giving the slightest noise at 45°

Table 3. The standard deviation for noise level

Chopper phase (°)	Std Dev. Of Noise Level
67	1.0×10^{-6}
60	4.8×10^{-7}
55	5.9×10^{-7}
52	6.9×10^{-7}
50	5.4×10^{-7}
45	4.2×10^{-7}

4.4 Quarter Waveplate Angle Study

To detect THz transients, the electro-optic sampler must first be accurately calibrated. The calibration process involves adjusting a quarter-wave plate to compensate for the equilibrium birefringence of the electro-optic medium. This equilibrium birefringence causes the near-infrared probe pulse to become elliptically polarised. If the probe pulse is passed through the Wollaston prism without first going through a compensation plate, it will result in a non-zero detector output. Therefore, the output voltage of the differential detector is closely monitored, and the quarter-wave plate is continually adjusted until the reading is as close to 0V as possible. This calibration ensures that the probe pulse becomes circularly polarised, meaning it has p and s components of equal magnitude after passing through the quarter-wave plate. This allows for accurate detection of THz transients.

QWP is placed onto the system with a special holder that can freely rotate in a plane orthogonal to the beam transmission direction. The angle should be arranged so that circular polarisation is obtained and each has equal intensity. We could understand this by changing the rotation angle differently and checking the signal with respect

to the noise level. Table 4 represents the QWP angle from 18-28° that tended to give the maximum signal amplitude and checked for the best S/N. As the table suggests, the maximum S/N was obtained at a 22-degree quarter angle, providing a max peak THz signal.

Table 4 QWP angle and S/N

Rotation Angle (°)	Peak amp of THz signal	Std dev. of noise	S/N
28	3.6×10^{-5}	5.2×10^{-7}	67
26	3.6×10^{-5}	5.1×10^{-7}	70
22	3.6×10^{-5}	4.6×10^{-7}	77
18	3.4×10^{-5}	4.6×10^{-7}	73

4.5 Lock-in Amplifier Settings Study

Lock-in amplifiers (LIA) use phase-sensitive detection to measure weak AC signals down to a few nanovolts, even in the presence of much larger noise sources. They work by selecting a specific reference frequency that matches the signal frequency of interest and rejecting any signals not in phase with the reference signal. Lock-in amplifiers are commonly used in scientific research, engineering, and medical diagnostics, particularly in experiments involving low-level signals such as magnetic resonance imaging (MRI) and optical spectroscopy. Its settings are also essential to achieve the best S/N, including time constant, signal input settings, and sensitivity.

4.5.1 Time constant

The time constant is a crucial parameter that determines the filter response time of a lock-in amplifier. It is a measure of how quickly the amplifier responds to changes

in the input signal. A long-time constant provides better noise rejection and a smoother output response. It averages the input signal over a more extended period, reducing the impact of noise and providing stable output readings. However, this also means that the response is slower to changes in the output signal. On the other hand, a short time constant gives a faster response to signal changes and reduced settling time. This means that the output signal tracks changes in the input signal more quickly, making it suitable for applications requiring fast response. However, the output signal also has an increased noise component due to the shorter averaging period. Choosing the right time constant for a lock-in amplifier involves balancing noise rejection and response speed. It depends on the nature of the input signal and the measurement requirements. It is essential to remember that a longer time constant is suitable for applications where signal stability is more critical than a fast response. A shorter time constant is appropriate for applications where speed is more important than noise rejection.

The time constant settings of 100 and 300 ms were measured to measure the best S/N. 6 measurements were done for the 100ms setting, and two measurements were done for the 300ms setting to make the conditions equal for both settings, whose results are available in Table 5. The resulting S/N turned out to be better for the 100 ms setting, which resulted in an S/N of 71, as presented in the table.

Table 5 Time constant settings

Setting	Peak amp of THz signal	Std dev. of noise level	S/N
time cst 100 ms, 300 ms wait time-6 average	3.6×10^{-5}	5.1×10^{-7}	71
time cst 300 ms, 600 ms wait time-2average	3.6×10^{-5}	5.4×10^{-7}	67

4.5.2 Signal Input Settings Study

Since Lock-in amplifiers (LIAs) are commonly used to detect weak signals buried in noise, electromagnetic interference can often compromise the accuracy and reliability of the signal obtained from LIAs. Proper grounding of the LIA can mitigate this issue by providing a low-resistance path for the current to flow to the ground. This helps to minimize the potential difference between different points of the circuit and reduce the overall noise in the signal. The grounding can also prevent the LIA from picking up unwanted environmental signals, such as radio waves or electrostatic discharges. Therefore, to ensure optimal performance of the LIA, it is essential to ground it properly.

Table 6 shows two signal input settings, float, and ground, for the best S/N calculated by the ratio peak THz signal and the standard deviation of that signal. Since TARLA has an isolated environment the ground signal resulted in better S/N as expected.

Table 6 Signal input settings

Setting	Peak THz signal	Std dev. of noise level	S/N
signal input- ground	3.6×10^{-5}	4.9×10^{-7}	74
signal input- float	3.6×10^{-5}	5.2×10^{-7}	70.8

4.5.3 Lock in Sensitivity Study

The Lock-In Amplifier (LIA) is a sensitive device that requires precise input signal level control to provide accurate measurements. The sensitivity setting is a critical

parameter determining the input signal level necessary to drive the LIA to full scale. It is essential to set the sensitivity correctly to ensure the LIA's proper functioning and accurate measurement results. If the sensitivity is set too high, the LIA may overload, resulting in a low full-scale voltage or current. This can lead to significant measurement errors and potential damage to the device. On the other hand, if the sensitivity is set too low, the full-scale voltage or current may be too high, resulting in suboptimal noise performance. This can compromise the accuracy and precision of the measurements. Therefore, choosing the optimal sensitivity level is crucial based on the input signal strength and the desired measurement accuracy. The sensitivity setting should be adjusted gradually, starting from a low value and increasing it until the signal level drives the LIA to full scale. Hence, in this part, noise analysis of the output signal and adjustment of the sensitivity are presented accordingly to achieve the best possible noise performance. As presented in Table 7, the sensitivity setting of 10 mV gave the slightest noise and the best S/N for the measured THz transient.

Table 7 Lock in sensitivity

Setting	Peak amp of THz signal	Std dev. of noise level	S/N
lock in 5 mV sens	3.5×10^{-5}	5.0×10^{-7}	70.1
lock in 10 mV sens	3.5×10^{-5}	4.9×10^{-7}	70.2
lock in 20 mV sens	3.5×10^{-5}	5.2×10^{-7}	67.7

4.6 400 nm Nonlinear Crystal Optimization Study

Beta Barium Borate (BBO) crystal is a popular nonlinear optical crystal used for Second-harmonic generation (SHG), also known as frequency doubling.[96] In our system, the crystal generates an alternative pump color at 400nm using 800nm laser

pulses. Upon installation of these crystals, one should be careful about the fluence of laser light and the damage threshold of these crystals, which are in the order of 0.3 J/cm^2.[97] Also, after installation of the crystal, to acquire maximum conversion efficiency together with suitable fluence, one should consider the angle of the crystal with respect to both normal angle and rotary angle. Particularly in our system, the power reached for the 400 nm light is ca 25 mW after optimizations.

4.7 Setting up a Beam Expander for Low Beam Size and Producing More 400 nm Light

The initial part of the studies was carried out at UNAM. In the middle of our studies, the laser parameters and beam direction were required to be changed after the TOPAS equipment was installed to have light in the UV-VIS range of the EM spectrum. The equipment installation resulted in a decreased beam size that was dangerous to handle because of its increased intensity. Therefore, it was necessary to increase the beam diameter, and no proper beam expander was available at the UNAM facility. We decided to build our beam expander with a combination of a negative focus diverging lens and a converging lens with proper focuses, aiming to double the beam diameter to end up ~8mm. We deliberately used the diverging lens as the converging lens causes plasma formation in the air, causing a wasp-like sound and an emission of different λ.

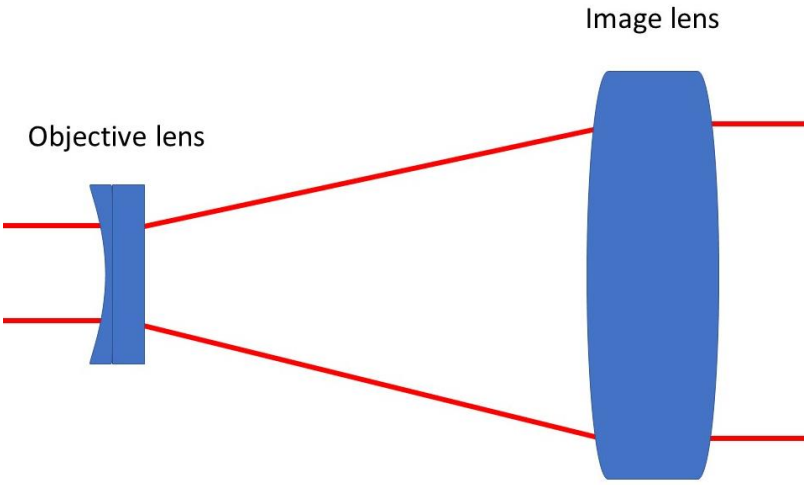

Figure 4.3. Beam expander for beam propagating from left to right

In Figure 4.3, the optics provide beam expansion from left to right, but the beam is reduced if the light propagates in the reverse direction. For this purpose, we tried a lens couple of f = -5 cm & f = 10 cm, increasing two times of the beam diameter.

While setting up the beam-expander system, we faced the following difficulties;

- Fitting into enough space was hard without changing the positions of some optics; thus, I changed some positions wherever possible but sometimes had difficulty fitting.
- The f = -5 cm lens had a burning in the midst of it since it is composed of two different lenses glued to each other, and that glue was burnt with the effect of the intense laser beam. After having a small black spot, it increased in time and made the spot bigger, as seen in Figure 4.4, and eventually, we had to change the lens.

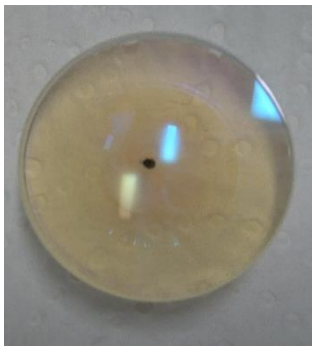

Figure 4.4. f = -5 cm lens with a small black burnt in the middle

After obtaining a proper lens, the modification of the system was successfully achieved by installing the beam expander, a couple of mirrors, and changing positions slightly, as shown in Figure 4.5. The changes included adding new mirrors for the guidance of the beam to form a common ground for our setup and other setups that also utilize the same beam. Also, we needed to incorporate two new mirrors to arrange the changed beam height after installing the TOPAS instrument. The larger dashed circle in the figure shows the locations of the added new mirrors beam expander. In comparison, the smaller circle shows the slightly changed location of the mirror that reflects the light required for photoexcitation in our system.

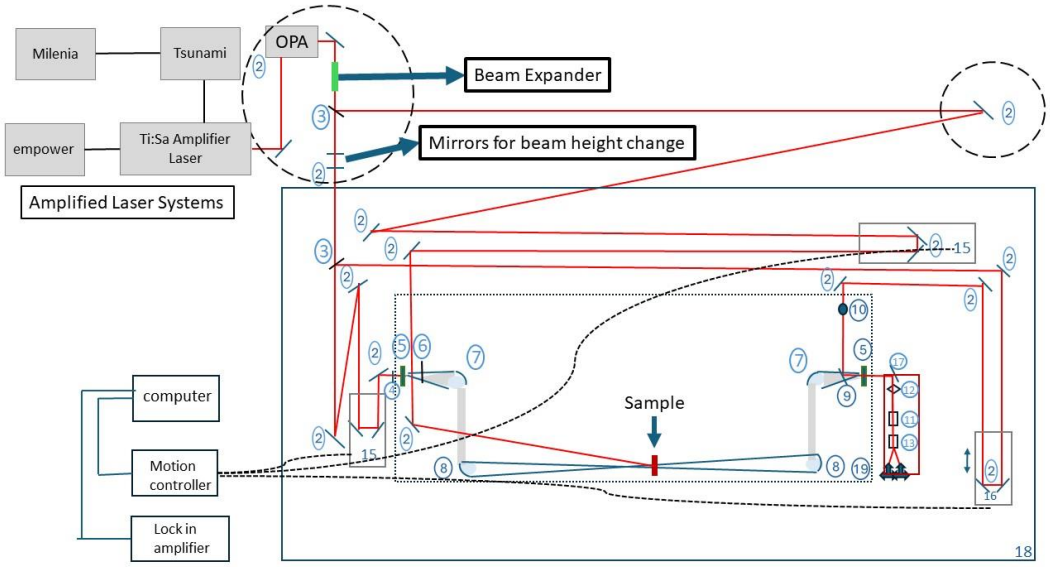

Figure 4.5. System modifications for beam expander in UNAM. The dashed circles show the adapted changes for installing the beam expander

4.8 Adaptation Of The TRTS Setup To The New Laser Configuration In TARLA

After the installation of the beam expander in the UNAM facility, the beam quality was worse before the activation of TOPAS, with less intensity in the middle part of the beam, which negatively influenced the attainable S/N for the TRTS system. Therefore, a need for moving the system to another laser lab emerged. It was possible to move our system to the TARLA facility.

Since the lab environment differed from UNAM, the TRTS system was required to be adapted to the new beam parameters. The 800 nm beam path was changed, whose difference can be seen in Figure 4.6.

After finishing up the required adjustment in configurational settings according to the new beam parameters and positional changes, the system was again optimized to attain the best S/N possible. The necessary optimizations resulted in a signal, as presented in Figure 4.7. The signal amplitude and achieved bandwidth increased as

compared to the UNAM signal. As Figure 4.7 presents, the current S/N at THz peak amplitude is ~10^5, and bandwidth could stretch up to 4.5 THz depending on the sample under examination.

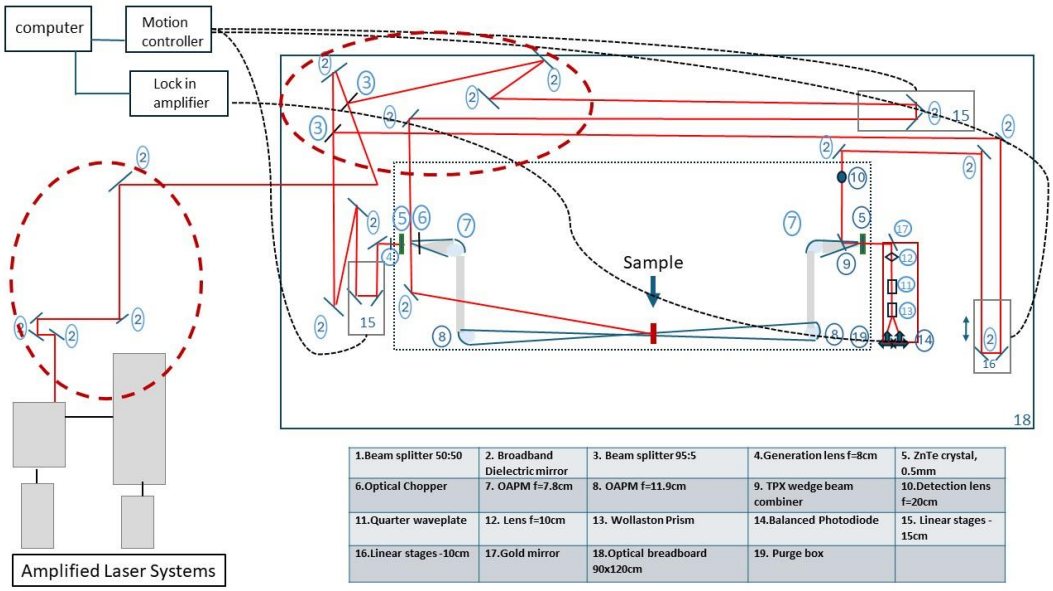

1.Beam splitter 50:50	2. Broadband Dielectric mirror	3. Beam splitter 95:5	4.Generation lens f=8cm	5. ZnTe crystal, 0.5mm
6.Optical Chopper	7. OAPM f=7.8cm	8. OAPM f=11.9cm	9. TPX wedge beam combiner	10.Detection lens f=20cm
11.Quarter waveplate	12. Lens f=10cm	13. Wollaston Prism	14.Balanced Photodiode	15. Linear stages - 15cm
16.Linear stages -10cm	17.Gold mirror	18.Optical breadboard 90x120cm	19. Purge box	

Figure 4.6. TRTS system with the adapted modifications to the laser lab in the TARLA facility

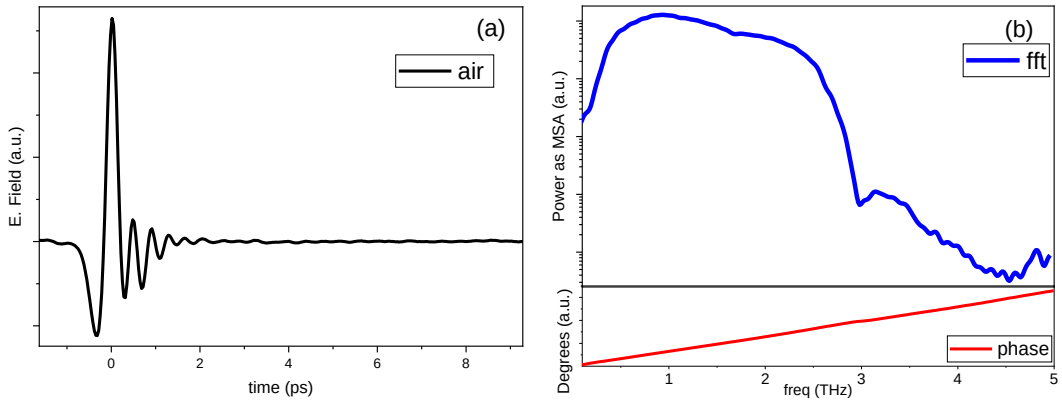

Figure 4.7. a) Time domain and b) frequency domain data together with extracted phase data of the optimized THz signal collected for air at the TARLA facility

4.9 Pump and Probe Beam Alignment in Time and Position

TRTS systems have a third arm time-delayed laser light used for photoexcitation of the analyzed sample, which differs from THz-TDS systems. In this case, the pump beam pulse and the THz probe pulses should coincide on the sample at the exact time to track the effect of photoexcitation by the THz light. So, having a working system, this matching of the optical and THz pulses in the time domain should be determined by a reference sample that gives a sharp response to photoexcitation. Here, the sample picked was Si/SiO_2, with a sharp THz peak response and long-living carriers whose lifetime exceeds the setup capabilities. The determined zero position could slightly shift depending on the thickness of the 2D material used and also the Natural Density (ND) filter to arrange the applied laser fluence.

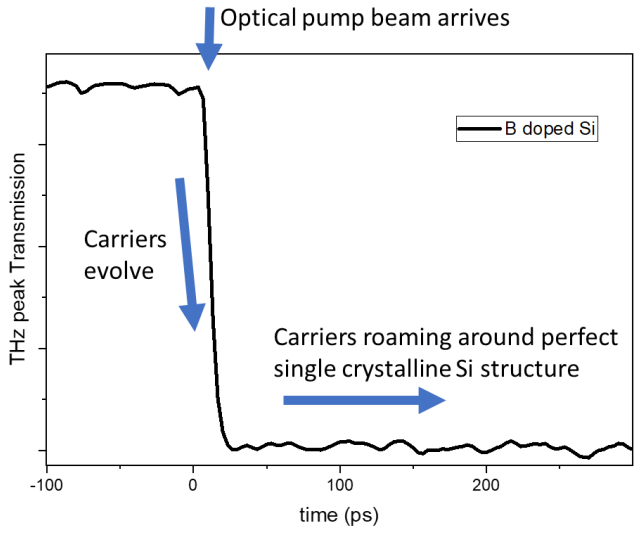

Figure 4.8. Zero-pump position of Si/SiO_2 sample

4.10 Fine Optimisation Steps

Before every measurement, parameters related to the system stability and low noise level should be checked to ascertain beam alignment for generation, detection, photoexcitation arm, THz generation angles, and detection crystals.

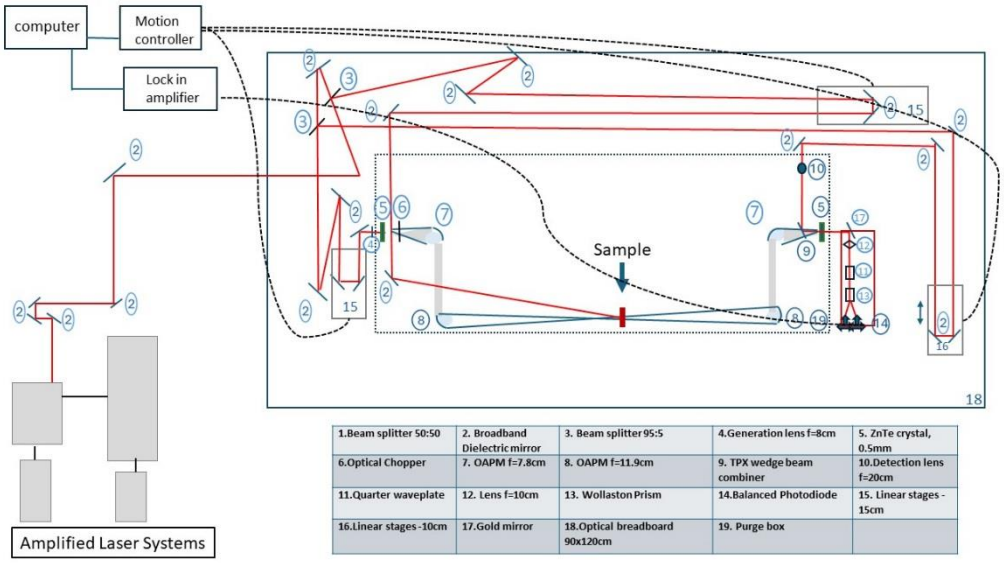

1.Beam splitter 50:50	2. Broadband Dielectric mirror	3. Beam splitter 95:5	4.Generation lens f=8cm	5. ZnTe crystal, 0.5mm
6.Optical Chopper	7. OAPM f=7.8cm	8. OAPM f=11.9cm	9. TPX wedge beam combiner	10.Detection lens f=20cm
11.Quarter waveplate	12. Lens f=10cm	13. Wollaston Prism	14.Balanced Photodiode	15. Linear stages - 15cm
16.Linear stages -10cm	17.Gold mirror	18.Optical breadboard 90x120cm	19. Purge box	

Figure 4.9. TRTS system with the adapted modifications to the laser lab in the TARLA facility

After assuring the laser stability, the following steps could be followed to maximize the signal:

- With the help of the irises beam alignment should be checked for generation and detection arm.
- The quarter waveplate angle could be rotated slightly (~couple of degrees for each direction) to have the optimum angle
- The generation and detection crystals (ZnTe) angles and beam positions for visible and THz beam overlap should be attested by an IR viewer.

- The beam position hitting the photodiode should also be checked by an IR viewer camera or IR card to ensure the beam hits the middle of the sensors.

4.11 Unidentified Noise Due To Environmental Changes

Advanced laser systems require environmental control with stable conditions in a particular laboratory. Thermal management, vibration control, and humidity are some of the crucial parameters that mainly affect the stability of a working laser system. Sometimes, meeting all requirements inside the lab may not be enough for optimum stability. In some cases, electrical noises through the neighboring labs or in some other parts of the building, construction vibrational or electronic noises around, unscheduled maintenance, or even a heavy vehicle like a train passing closely by the lab environment could be a source of high noise. Hence, if faced with a certain laser instability problem, one should first check the temperature and humidity values and then consider various possible sources inside and outside the lab.

Some of the sources for observed high noise throughout the study:

- The laser itself (primarily). Unfortunately, this problem has no proper solution because the noise usually comes from abrupt weather changes (temperature and/or humidity, for example). In such cases, the best practice is to wait until the situation is restored since such environmental changes last only a few days. However, seasonal changes are also the source of signal loss due to the drift in laser performance during the seasonal shifts. The laser cavity and seed beam alignment should be optimized in these cases. A professional should do this process.

- Misaligned beam hitting the photodetector. To solve this problem, we need an IR viewer camera since the light reaching the detector is weak and hence is not visible by bare eyes. The light should be aligned, so the beam should be in the middle of the sensors.

- Accidental misalignment may cause a shift in the laser beam position, which moves away from the middle of the detection crystal (ZnTe). This should be regularly checked. To do this, the last off-axis parabolic mirror should be handled carefully without touching the other mirrors in the system.
- The angle of the quarter waveplate should be checked to ensure that the split light reaching the detector has equal intensity.

CHAPTER 5

2D MATERIALS-PART Ⅰ

This chapter presents the time-domain and time-resolved Terahertz spectroscopy measurements and short discussions of highly anticipated 2D material, graphene. The details of the samples are given in the experimental section. The samples are composed of single-layer graphene (SLG) or multi-layer graphene (MLG) that are either grown/prepared with different methods or transferred to various substrates. THz-TDS profiles were collected for Air as a system check, the substrate as a reference, and the samples. TRTS measurements, on the other hand, exclude polymer substrates and Quartz due to their irresponsive behavior to optical excitation. When semiconductor substrates such as Si wafers and SiC are excited, they tend to respond strongly. This poses a challenge when studying single-layer graphene (SLG) carrier behavior since the sample response also contains the substrate response. To isolate the carrier behavior of SLG alone, it is necessary to subtract the substrate response from the sample response. Such studies were discussed in Chapter 7, where optical pump THz probe behaviors were analyzed and compared.

5.1 Single-layer graphene on polyethylene terephthalate

The SLG was produced using the Chemical Vapour Deposition (CVD) technique and then transferred to a polyethylene terephthalate (PET) substrate at Eskisehir Technical University. The time domain profiles of the air, substrate, and SLG on PET are presented in Figure 5.1. As expected, the PET substrate causes a shift in time due to the delay of the pulses with its higher refractive index relative to the air and its thickness. The delay is directly proportional to the measured samples' indices

and thicknesses. If the PET thicknesses of the reference and the sample substrate were the same, the shift amount should have been the same or slightly delayed more due to the extra SLG on PET. However, the early appearance of the sample profile relative to the reference substrate suggests that the substrate thicknesses were different. Another observation is the decrease in the amplitude of the profiles. The change observed for the PET relative to the air shows the loss in transmitted THz frequencies due to absorption, reflection, or scattering. Similarly, there is an intensity decrease for the sample signal, indicating a certain THz beam loss owing to absorption and reflection. The comparison relative to air shows the cumulative effect of substrate and the SLG. However, comparing the sample response to the substrate response isolates the SLG behavior. In general, about 4 % loss is expected[98], and a similar response was observed here.

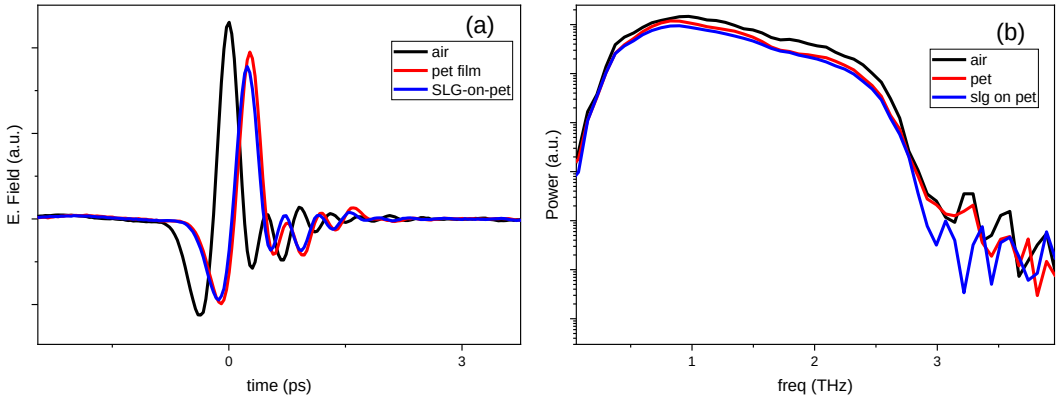

Figure 5.1. a) Time-domain b) Frequency-domain profile of free space (air), substrate PET, and SLG on PET.

Figure 5.2 presents the 800nm pump THz probe, the time-resolved measurement of the SLG on the PET sample collected by the TRTS instrument, described in the

experimental part. A positive change in the transmission was observed during the measurements, meaning the THz transmission increased with the 800nm pumping, and over time, it recovered to the original transmission level. As discussed, this behavior corresponds to a negative photoconductivity behavior in the theoretical part. This is expected for SLG due to its high carrier density. A detailed explanation of the dynamics will be provided in the upcoming chapter. However, the sample responds quickly and sharply, showing a short-living decay profile for the generated carriers due to scattering mainly among themselves.

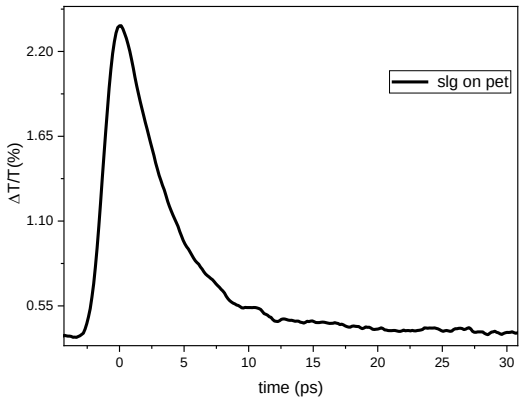

Figure 5.2. Differential THz transmission, $\Delta T/T_0$, of SLG on PET as a function of pump–probe delay recorded at a fluence of 300 $\mu J/cm^2$.

5.2 Single-layer graphene on Polydimethylsiloxane

The SLG sample was also produced via the CVD technique and then transferred onto a polydimethylsiloxane (PDMS) substrate at Eskisehir Technical University. The time domain response profiles of the air, substrate PDMS, and SLG on PDMS are shown in Figure 5.3. Similarly, due to the higher index of PDMS and its thickness, the PDMS substrate causes a delay in the THz pulses, and a shift in time was observed. If the PDMS thickness of the reference substrate and the sample were the same, the shift amount observed in the sample measurement should have been very

close and may have been slightly delayed due to the extra layer. Unfortunately, less shift was observed for the substrate+SLG. This suggests that the substrate thicknesses differed for the reference and the sample. On the other hand, there is an intensity decrease for both the reference and the sample signal, as expected, due to transmission losses. This indicates a specific THz beam loss due to the absorption, scattering, and reflection of the signal compared to the air. However, the decrease is less for the SLG sample signal. Usually, with the addition of SLG on the substrate, there should have been more losses, as observed in the previous case. This difference may come from the significant thickness differences between the sample and reference substrates.

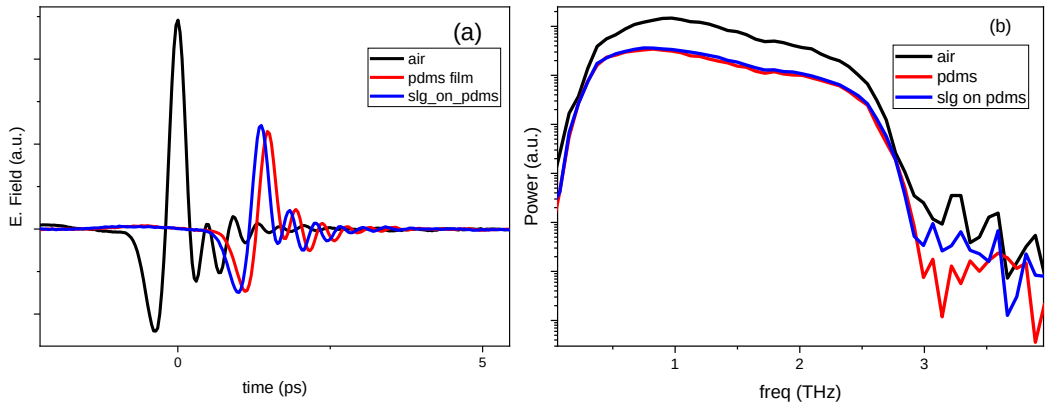

Figure 5.3. a) Time-domain b) Frequency-domain profile of free space (air), substrate PDMS, and SLG on PDMS.

The graph in Figure 5.4 shows the dynamic change in THz transmission with 800nm excitation. The data was collected with the TRTS instrument. When exposed to an 800nm beam, it displays negative THz photoconductivity similar to the previous sample, which is expected from SLG because of its high carrier density. The observed fast dynamics of carrier generation and evolution are typical of graphene.[99] A detailed explanation of the response will follow in the upcoming chapter.

However, we can tell that the sample responds quickly and sharply, and the generated carriers are short-lived according to the decay profile, mainly due to scattering among themselves.

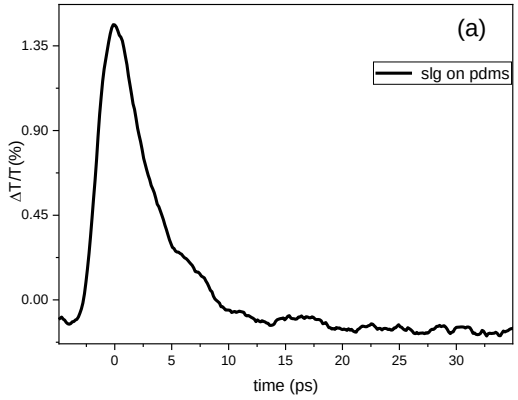

Figure 5.4. Differential THz transmission, $\Delta T/T_0$, of SLG on PDMS as a function of pump–probe delay recorded at a fluence of 300 $\mu J/cm^2$.

5.3 Single-layer graphene on a blend of polymethyl methacrylate and polydimethylsiloxane

The SLG was again produced via CVD technique and then transferred to a blend of polymethyl methacrylate (PMMA) and polydimethylsiloxane (PDMS) substrates of two different thicknesses. The time domain profile of the air, PDMS substrate as a reference, and the first sample are shown in Figure 5.5. The transmission of PDMS substrate has been discussed before. There is a significant shift and decrease in the THz amplitude as the light passes through the sample. The observed shift is directly proportional to the average index of the sample and its thickness. There is also significant amplitude loss, possibly due to strong absorption of PMMA. This is first confirmed by the profile change of the THz pulses and by the frequency domain amplitude data.

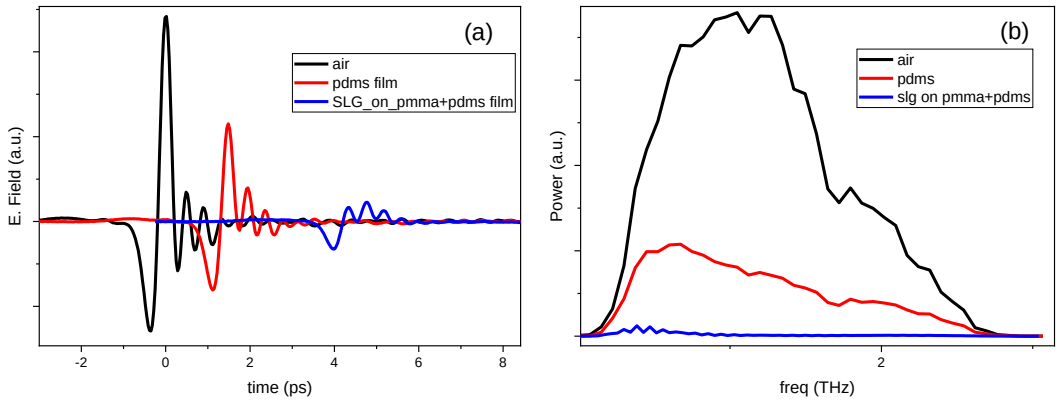

Figure 5.5. a) Time-domain b) Frequency-domain profile of free space (air), substrate PDMS, and SLG on a blend of PDMS and PMMA.

The time-resolved carrier dynamics of graphene on the blend substrate were also measured with the TRTS instrument. The two samples' carrier generation and decay dynamics response are shown in Figure 5.6 (a) and (b). Each graph depicts an increase in THz transmittance when they were optically excited by 800nm laser light. This confirms the presence of SLG in both samples, which will be discussed in detail in the upcoming chapter. It's worth noting that both samples similarly responded quickly and sharply, leading to a short-lived decay profile for the generated carriers due to carrier-carrier scattering; however, after the initial faster decay of the smaller sample, around 322ps seems to decay slower than the bigger sample. On the other hand, the bigger sample appears to have more intense THz conductivity than the smaller one, indicating that even though their substrates and production processes are the same, each sample is not identical.

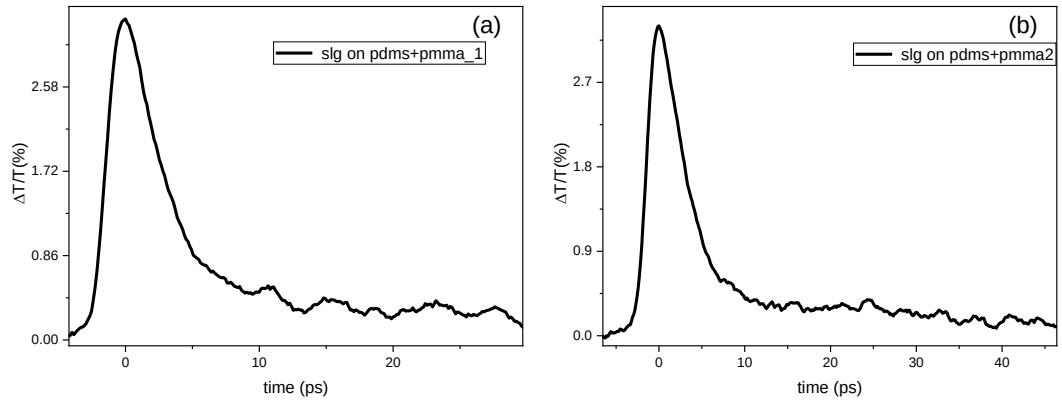

Figure 5.6. Differential THz transmission, $\Delta T/T_0$, of a) smaller sample of and b) larger sample of SLG on blend PDMS/PMMA as a function of pump–probe delay recorded at a fluence of 300 $\mu J/cm^2$.

5.4 Epitaxial single-layer graphene on silicon carbide

Two epitaxially grown SLG samples on SiC substrate were also analyzed using THz-TDS. The samples were expected to have an interface layer consisting of Si and C atoms; an SLG layer exists upon this. The samples are expected to have n-doping as opposed to CVD-grown graphene, which has p-type doping.[100,101] For analysis of the samples, the THz-TDS was utilized first, resulting in the responses presented in Figure 5.7. As the figure shows, sample-1 and sample-2 respond similarly to their reference, bare SiC. As expected, their thicknesses were the same as they seemed to shift almost equally in the time domain. On the other hand, their interaction with the THz pulse makes a noticeable difference, namely that sample-2 causes absorption of the THz signal three times more than that of sample-1, clearly indicating that the same batch samples grown on the same sort of substrate are not identical.

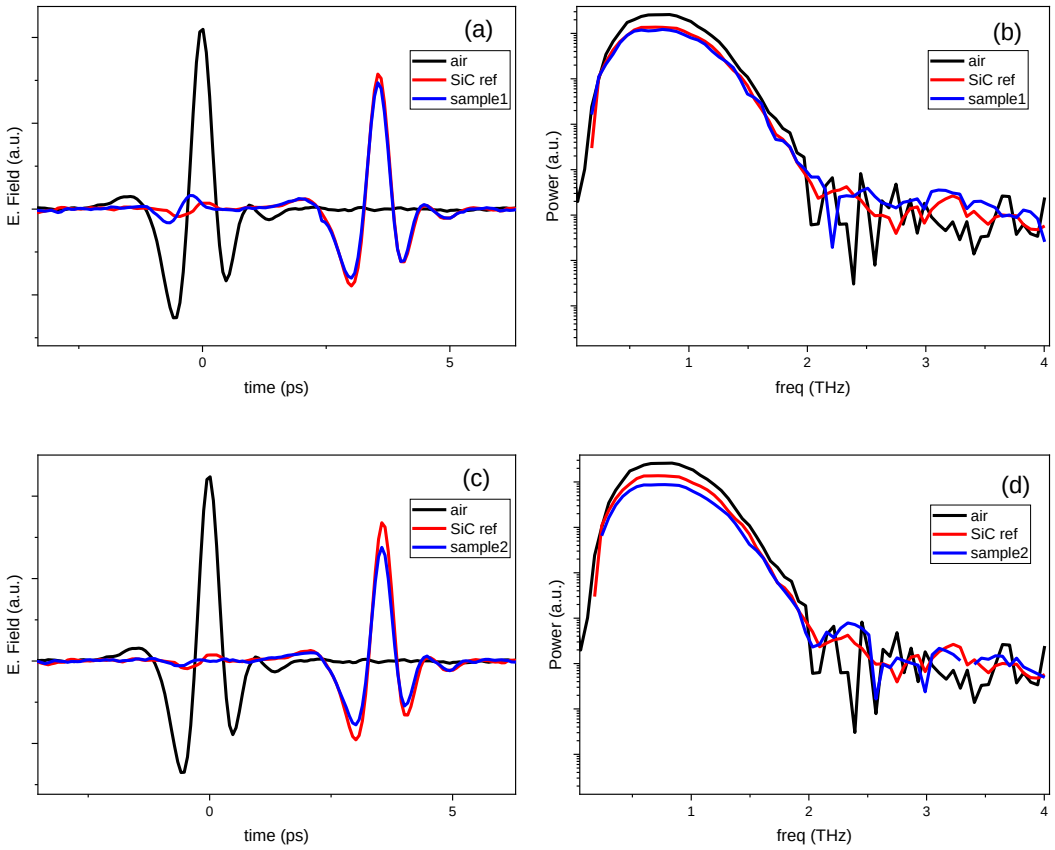

Figure 5.7. a) Time-domain b) Frequency-domain profile of free space (air), substrate SiC and sample1 of SLG on SiC. c) Time-domain d) Frequency-domain profile of free space (air), substrate SiC, and sample2 of SLG on SiC

TRTS studies showed their dynamic responses, presented in Figure 5.8. Since SiC is a semiconductor, the reference's differential change in the THz pulse peak was also observed (black line) when optically excited by 800nm light, whose details will be discussed in Chp 7. The negative nature of the signal corresponds to a decrease in THz transmission and shows the increase in carrier density with the photoexcitation. Though this response was expected, the strong response of the SiC substrate makes it quite hard to differentiate the sole SLG response. Similar but stronger responses

were observed with the SLG layers on the SiC on the two samples. The responses were all dominated by the SiC response. The observed increase may be attributed to the response of the SLG. However, the SLG responses are expected to be intense but quite sharp and short-lived, followed by the SLG samples on the polymer substrates. Thus, here, the responses are convoluted responses of both the SiC and the SLG. The stronger responses of the semiconductor SiC substrate of the SLG samples might be due to the doping of the substrate either during the growth process or by the electron transfers from the graphene when photoexcited. Therefore, the sample response is subtracted from the reference signal to obtain the SLG dynamics, as presented in Figure 5.8 (b). As can be seen from the figure, both samples ended up with a different response from each other as they gave in their THz-TDS signal. Unlike the SLG on polymer samples, the photoexcitation of SLG decreases the THz transmission; thus, its behavior is more like multilayer graphene samples.[102] In addition, sample 2 had a stronger THz absorption in the time domain and showed a weaker THz photoconductivity response, which could be mainly due to having more than one layer.

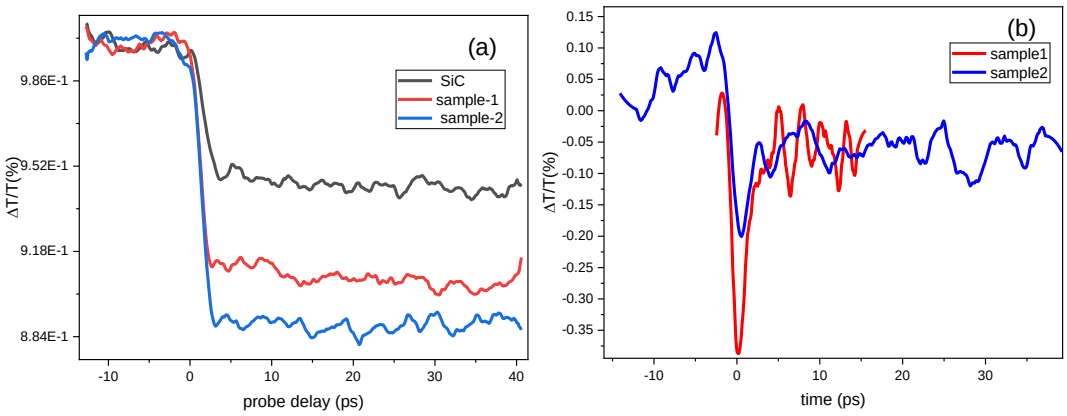

Figure 5.8. a) Differential THz transmission, $\Delta T/T_0$, of two samples of SLG on SiC as a function of pump–probe delay recorded at a fluence of XYZ μJ/cm^2. b) Derived response of the SLG layer relative to the SiC.

5.5 Commercial single-layer graphene on Si wafer

The sample is a commercial SLG produced by CVD and transferred onto a Si wafer substrate. Thus, the structure is Si/SiO_2/graphene/photoresist, as stated in the experimental part. Here, Si is a semiconducting layer, and the dielectric SiO_2 layer naturally forms on the Si wafer and is about a few nanometers thick. The photoresist is covered on graphene to protect the graphene from external exposure and reduce charging and contamination.

The differential THz peak pulse of optically excited reference and sample for three different pump fluences of 84 μj/cm^2, 280 μj/cm^2, and 650 μj/cm^2 are collected over time and presented in Figure 5.9. The details regarding carrier decay dynamics and its modelling will be discussed in Chapter 7. Like the Si carbide, the semiconductor substrate dominated the responses. As the pump fluence increased, the difference between the sample and the pristine Si wafer decreased. At a pump fluence of 84 μj/cm^2, the sample response appears to be approximately 7% stronger than the Si reference. This difference, however, reduces to about 1% with an increase in fluence to 280 μj/cm^2 and eventually becomes roughly the same when the sample was photoexcited with a fluence of 650 μj/cm2.

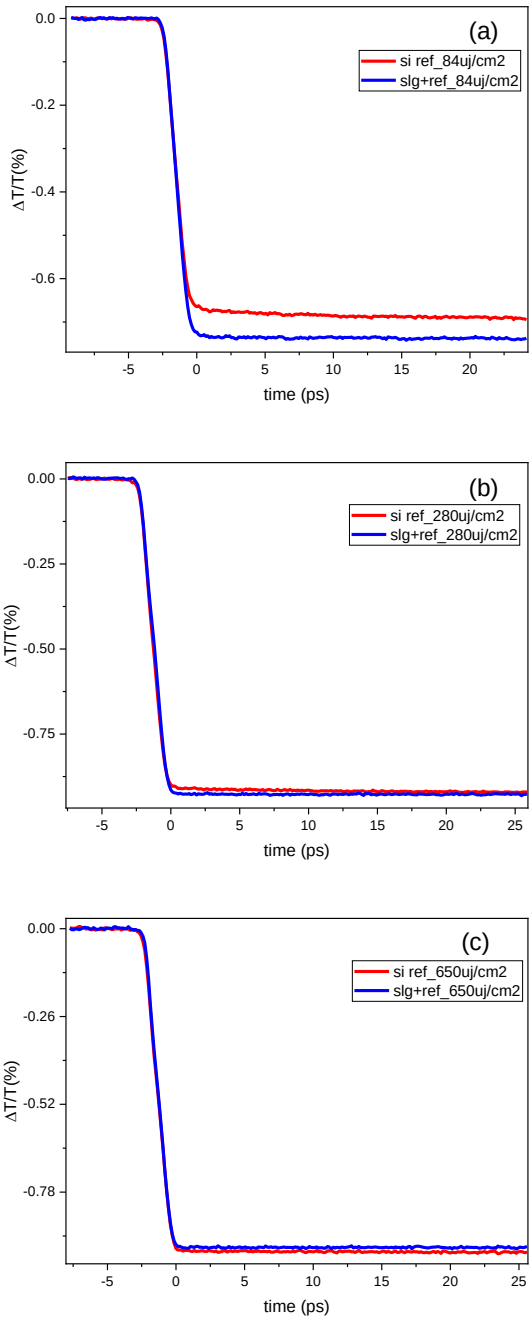

Figure 5.9. Differential THz peak transmission response, $\Delta T/T_0$, of Si/SiO_2 as reference and SLG on Si/SiO_2 as a function of pump–probe delay recorded at pump fluences of a) 84 μj/cm^2, b)280 μj/cm^2, and c) 650 μj/cm^2.

In order to extract the SLG dynamics, subtracting the sample response, which includes the Si response, from the reference signal is necessary. The resultant output provides the evolution of SLG and SLG effect on Si, as illustrated in Figure 5.10. The figure suggests that the subtracted signals with respect to different fluences still contain traces from strong Si carrier response, meaning that the subtraction process was not enough to isolate the SLG response. Also, the fluence effect on the obtained individual graphs showed that as the fluence increases, the SLG response dominates over the Si response. In the meantime, the Si response was saturated, and the SLG response, as observed on the polymer substrates, was extracted. Even though the relative SLG response was higher at lower pump fluences, the response could not be isolated. Further investigation will be carried out in Chapter 7, where the rise and decay dynamics were compared.

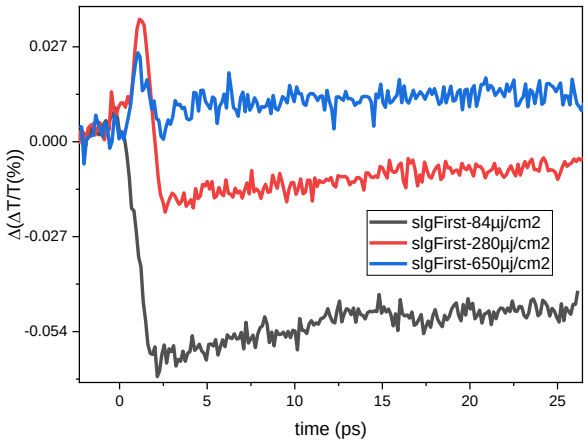

Figure 5.10. The difference in differential THz peak transmission response of the data is given in Figure 5.9.Si/SiO_2 substrate response was considered as a reference.

5.6 Multi-layer graphene, MLG850, on quartz

The present study investigates the THz dynamics of a multi-layer graphene (MLG) sample comprising approximately 30 layers. The sample was obtained using the chemical vapor deposition (CVD) technique and transferred to a Quartz substrate.

The THz dynamics were studied by exciting the sample using a near-infrared (NIR) pulse of 800 nm and probing it with THz light. The study results are presented in Figure 5.11, and details are discussed in Chapter 7. The inset shows a long scan of the samples over 450 ps. The figure indicates that the initial response of the sample upon optical excitation showed a rise time of 2.54ps, which is much more than the instrument limit of 0.5 ps. These samples are over eight years old, and the rise time increases over the years from 1.78ps.[94] Over the period, the rise time increased, which could be attributed to the oxidation of the sample. The decay dynamics and carrier evolution changes over the period will be discussed in Chapter 7. The study provides valuable insights into the THz dynamics of graphene and highlights the importance of examining samples for extended periods to gain a comprehensive understanding of their behavior.

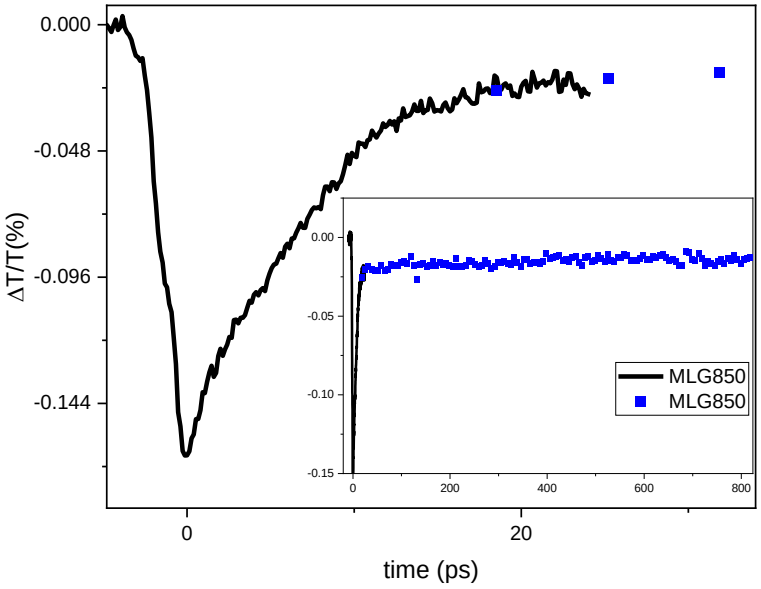

Figure 5.11. Differential THz transmission, $\Delta T/T_0$, of MLG850 as a function of pump–probe delay recorded at a fluence of 700 μJ/cm^2.

5.7 Multi-layer graphene, MLG900, on quartz

The first sample, MLG900, consists of around 60 layers, while the second sample, MLG1000, has 100 layers. Both samples were obtained using the chemical vapor deposition (CVD) technique and then transferred onto a Quartz substrate. The details are given in the experimental part. The samples were excited by a near-infrared (IR) pulse to study the THz dynamics and then probed using THz light.

As the layer thickness increases, the THz transmission loss increases since every layer accounts for a loss of approximately 4%. Thus, compared to MLG850, the transmission loss is almost twice through the sample MLG900. The lower signal amplitude and further delay in time relative to the air are caused by this higher layer number.

Figure 5.12 presents differential THz probe transmission of MLG 900 samples excited by 800 nm. Details regarding the dynamics of the carriers will be discussed in Chapter 7. Due to the higher loss amount with the doubled layer numbers, the THz peak amplitude is as stated. Thus, the signal-to-noise (S/N) level is considerably lower in differential THz transmission data. However, it is still high enough for the nonlinear analysis. The sample's initial response upon optical excitation had a rise time of roughly 5 ps. However, the rise time appeared to increase over eight years, which was around 3 ps[94], possibly due to the sample's oxidation. The research provides valuable insights into Graphene's THz dynamics and emphasizes the significance of examining samples for extended periods to understand their behavior comprehensively.

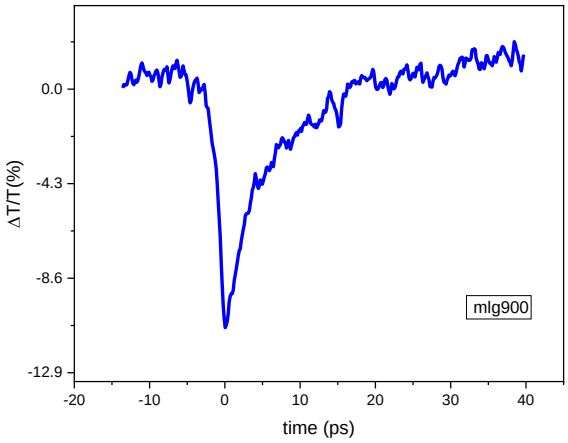

Figure 5.12. Differential THz transmission, $\Delta T/T_0$, of MLG900 as a function of pump–probe delay recorded at a fluence of 250 $\mu J/cm^2$.

The sample, MLG900, consisting of around 60 layers, was also analyzed once the system was transferred to TARLA in the new set-up. The time domain profile of the sample was collected with THz-TDS set-up and presented in Figure 5.13. The sample causes a further decrease in THz signal amplitude compared to the quartz itself due

to absorption/reflection losses mainly caused by graphene layers. The earlier arrival of THz pulse through the sample suggests that the MLG graphene has a negative refractive index. However, this is not possible because graphene has a positive refractive index; therefore, the difference should stem from the thickness difference between the reference quartz substrate and quartz substrate under the MLG layer.

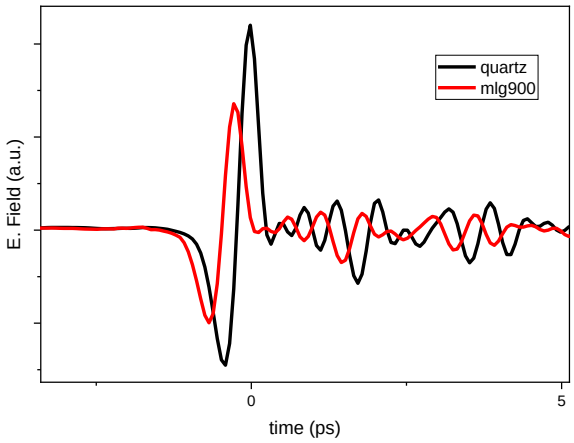

Figure 5.13. Time-domain profile of MLG900 sample on Quartz.

The samples were excited by 400nm and 800nm laser pulses to study the THz dynamics and then probed using THz light. The resultant transient data is presented in Figure 5.14. A detailed discussion of the dynamics will be given in Chapter 7. Firstly, the S/N level of the current TRTS instrument is one-fold higher than the data collected by set-up at UNAM (Figure 5.12). The sample's initial response to 400 nm had a rise time of around 2 ps; on the other hand, 800nm excitation resulted in a rise time of 4ps, both well above the instrument limit of 0.5ps. Upon both 400nm and 800nm excitations, the long recovery time (tail of the data) shows that the sample has a longer carrier lifetime than our experimental scan limit of ca 500 ps. The rise and multi-exponential decay dynamics upon 400nm and 800nm excitations will be discussed in Chapter 7.

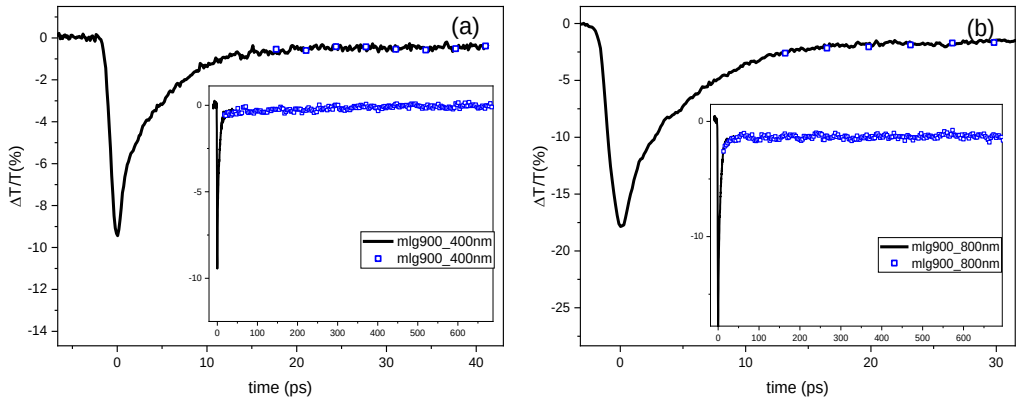

Figure 5.14. Differential THz transmission, $\Delta T/T_0$, of MLG900 as a function of pump–probe delay recorded at a fluence of 230μJ/cm^2 for 400nm excitation and b) a fluence of 700μJ/cm^2 for 800nm excitation. Insets show the long scans covering a 450 ps time scale, enabling the observed long-lived carrier dynamics.

5.8 Multi-layer graphene, MLG950, on quartz

The sample MLG950, consisting of around ca. 70 layers, was analyzed using the new system available in TARLA. The sample was obtained using the chemical vapor deposition (CVD) technique and then transferred onto a quartz substrate. Firstly, the THz-TDS was utilized, resulting in the responses in Figure 5.15. The figure presented depicts the decrease in THz signal amplitude caused by the sample compared to quartz alone, primarily due to the absorption/reflection by graphene layers. Additionally, the graph indicates that the sample causes less shift in the time domain than pristine quartz, possibly indicating the negative refractive index of graphene. However, it is crucial to note that graphene has a positive refractive index, and the difference between the two most probably arises from the variation in thicknesses between reference quartz and graphene-coated quartz. Figure 5.15(b) presents the nonuniform thickness of the samples. Although the samples were prepared using the same procedure, the two samples prepared under the same

conditions have slight differences. Sample 2 (slightly bigger in size) caused more loss of THz signal and resulted in a more remarkable shift in the time domain. These results show the strength of the THz-TDS technique in the determination of index, thickness, etc., in other words, the static properties of the materials, especially relative changes.

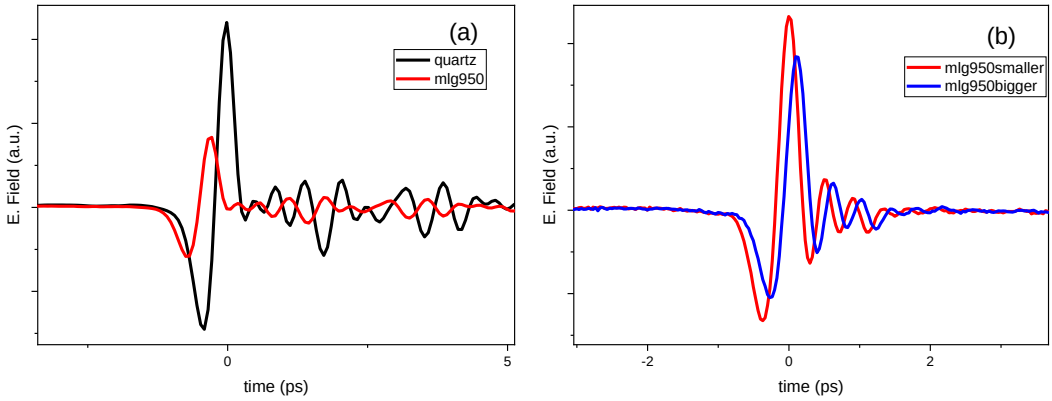

Figure 5.15. Time-domain profiles of (a) Quartz substrate and MLG950 sample on Quartz and (b) two different MLG950 samples compared

The samples were excited by 400nm and 800nm laser pulses to study the THz dynamics and then probed using THz light. Figure 5.16 presents the transient data for the Sample 1 (smaller piece). Once again, the signal and the noise levels were significantly improved compared to the system at UNAM. Hence, we have an outstanding S/N level for this study to extract the dynamics associated with carrier generation and recombination, which will be presented in Chapter 7. When subjected to 400 nm excitation with a fluence of 230μj/cm^2, the sample exhibited an initial response with a rise time of approximately 2 ps, followed by fast recombination and long-lived free carriers. Conversely, 800 nm excitation with a fluence of 700 μj/cm^2

resulted in a rise time of around 4 ps, followed by rapid recombination and long-lived free carriers. In both cases, the sample responded with a free carrier lifetime that exceeded our experimental limit of approximately 0.5 ns.

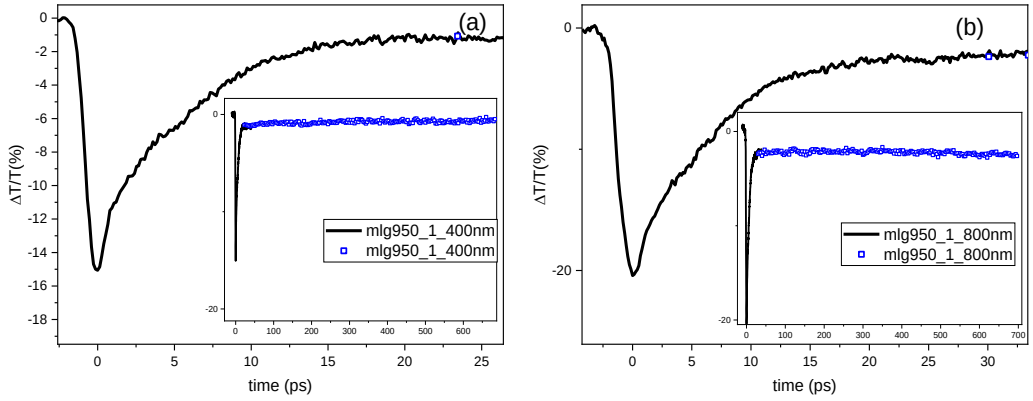

Figure 5.16. Differential THz transmission, $\Delta T/T_0$, of MLG950 Sample 1 as a function of pump–probe delay recorded at (a) a fluence of 230 μJ/cm^2 for 400nm excitation and b) a fluence of 700 μJ/cm^2 for 800nm excitation. Insets show the long scans covering up to 450 ps time scale and enable the observation of long-lived carrier dynamics.

Figure 5.17 illustrates the transient response of the MLG950 Sample 2 upon 400nm and 800nm excitation with the fluences of 230μJ/cm^2 and 700μJ/cm^2, respectively. Once again, the noise level was outstanding and enabled investigation of the carrier dynamics, which will be given in Chapter 7. When Sample 2 was subjected to 400 nm excitation, the sample exhibited an initial response with a rise time of approximately 2 ps, similar to Sample 1. Unlike Sample 1, the 800 nm excitation resulted in a faster rise time of around 2 ps. Even though the samples were supposed to be the same, both the THz-TDS and TRTS data suggest significant differences in

the sample's static and dynamic properties. In both cases, the sample showed a free carrier lifetime higher than our experimental limit of 0.5 ns.

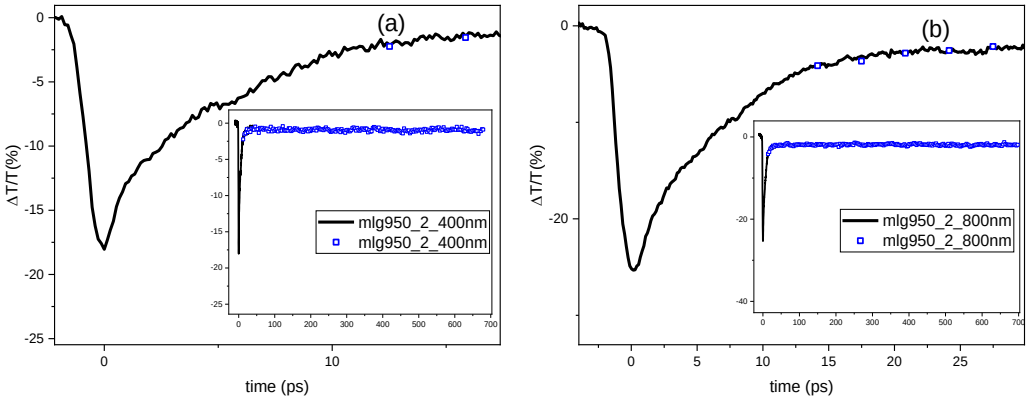

Figure 5.17. Differential THz transmission, $\Delta T/T_0$, of MLG950 Sample 2 as a function of pump–probe delay recorded at a fluence of 230 μJ/cm^2 for 400nm excitation and b) a fluence of 700 μJ/cm^2 for 800nm excitation. Insets show the long scans covering up to 450 ps time scale and enable the observation of long-lived carrier dynamics.

5.9 Multi-layer graphene MLG1000, on quartz

Figure 5.18, on the other hand, presents differential THz probe transmission of MLG1000 sample excited by 800 nm. The corresponding rise and decay dynamics will be discussed in Chapter 7. Further increase of the layer numbers to 100 in this sample relative to ca.30 of MLG850 resulted in a significant loss in THz transmission through the sample. Thus, the peak THz amplitude S/N level is relatively low. Therefore, the noise level seems comparable to the response level, making it harder to evaluate the sample response, which is also relatively weak. Averaging the data helps further to increase the S/N level. The sample's initial response upon optical excitation had a rise time of around 6-7 ps. However, the rise time increased over eight years, which was ca 4.5 ps[94], possibly due to the sample's oxidation. The study

provides valuable insights into the THz dynamics of graphene and emphasizes the significance of examining samples for extended periods to gain a comprehensive understanding of their behavior.

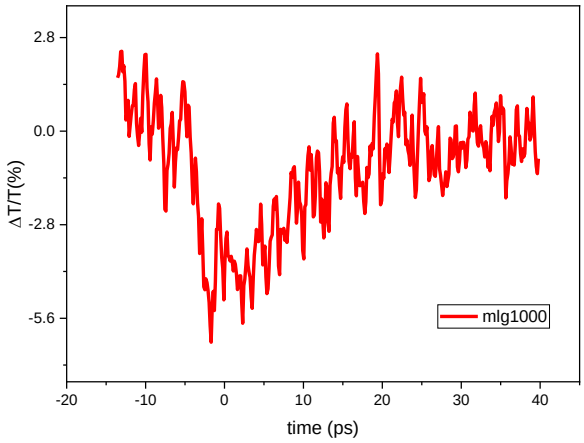

Figure 5.18 Differential THz transmission, $\Delta T/T_0$, of MLG1000 as a function of pump–probe delay recorded at a fluence of 450 $\mu J/cm^2$.

The same sample, MLG1000, was also analyzed using the newly set up system in TARLA. Firstly, the THz-TDS instrument was utilized to measure the time-resolved THz beam transmission through the sample, as presented in Figure 5.19. As mentioned above, the transmitted THz signal amplitude decreased significantly due to the high number of graphene layers (about 100). This affects both the time domain and time-resolved studies since the Terahertz amplitudes passing through the sample are low, resulting in low S/N levels. The data also shows that the sample causes less shift in the time domain than pristine quartz. Typically, such a behavior would indicate a negative refractive index of Graphene. However, Graphene has a positive refractive index, and the difference between the two mainly arises from the variation in thickness between reference quartz and Graphene-coated quartz. Figure 5.19(b) presents the time-domain profiles of two different MLG1000 samples. Similar to the

MLG950 samples, the samples exhibit slight differences despite their similar preparation. The larger sample demonstrates a more pronounced absorption of the THz signal and a more significant shift in the time domain, which can be readily detected via the THz-TDS technique. This shows that the layer number is slightly more than that of Sample 1.

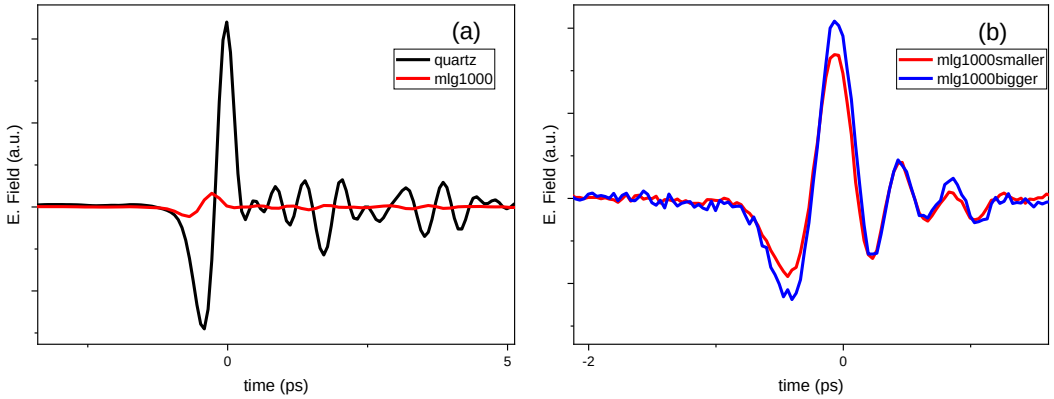

Figure 5.19. (a) Time-domain profiles of Quartz substrate and MLG1000 sample on Quartz and (b) two different MLG1000 samples compared

5.10 Comparison of all MLG on quartz samples

Figure 5.20 presents the THz-time domain profiles of all the MLG samples on quartz for comparison. As expected, the THz transmission decreases with the layer number. Due to the differences in the quartz substrate of the samples, it is challenging to compare the average change in time concerning the layer number. However, the results clearly show that the two samples of MLG950 are somewhat different from each other.

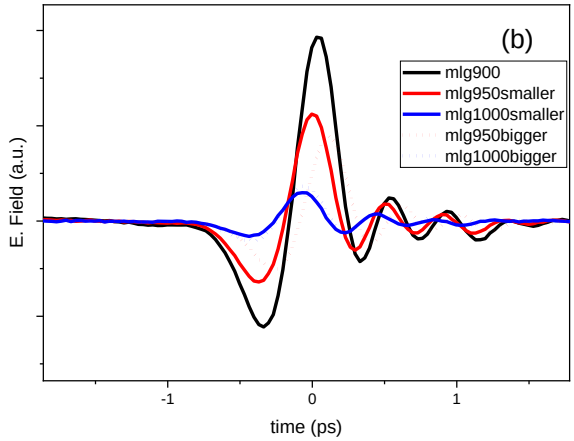

Figure 5.20. Time-domain profiles of MLG900, two MLG950, and two MLG1000 samples on quartz.

The samples were excited by 400 & 800 nm laser pulses for their THz conductivity behavior and then probed using THz light, as presented in Figure 5.21, for smaller pieces. In Chapter 6, you will find a detailed discussion of the matter. According to the figure provided, the response seems stronger for the 800nm pump. When subjected to 400 nm excitation, the sample exhibited an initial response with a rise time of approximately 3 ps. Conversely, 800 nm excitation also resulted in a rise time of around 3 ps. In both cases, the sample responded with a carrier lifetime that exceeded our experimental limit of approximately 0.5 ns. 800nm excitation. This results in better THz conductivity, leading to longer initial and overall decay.

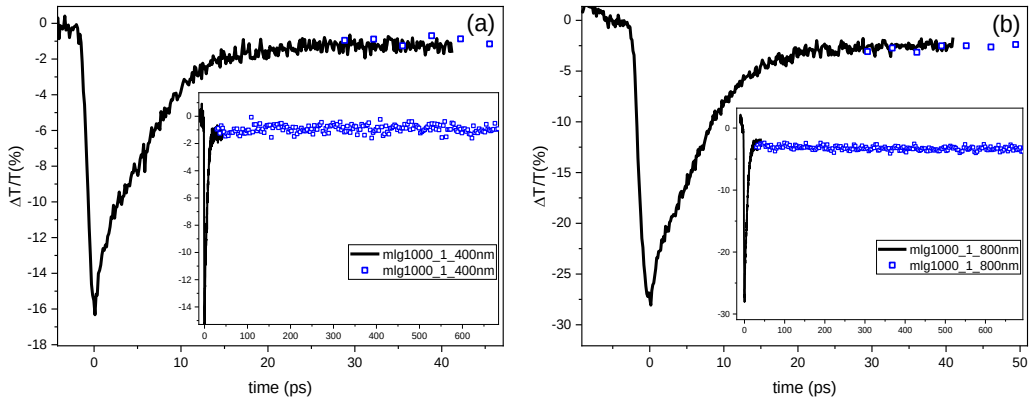

Figure 5.21. Differential THz transmission, $\Delta T/T_0$, of MLG1000 Sample 1 as a function of pump–probe delay recorded at (a) a fluence of 230 μJ/cm^2 for 400nm excitation and b) a fluence of 700 μJ/cm^2 for 800nm excitation. Insets show the long scans covering up to 450 ps time scale and enable the observation of long-lived carrier dynamics.

The second sample was also excited by 400 & 800 nm laser pulse and then probed using THz light, as presented in Figure 5.21 for its THz conductivity. In Chapter 7, you will find a detailed discussion of the matter. Based on the given figure, the response appears stronger for the 800nm pump. When the sample was exposed to 400 nm excitation, it showed an initial response with a rise time of approximately 3 ps. Similarly, 800 nm excitation also resulted in a rise time of around 4 ps. In both cases, the sample exhibited a carrier lifetime beyond our experimental limit of approximately 0.5 ns. 800nm excitation results in better THz conductivity, which leads to longer initial and overall decay.

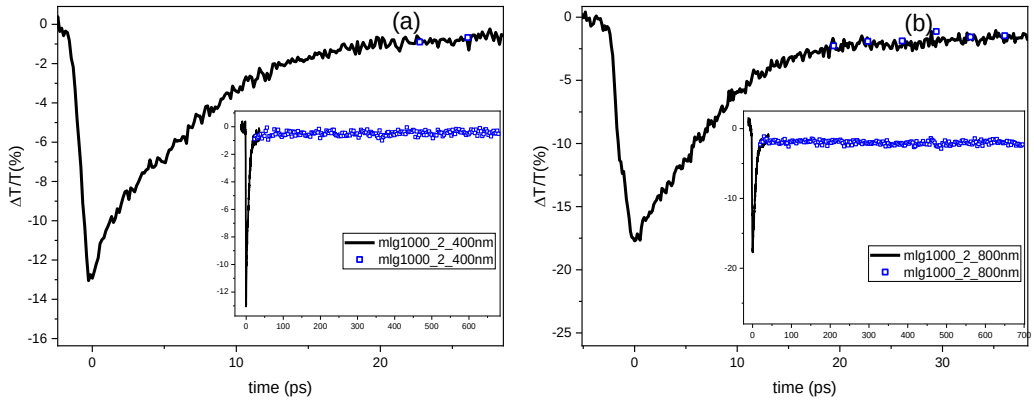

Figure 5.22. Differential THz transmission, $\Delta T/T_0$, of MLG1000 Sample 2 as a function of pump–probe delay recorded at (a) a fluence of 230 μJ/cm^2 for 400nm excitation and b) a fluence of 700 μJ/cm^2 for 800nm excitation. Insets show the long scans covering up to 450 ps time scale and enable the observation of long-lived carrier dynamics.

5.11 Multi-layer graphene on polyvinyl chloride

The sample was obtained using the chemical vapor deposition (CVD) technique and then transferred onto a polyvinyl chloride (PVC) substrate. The details are given in the experimental part. The sample consisted of approximately 30 layers and was analyzed by TARLA's newly set spectrometer system.

The sample was excited by an 800nm laser pulse with a fluence of 700 700 μJ/cm^2 for THz conductivity behavior and then probed using THz light. The resultant transient data is presented in Figure 5.23. After the 800 nm excitation, the carrier generation resulted in a rise time of around ca. 3 ps, similar to the MLG850. That is followed by a sharp decay due to the cooling and recombination of the carriers. Finally, a significant quantity had lived as a free carrier. Interaction of the free carriers with the significant mean free path was observed as the long-living tail in

the transient response. The sample response for its carrier lifetime exceeds our experimental limit of approximately 0.5 ns.

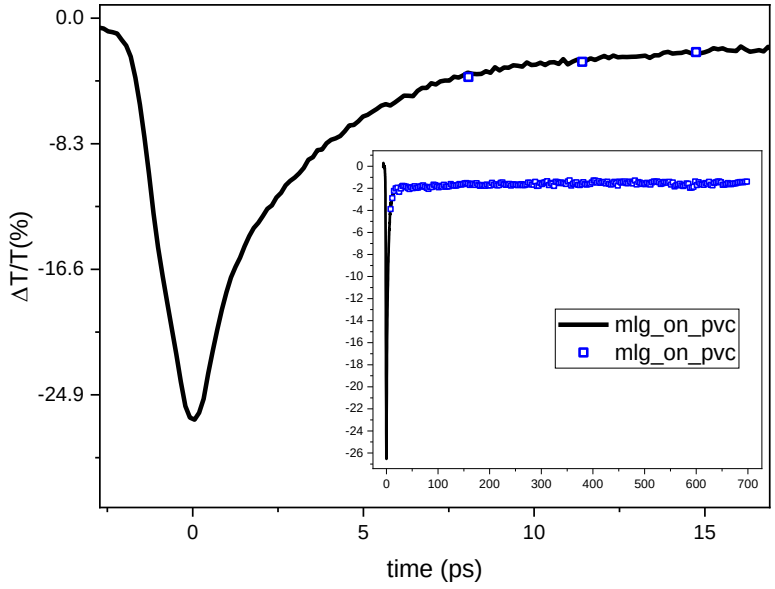

Figure 5.23. Differential THz transmission, $\Delta T/T_0$, of MLG on PVC as a function of pump–probe delay recorded at a fluence of 700 μJ/cm^2 for 800nm excitation. Inset shows the long scans covering up to 450 ps time scale and enables the observation of long-lived carrier dynamics.

5.12 Multi-layer graphene on polyethylene

The sample was obtained using the chemical vapor deposition (CVD) technique and then transferred onto a polyethylene (PE) substrate. The sample consisted of approximately 32 layers and was analyzed using the newly set spectrometer in the TARLA system.

The sample was excited by an 800nm laser pulse with a fluence of 700 μJ/cm^2 for THz conductivity behavior and then probed using THz light. The resultant transient response is presented in Figure 5.24. Similarly, the rise time was around 3 ps with 800 nm excitation. That is followed by a sharp decay due to the cooling and recombination of the carriers. Finally, a significant quantity had lived as a free carrier similar to MLG on PVC and MLG850 on quartz. Interaction of the free carriers with the significant mean free path was observed as the long-living tail in the transient response. However, the sample's carrier lifetime response exceeded our experimental limit of approximately 0.5 ns.

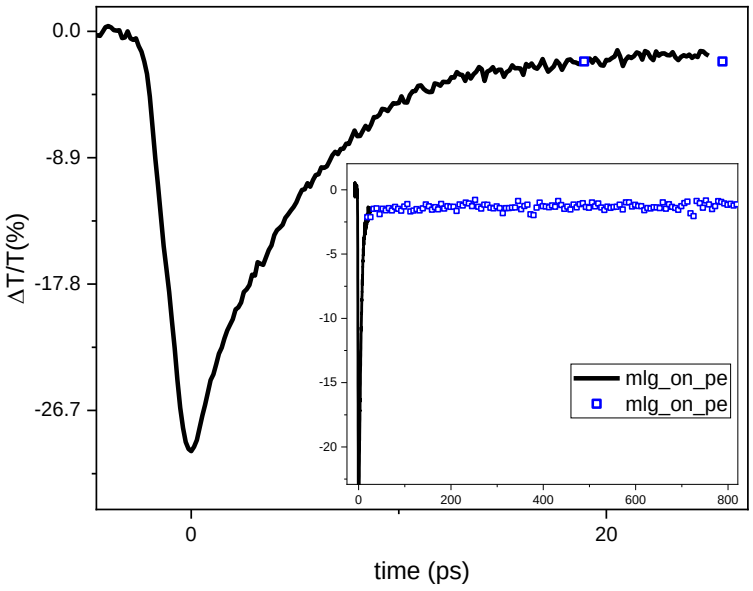

Figure 5.24. Differential THz transmission, $\Delta T/T_0$, of MLG on PE as a function of pump–probe delay recorded at a fluence of 700 μJ/cm^2 for 800nm excitation. Inset shows the long scans covering up to 450 ps time scale and enables the observation of long-lived carrier dynamics.

CHAPTER 6

2D MATERIALS-PART Ⅱ

This chapter focuses on the time-domain and time-resolved responses of 2D transition metal dichalcogenide films comprising $MoSe_2$+$PtSe_2$ (Sample 2705) or WSe_2 (Sample 2706) coated in Mica substrate by CVD technique. The details of the samples are given in Chapter 3. Terahertz Time-Domain Spectroscopy (THz-TDS) studies were carried out on four samples: Air, Mica, and two samples, 2705 and 2706. This allowed us to analyze the samples' optical properties and understand how they respond to optical excitation. In addition, we conducted Time-Resolved Terahertz Spectroscopy (TRTS) measurements for all samples, including Mica. Transient responses of the samples were collected with two excitation colors: 400nm and 800nm ultrashort laser pulses. This helped us determine their response to optical excitation and compare them with THz-TDS results. Overall, our study provides valuable information about the optical properties of these samples and their response to photoexcitation.

6.1 2D Transition metal chalcogenide films on mica substrate - sample #2705

The sample numbered 2705 consists of substrate mica, 1 layer of $MoSe_{2\ on}$ mica, and 2 layers of $PtSe_2$ on top of those. The time domain response of sample 2705 is presented in Figure 6.1. substrate causes a shift in time associated with its refractive index and thickness. Similarly, the sample also showed a delay in time. However, it is worth noting that the shift for the sample is more remarkable compared to other substrates due to its higher Mica thickness. Unfortunately, the reference substrate is

about 150 µm while the sample is 170 µm. Thus, the observed delay was corrected for the mica substrate, showing no difference in the delay time since the sample layer is too thin. (Figure 6.1) The loss in the THz amplitude is the transmission loss due to the absorption and reflection of the semiconducting thin film. Reflection in the measured sample results in a reflection signal correlated with the index and its thickness.

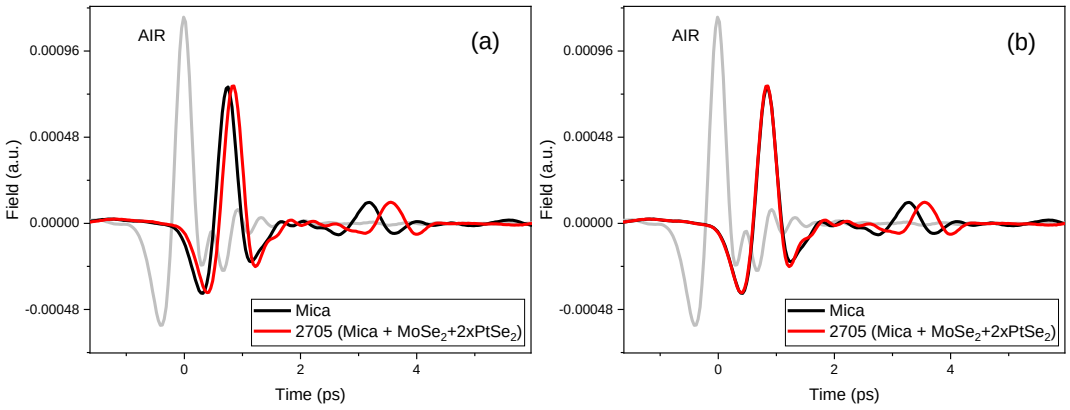

Figure 6.1. THz-TDS Time-domain profiles of a) substrate Mica and samples of 2705 as collected, b) substrate profile was thickness corrected.

The extracted refractive index and extinction coefficient of the substrate mica and 2705 are presented in Figure 6.2. it can be inferred that Mica and the sample exhibit minimal THz radiation absorption (almost zero extinction coefficient). This suggests that the material composition of mica is less likely to hinder or interfere with the transmission of THz radiation. The implication of this finding could be significant for applications that require terahertz radiation, such as in medical imaging or security screening, as these materials may prove helpful in minimizing any interference with the transmission of the radiation. Mica and 2705 are two different materials with distinct refractive indices. Mica has an average refractive index of around 2.5, and its refractive index spectrum is almost flat in the 0.1-1.4 THz range.

On the other hand, sample 2705 has a nearly featureless and flat refractive index spectrum, with an average index of around 2.7 in the same frequency range.

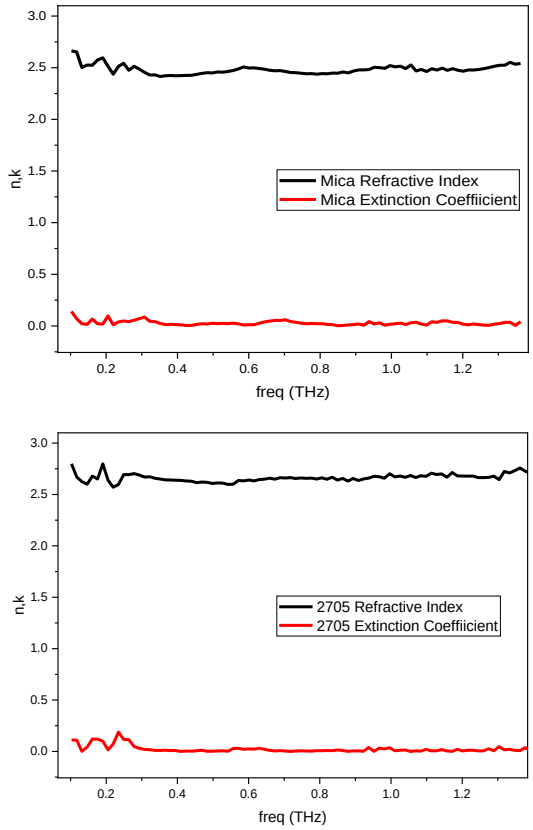

Figure 6.2. Refractive index and Extinction Coefficient of (a) Mica substrate and (b) 2705 sample

The THz dynamics of 2705 are presented in Figure 6.3, the detailed analysis of which is available in Chapter 7. The sample was excited by ultrafast pulses of 400 and 800nm with 195 μj/cm^2 and 255 μj/cm^2 fluences and probed using a THz beam. The data suggests that the noise level is similar to the sample response, even though multiple measurements were taken to minimize noise interference; thus, smoothing of the signal was required. The dots are the collected data, while the line in the Figure

is smoothed with a 20-point average Savitzky-Golay filter. When excited with 400 nm light, the sample exhibited an initial response with a rise time of approximately 1 ps and a fall time of around 1 ps. Conversely, when excited with 800 nm light, the sample displayed a faster rise time of about 0.36 ps and a similar fall time of about 1 ps. Despite both excitations resulting in a relatively low THz conductivity, the conductivity was higher for the 800 nm excitation due to the greater density of states available for the $PtSe_2$.[103]

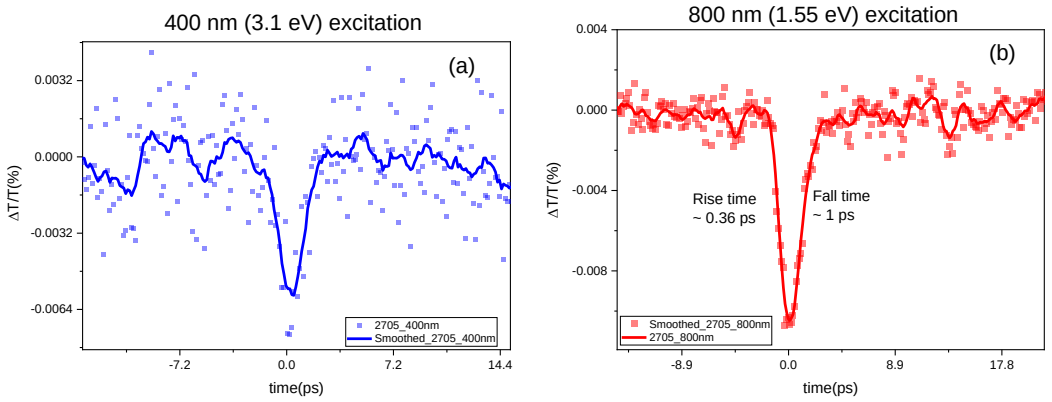

Figure 6.3. Differential THz transmission, $\Delta T/T_0$, of Sample 2705 as a function of pump–probe delay recorded **a)** at a fluence of 195 $\mu J/cm^2$ for 400nm excitation and **b)** at a fluence of 255 $\mu J/cm^2$ for 800nm excitation.

6.2 2D Transition metal chalcogenide films on Mica substrate-sample #2706

Sample 2706 consists of substrate mica coated with 3 layers of CVD-grown WSe_2 transferred to mica. The time domain response of the sample is presented in Figure 6.2. the sample substrate causes a shift in time due to its refractive index; however, the amount of shift for the sample is more significant due to having higher Mica thickness. The same graph suggests a slight intensity distortion for the sample signal

for the main pulse and the tail of the pulse. The greater loss in THz beam amplitude is because of absorption and reflection of the thin film.

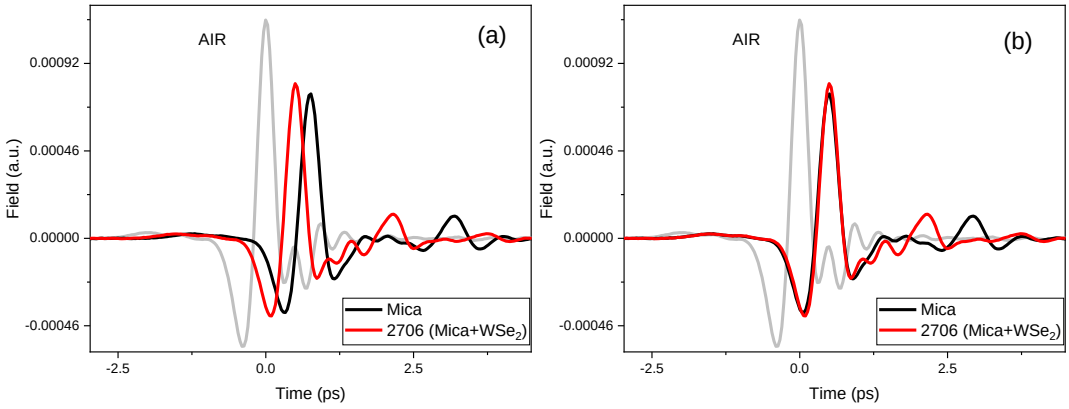

Figure 6.4 THz-TDS time-domain profiles of **a)** substrate mica and the Sample 2706 as collected, **b)** substrate profile was thickness corrected.

The extracted refractive index and extinction coefficient of Sample 2706 are presented in Figure 6.5 compared to the Mica data given in Figure 6.4. Similar to Sample 2705, it can be concluded that Sample 2706 has almost zero terahertz radiation absorption. Also, Sample 2706 showed a distinct refractive index with a nearly featureless and flat refractive index spectrum, with an average index of around 2.7 in the same frequency range, almost the same results as Sample 2705. There is an apparent increase in the THz amplitudes; however, that is most likely associated with the much lower thickness of the sample (90 μm) compared to the reference substrate (150 μm).

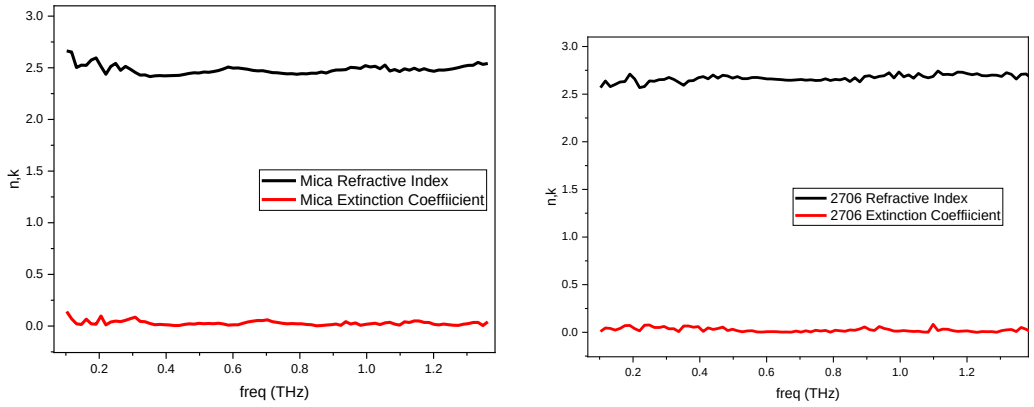

Figure 6.5. Refractive index and Extinction Coefficient of **a)** the Mica substrate and **b)** the Sample 2705

The THz dynamics of 2706 are presented in Figure 6.6, the detailed analysis of which is available in Chapter 7. This sample was also excited by ultrafast pulses of 400 nm and 800 nm with fluences of 195 μj/cm^2 and 255 μj/cm^2, respectively, and probed using a THz beam. Unfortunately, the signal level was too low, comparable to the noise response. Thus, multiple measurements (10 to 15 scans) were taken to minimize noise interference. Later, the data is also smoothed with a 20-point average Savitzky-Golay filter. After exposure to 400 nm light, the sample responded with an initial rise time of approximately 1 picosecond, followed by a fall time of about 1 picosecond. In contrast, when exposed to 800 nm light, the sample showed a more rapid rise time of around 0.36 picoseconds and a comparable fall time of about 1 picosecond. The responses were similar to those of Sample 2705. In addition, the responses are similar to the graphene, though the levels are much weaker, possibly due to the inability to generate carriers as much as graphene. Even though both excitations resulted in a relatively low THz conductivity, the conductivity was higher for the 400 nm excitation because the WSe_2 had a higher density of states available.[103]

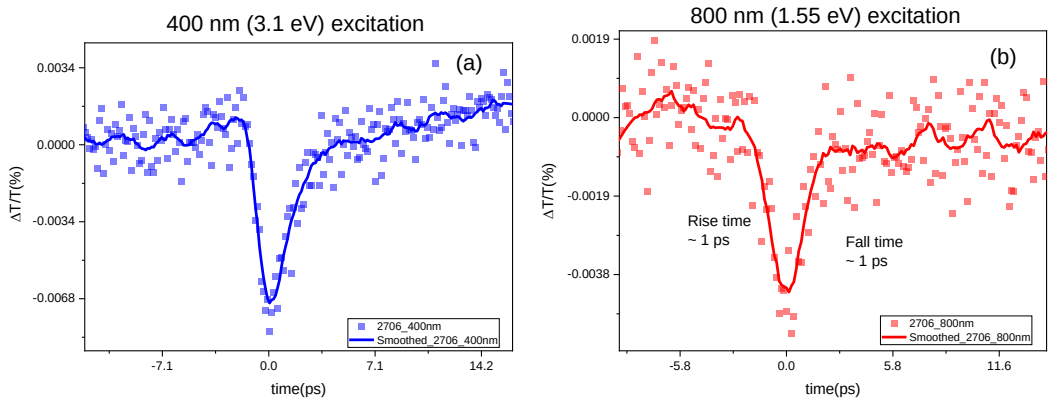

Figure 6.6. (a) 400nm (3.1 eV) and (b) 800nm (1.55eV) pump THz probe differential spectrum of 2706 sample

CHAPTER 7

TIME-RESOLVED STUDIES

Our research employed a powerful combination of Time-Resolved THz Spectroscopy (TRTS) and Transient Absorption (TA) techniques. We aimed to investigate the behavior of photoexcited charged species in 2D materials: Single and Multi-Layer Graphene samples and 2D Transition Metal Dichalcogenide (TMDC) samples. By utilizing these techniques, we could observe these species' dynamics with high precision and gain valuable insights into their behavior. We used 400nm light of ca. 1mW to excite the sample for TA studies. White light was then used as the probe beam to investigate the resultant changes in the sample. During TRTS measurements, however, 400 nm and 800 nm light were used as pump lights to excite the sample and create charge carriers. The transmitted THz radiation was then detected as the probe beam. Here, the change in THz transmission is monitored to study the ultrafast dynamics of the sample. This will lead to the transient evolution of the sample's free carriers. In this context, the phrase "charge species or charge carriers" refers to various types of charged particles, mainly free electrons and holes. Additionally, the term encompasses the correlation between charges, such as excitons - bound electron-hole pairs - and charged excitons (trions) and plasmons.

The details of the samples whose results will be presented in this part of the study are given in the experimental part. In short, graphene samples are either single layers or multilayers on various substrates. The multilayer graphene samples MLG850, MLG900, MLG950, and MLG100 consisted of 30, 50, 70, and 100 graphene layers on quartz 30 and 32 layers on PE and PVC substrates, respectively. The two thin film

samples of 2D TMDC are 2 layers of $PtSe_2$ on 1 layer of $MoSe_2$ on mica substrate and 3 layers of WSe_2 on mica substrates.

7.1 Fluence on Single-Layer Graphene

The fluence applied in a pump-probe measurement is crucial for several reasons. Firstly, the applied sample or substrate could be damaged by applying too much photon density. Also, the sample response for photoexcitation could change linearly up to a certain limit.

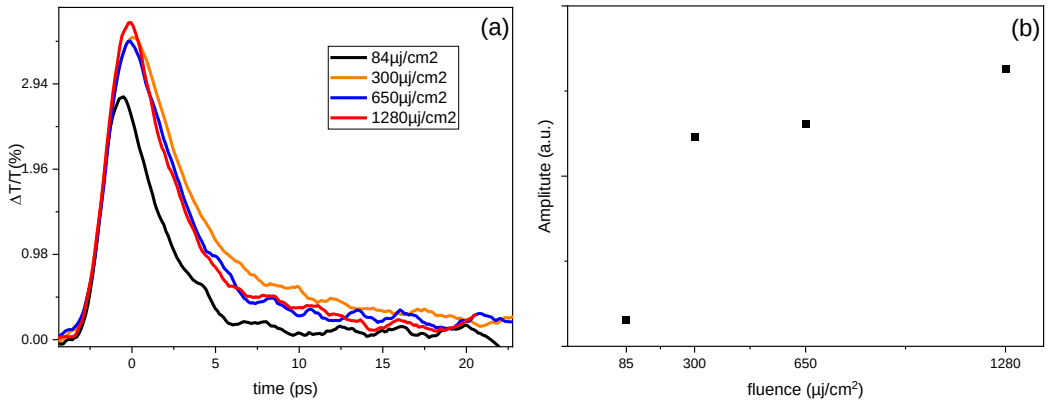

Figure 7.1 (a) Differential THz peak transmission response of SLG sample on Si/SiO_2 at pump fluences of 84, 300, 650, and 1280 µj/cm^2 (b) peak amplitude vs fluence showing saturation after 300µj/cm^2

Figure 7.1(a) represents the differential THz peak dynamics upon excitation with fluences of 84, 300, 650, and 1280 µj/cm^2. With the changing fluence of the optical gating, the rise time of the sample was roughly the same after 300 µj/cm^2 pump fluence: 0.73ps, 0.96ps, 0.91ps, and 0.93 ps.

On the other hand, the lifetime of hot carriers tends to increase steadily from 2.49ps, 2.97ps, 2.98ps, and 3.53ps with increasing fluence that could result from steadily increasing momentum of the carriers with increasing number of photons exposed.

Figure 7.1 (b) reveals the peak THz amplitude change with respect to different fluences. As the figure suggests, after 300μj/cm^2, saturation occurs; therefore, for the rest of the measurements, the applied fluence remained the same as 300μj/cm^2.

7.2 Single-layer graphene on Polydimethylsiloxane

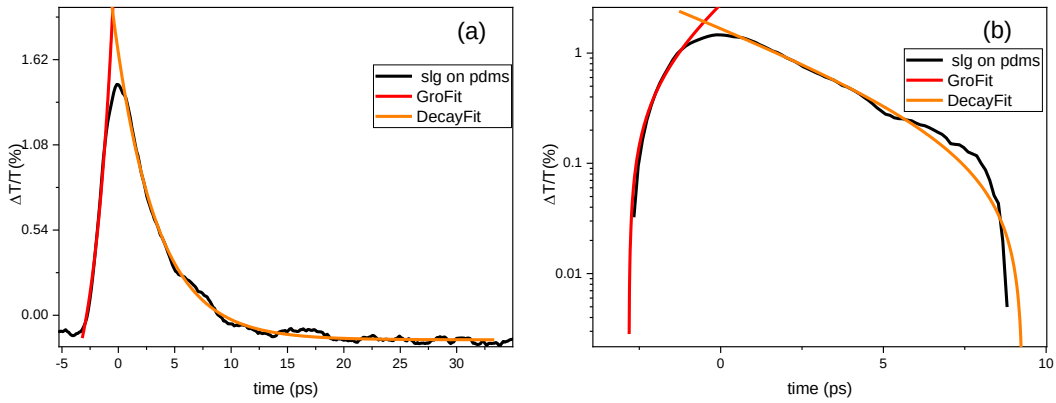

Figure 7.2 (a) Differential THz transmission, $\Delta T/T_0$, of SLG on PDMS as a function of pump-probe delay recorded at a fluence of 300 μJ/cm^2.(b) Differential THz transmission, $\Delta T/T_0$, of SLG on PDMS as a function of pump-probe delay recorded at a fluence of 300 μJ/cm^2 in logarithmic scale for showing decay time better.

As shown in Figure 7.2(a), when the sample was excited, its THz conductivity decreased due to its metallic-like nature. When the pump pulse is applied, the carrier density doesn't increase much, but the charge carriers scatter more among

themselves, causing a reduction in THz conductivity. This sample shows a highly rapid and precise response, indicating its excellent performance characteristics. The rise time of the sample is approximately 1.85 picoseconds, suggesting that it can respond to changes in the input signal very quickly. This makes it also suitable for high-speed applications requiring fast and reliable switching. The relaxation of carriers in a given system can be characterized using a monoexponential decay line. The figure also depicts the relaxation process, and the decay time of the line is determined to be $\tau_1 = 3.77 \pm 0.04$ ps. The carriers have low mobility and a relatively short lifetime of around 8 ps, which could be seen in Figure 7.2(b) due to structural imperfections and traps present on the substrate.

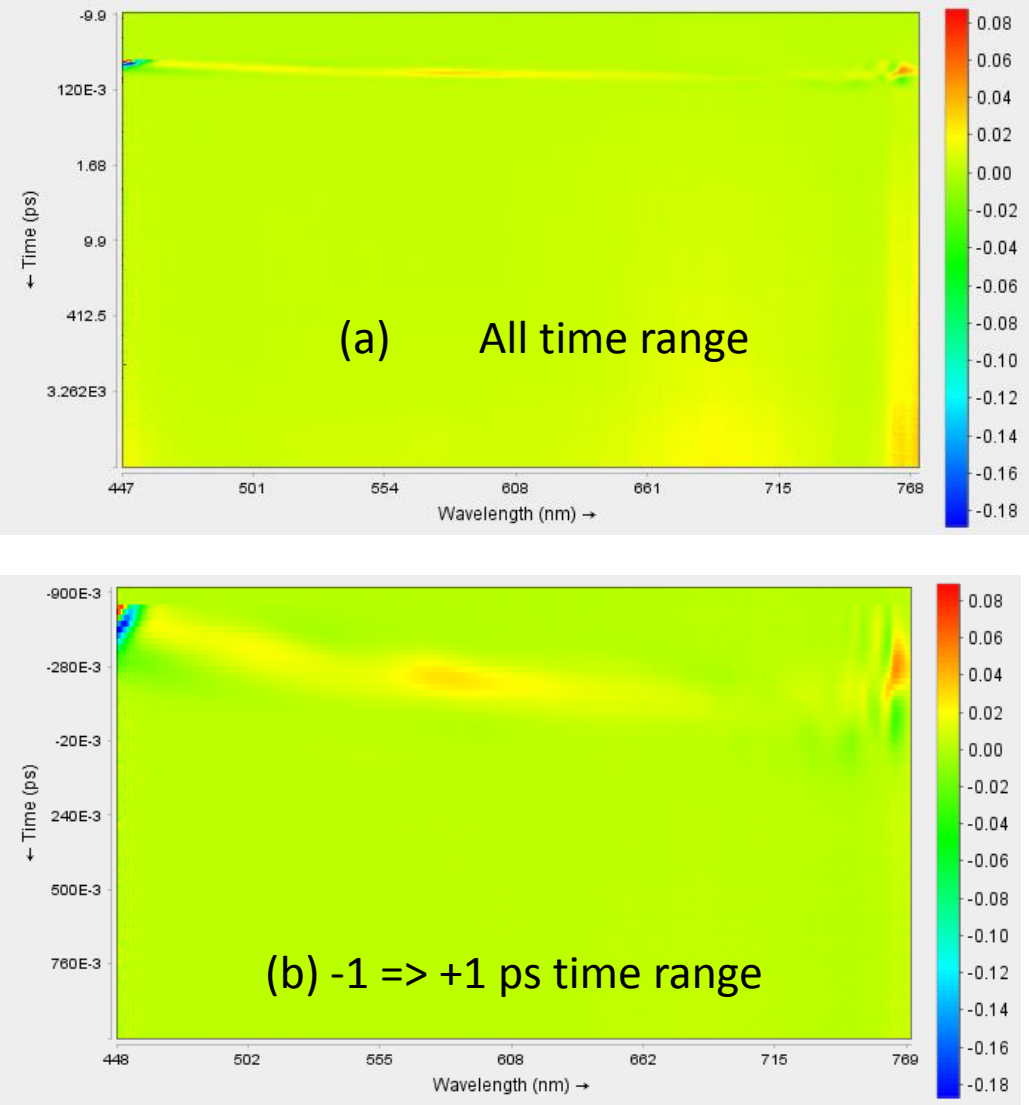

Figure 7.3. (a) and (b) TAS contour plot spectrum of 400 nm excited SLG on PDMS at visible (white) probe wavelengths in ~7ns and 2 ps timespan respectively

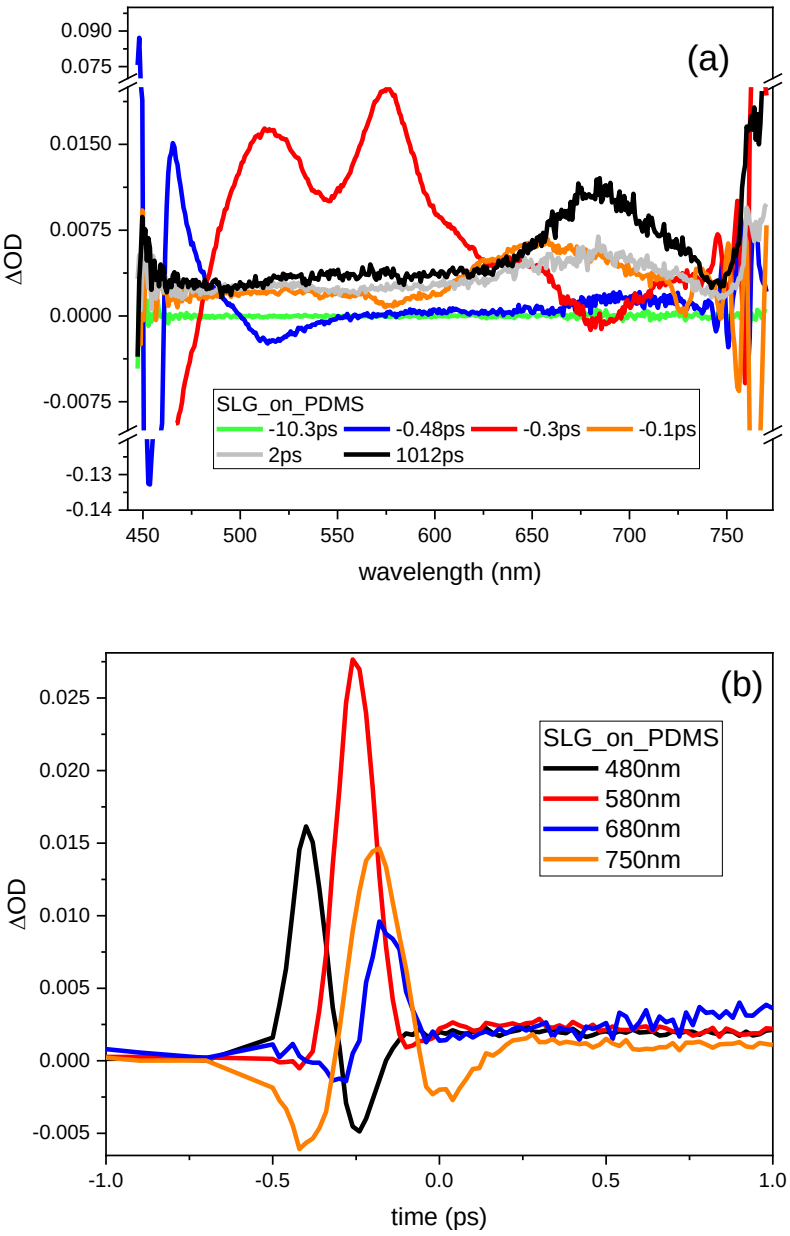

Figure 7.4. (a) Transient spectra in the visible range (b) Pump-induced transmission of different photon energies, 480nm, 580nm, 680nm, and 750nm of 400 nm excited SLG on PDMS at visible (white) probe wavelengths in ~7ns timespan

Figure 7.3 (a) and (b) represent comprehensive TAS data shown as contour plots, Figure 7.4 (a) shows the transient spectra at different delay times, and (b) illustrates the extracted dynamic traces for 480nm, 580nm, 680nm, and 750 nm. In plots Figure 7.3 (a) and (b), the y-axis shows the time in ps, whereas the x-axis displays the probe wavelengths in the visible range of the EM spectrum. As the figures suggest, the electron (hole) distributions were located at higher (lower) energies [104]; therefore, the bleaching was more dominant at shorter wavelengths. In addition to this, the negative ΔOD values at especially shorter wavelengths around 450nm in Figure 7.4 (a) also imply that the signal bleaching became more dominant for those wavelengths. On the other hand, in Figure 7.4 (b), the probe responses for the given wavelengths were different from each other. For the 480nm probe, the pump response initially caused increased absorption, followed by a positive ΔOD component. The initial increase in the ΔOD signal was attributed to the incorporated oxygen into the graphene structure.[105] The following negative component was most likely caused by intraband absorption due to the bleaching. [106] The negative component disappeared for 580 nm but started to appear for 680 nm and became more apparent at 750nm. For 680nm and 780 nm, the initial negative component was due to pump-induced bleaching of the transition, and the positive part was most likely due to intraband absorption.

7.3 Single-layer graphene on polyethylene terephthalate

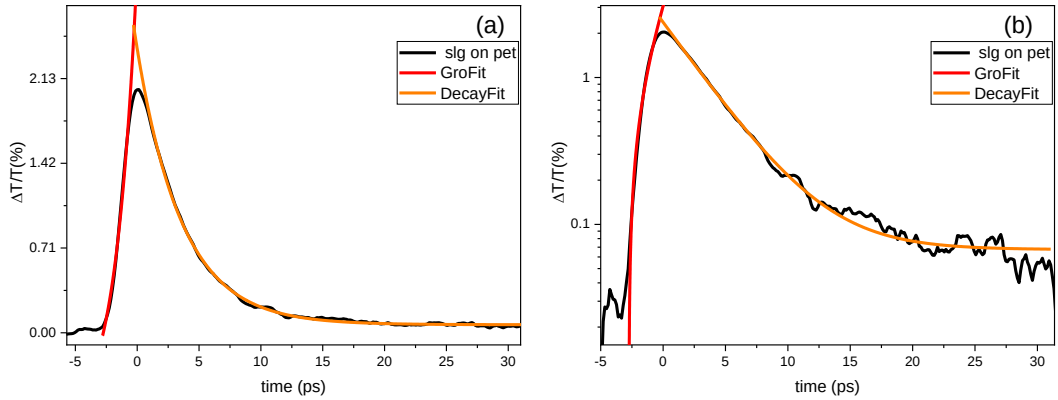

Figure 7.5 (a) Differential THz transmission, $\Delta T/T_0$, of SLG on PET as a function of pump–probe delay recorded at a fluence of 300 μJ/cm^2 for 800 nm pump. (b) Differential THz transmission, $\Delta T/T_0$, of SLG on PET as a function of pump-probe delay recorded at a fluence of 300 μJ/cm^2 for 800 nm pump in logarithmic scale for showing the decay time better

Figure 7.5(a) presents the response of SLG on a dielectric substrate PET upon photoexcitation with a fluence of 300 μJ/cm^2 for an 800nm pump. Unlike the transient behavior of many of the semiconductors where an initial decrease in THz transmission would occur, and recovery would follow as stated in the theoretical part of this thesis, here, however, we observed a sharp increase in transmission of THz light at first and then recovery to the original THz transmission level. In general, this can be attributed to two different phenomena. First, if a substance has absorption and its absorption decreases upon excitation, that would lead to an increase in THz transmission until the recovery of the excited electrons. The observed recovery, in general, was either single or multi-exponential. The second one was related to the number of free carriers of the semiconducting materials. Free carriers in a

semiconductor would scatter within the sample with respect to their mobility and mean free paths. The scattering frequency of the carriers was in the same order of magnitude in frequency as the THz light. Thus, it hindered the THz transmission. Therefore, when there was an increase in carrier amount, the loss would increase or, in other words, the transmitted THz light would decrease. When there was a decrease in free carrier amount, an increase in THz transmission would be observed, as in this case. Such an increase was only possible if the material had a metallic characteristic. Since we observe an increase in THz transmission in this graphene sample on PET, we may suggest that the graphene here has a metallic nature. This is a known phenomenon and has also been observed in many other studies.[99] The carriers will scatter and recombine over time once the carriers are generated. Thus, the transient study will result in detailed information on the generation cooling of hot carriers and the recombination dynamics.

The observed response was generally proportional to the number of free carriers and their mobilities. One should also consider the cooling process of the carriers, which are hot right after photoexcitation. The added kinetic energy to the free carriers increases their temperatures and, thus, their mobilities and scattering rates. Therefore, in the early times, the transient response of the rise and the recovery comprised carrier generation, the carrier cooling process, and carrier recombination or trapping. Thus, the first few ps after the photoexcitation are quite complex, and deciphering the processes within this time scale requires careful experimental measurements with a high S/N ratio. In addition, one should consider secondary techniques, such as transient absorptions as a complementary technique for transient behaviors. Therefore, in these studies, we would mainly concentrate on the free carriers' time evolution after the cooling process, which is usually about 1-2 ps[107] or so. Considering fixed mobility for the carriers after cooling, the observed signal level of THz transmission change is directly proportional to the carrier numbers.[107]

The SLG on PET displays a highly rapid response, indicating outstanding performance characteristics, as presented in Figure 7.5a. The rise time of the sample was recorded to be approximately 1.74 ps. This value suggests that the sample can respond to changes in the input signal in a very short time scale, making it suitable for use in high-speed applications that require fast and reliable switching. On the other hand, the free carrier recombinations (the decay dynamics) did take a while, as expected. The relaxation of carriers was characterized using a single exponential decay line with a decay time, τ, of 3.64±0.02 ps. In general, due to the high mobility of the graphene and the long perfect structural 2D conjugation, the free carrier lifetimes were much longer with low scattering rates and high mean free paths. However, the number of carriers left was significantly low, around 30 ps in this sample. This was most likely due to structural imperfections and traps on the graphene structure. This might be due to the production processes or a substrate effect on the graphene properties. In short, the carrier generation rate appears to be quite high; however, the carrier recombination rates of free carriers are also very high; thus, very few long-lived carriers are left beyond 50 ps.

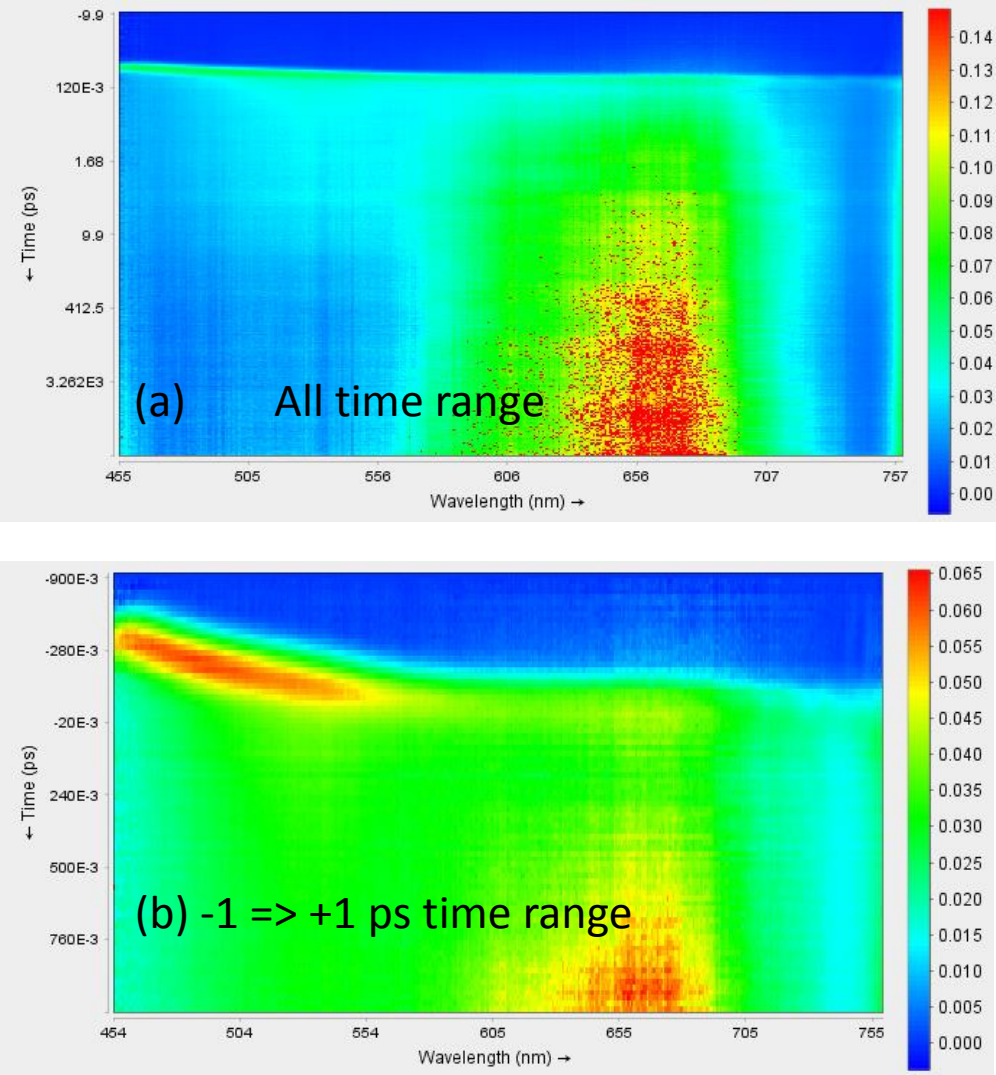

Figure 7.6. (a) and (b) TAS contour plot spectrum of 400 nm excited SLG on PET at visible (white) probe wavelengths in ~7ns and 2 ps timespan respectively

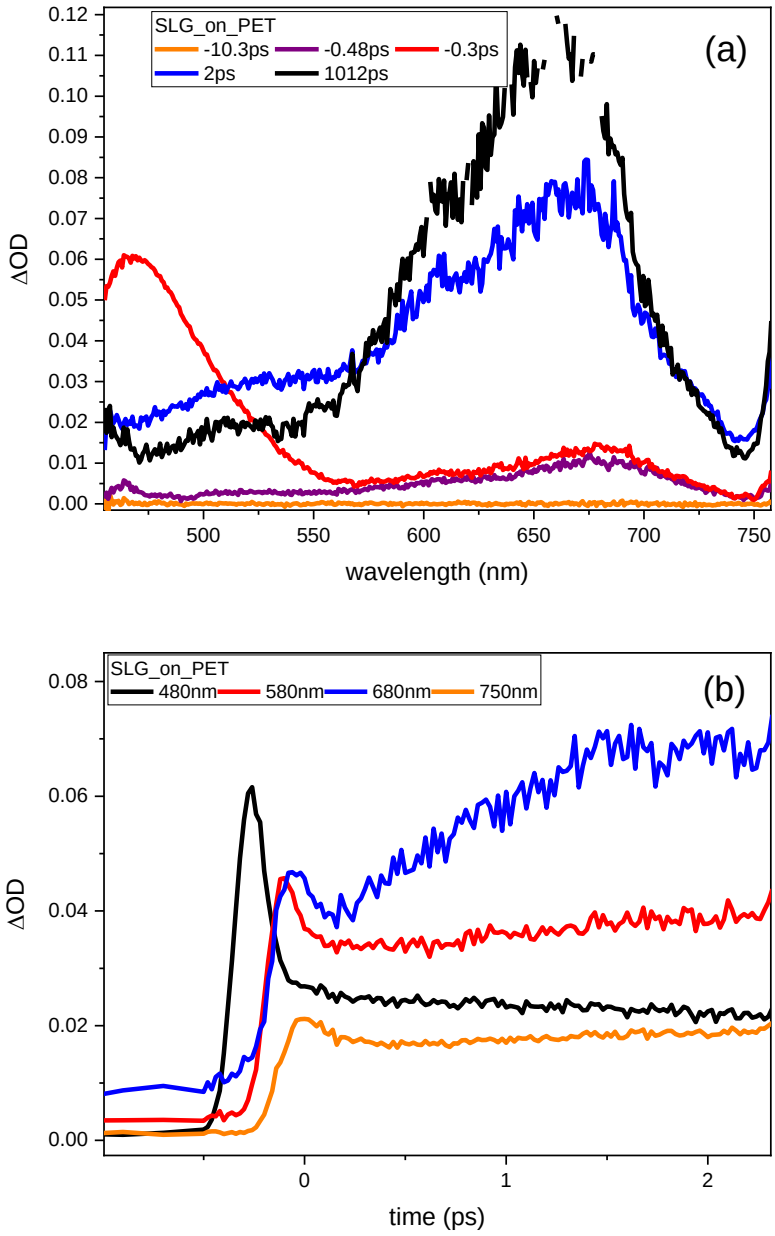

Figure 7.7. (a) Transient spectra in the visible range (b) Pump-induced transmission of different photon energies, 480nm, 580nm, 680nm, and 750nm of 400 nm excited SLG on PET at visible (white) probe wavelengths in ~7ns timespan.

Figure 7.6(a) and (b) represent comprehensive TAS data shown as contour plots, Figure 7.7(a) shows the transient spectra at different decay times, and (b) illustrates the extracted kinetic traces for 480nm, 580nm, 680nm, and 750 nm. In plots Figure 7.6 (a) and (b), the y-axis shows the time in ps, whereas the x-axis displays the probe wavelengths in the visible range of the EM spectrum. As (a) and (b) suggest, this sample has no bleaching caused by the pump. Figure 7.7 (a) shows that the transient absorption increases for the wavelength close to the pump wavelength of 400nm at very early times. It is expected that after the excitation with 400nm, electrons might be further excited at the excited states. As time progressed, the transient absorption increased for the longer wavelengths as the excited electrons relaxed in the conduction band. Figure 7.7 (b) shows the changes in OD of selected wavelengths as the time progressed after photoexcitation. As the figure suggests, at early times, high-energy transitions became dominant, and low-energy transitions (observed at longer wavelengths) started to be observed as the electron relaxes in the conduction band. One noticeable observation was that none of the transitions decayed quickly and lived beyond a few picoseconds.

7.4 Single-layer graphene on a blend of polymethyl methacrylate and polydimethylsiloxane

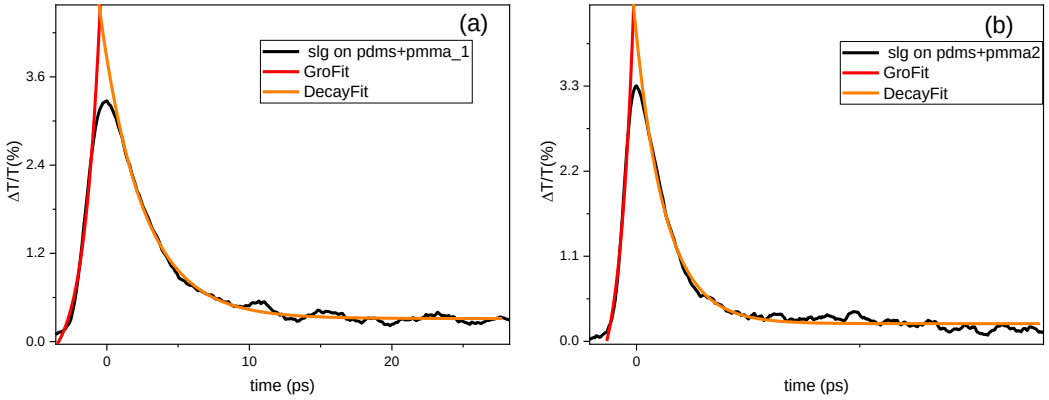

Figure 7.8 Fitted Differential THz transmission, $\Delta T/T_0$, of a) smaller size sample of and b) larger size sample of SLG on blend PDMS/PMMA as a function of pump-probe delay recorded at a fluence of 300 μJ/cm^2

Based on Figure 7.8(a), when sample 1 was excited, its THz conductivity decreased due to the metallic nature of the SLG material. Upon application of the pump pulse, the carrier density did not increase significantly, but the charge carriers scattered more, which reduced THz conductivity. This sample demonstrated a highly rapid and precise response, indicating its excellent performance characteristics. The rise time of the sample was approximately 1.16 ps, suggesting that it can respond to changes in the input signal very quickly. This makes it suitable for high-speed applications that require fast and reliable switching. The relaxation of carriers in a given system can be characterized by using a monoexponential decay line, with the figure depicting the relaxation process. The decay time of the line was determined to be $\tau = 2.97 \pm 0.04$ ps. Due to the presence of structural imperfections and traps on the

substrate, the carriers have low mobility and a relatively short lifetime of around 30 ps.

Sample 2 also showed behavior similar to sample 1, as presented in Figure 7.6(b), with a rise time of 1.61ps and a time constant of τ_1=3.36±0.04. It could be concluded that the samples had differences in conductivity properties even though their substrates and way of preparation were the same.

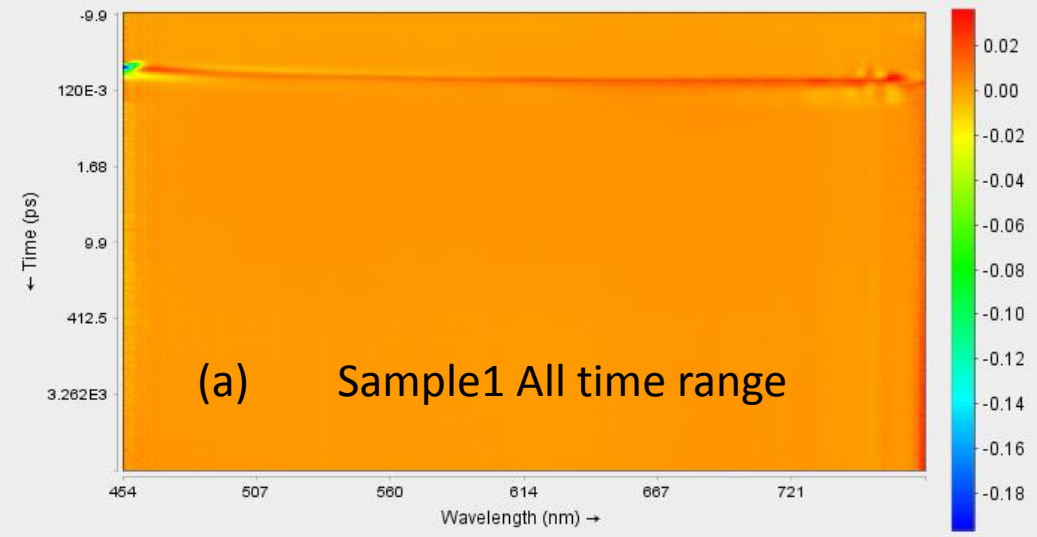

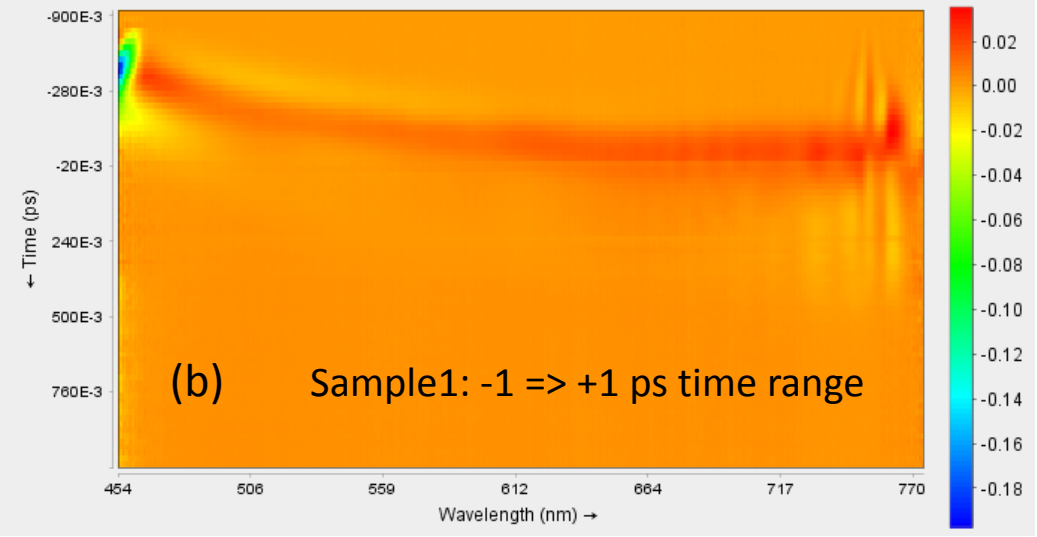

Figure 7.9. (a), (b), TAS contour plot spectrum of 400 nm excited SLG on blend of PMMA+PDMS of sample-1 in 7ns and 2 ps timespan respectively

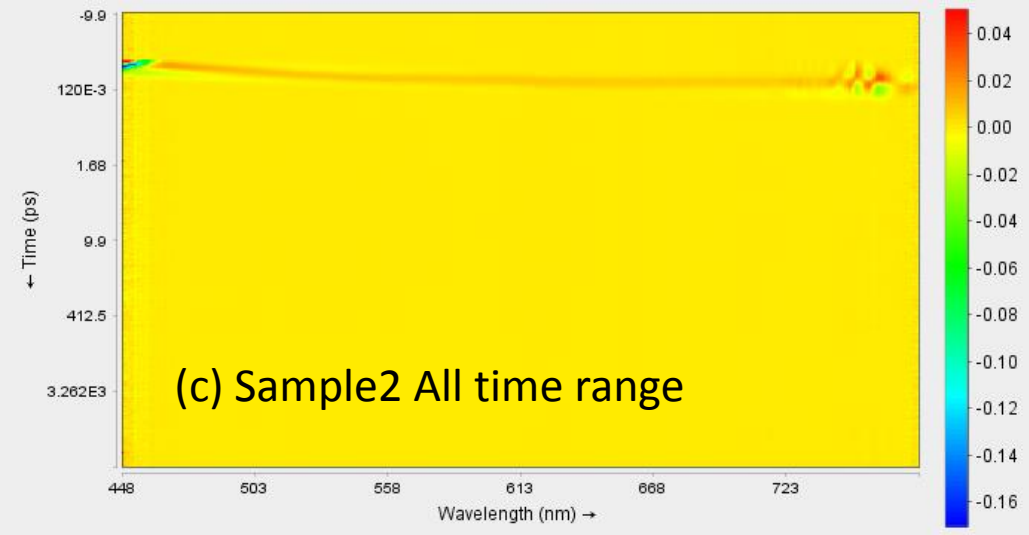

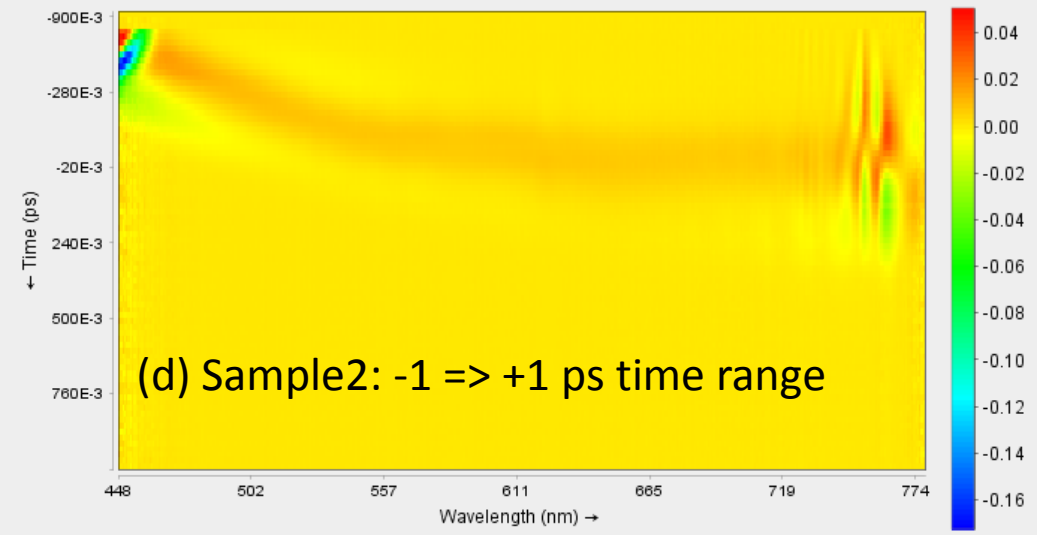

Figure 7.10. (a), (b), TAS contour plot spectrum of 400 nm excited SLG on blend of PMMA+PDMS of sample-2 in 7ns and 2 ps timespan respectively

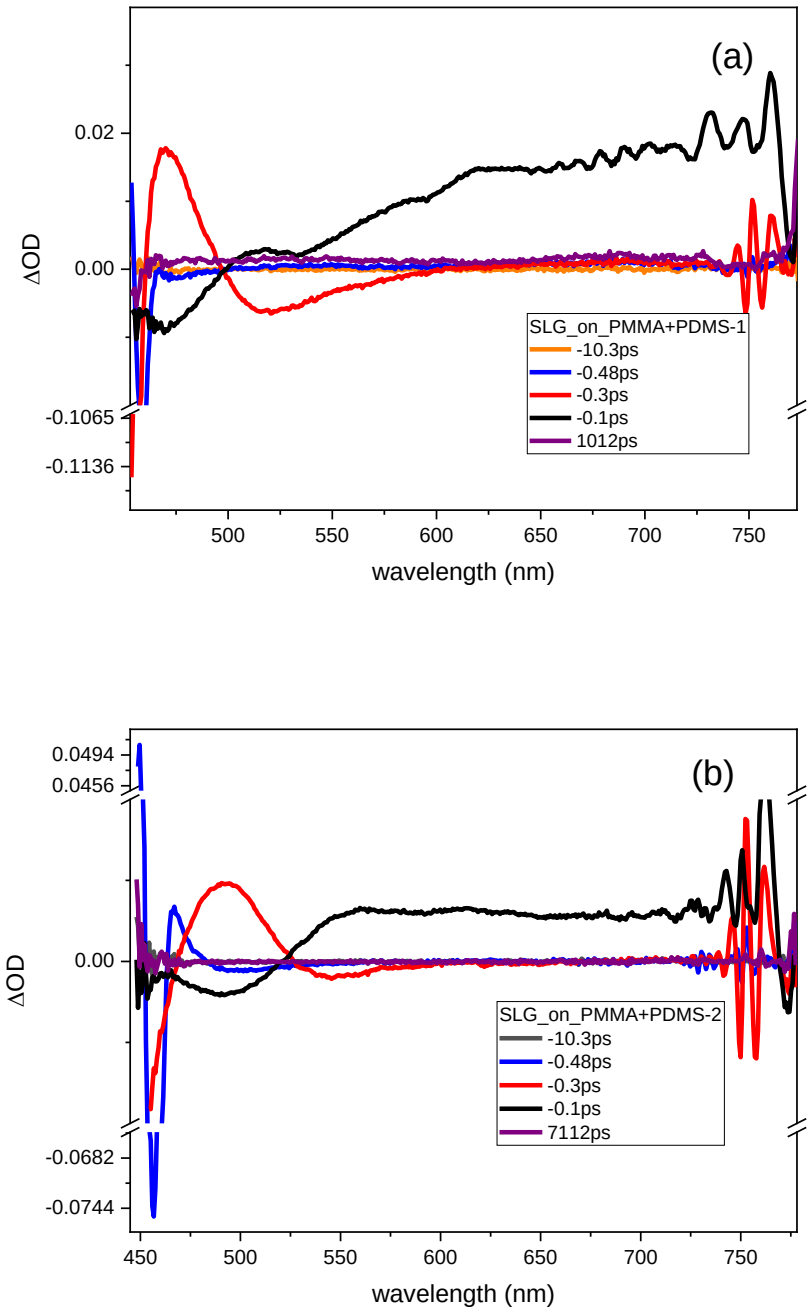

Figure 7.11. (a), (b) Transient spectra in the visible range for different time scales for SLG on PMMA+PDMS of sample-1 and 2 respectively.

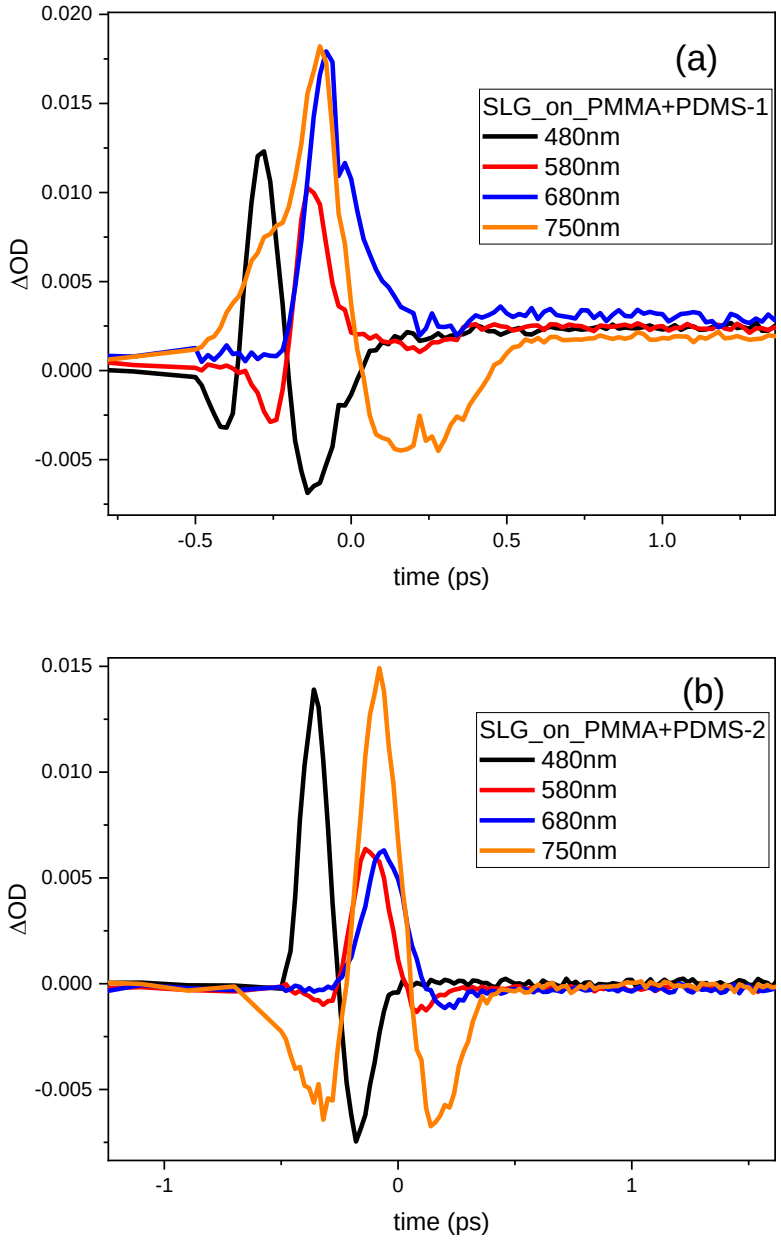

Figure 7.12. (a), (b) Pump-induced transmission at different photon energies, 480nm, 580nm, 680nm, and 750nm for SLG on PMMA+PDMS of sample-1 and 2 respectively.

Figure 7.9(a), (b) and Figure 7.10 (a), (b) show comprehensive TAS data as contour plots for samples 1 and 2. Figure 7.11 (a) (b) display the transient spectra at different time scales, and in Figure 7.12 (a), (b) extracted kinetic traces for 480nm, 580nm, 680nm, and 750 nm are illustrated. For samples 1 and 2, plots in Figure 7.9 and Figure 7.10 display time in the y-axis in ps, whereas the x-axis shows the probe wavelengths in the visible range of the electromagnetic spectrum. According to the figures, the electron (hole) distributions are located at higher (lower) energies for both samples.[104]; The dominance of bleaching was more evident at shorter wavelengths. Figure 7.11(a), (b) show negative ΔOD values, particularly around 450nm, indicating that the signal bleaching became more dominant at these wavelengths. However, the probe responses for the given wavelengths differ in Figure 7.12 (a), (b). For sample 1, the 480nm probe, the pump response initially causes a decrease, followed by an increase and a reduction in ΔOD. For this sample, we could say that the initial decrease could be attributed to pump-induced bleaching of the transition, and the aftercoming increase could point to intraband absorption. The second negative part of the signal again shows a decrease in OD due to the excitation of those states via the emissions of the excited electrons. For sample 2, on the other hand, the transient of the 480 nm spectrum showed an initial increase, which could be ascribed to the oxidized structure of the graphene.[105] The following negative component was most likely caused by intraband absorption due to bleaching caused by the pump.[106] The negative component disappeared for 580 nm but started to appear for 680 nm and became more apparent at 750nm. For 680nm and 780 nm, the initial negative component was due to pump-induced bleaching of the transition, and the positive part was most likely due to intraband absorption, and later negative responses were possibly from the valance band excitation by the emitted photons of the interband transitions in the conduction band during the relaxation of the excited electrons.

7.5 Comparison of SLG on PET, PDMS, and PMMA-PDMS substrates

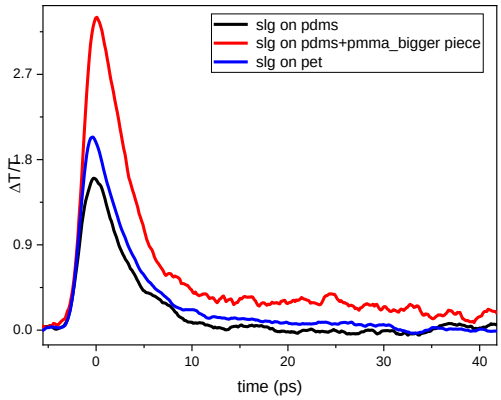

Figure 7.13 SLG sample comparison for their differential THz peak transmission

As Figure 7.13 suggests, SLG samples on the PDMS+PMMA blend resulted in a better THz conductivity and initial response to optical gating, indicating that the graphene quality on this blend substrate was higher. The higher quality could stem from fewer structural imperfections of the blend with fewer traps, resulting in better organization of graphene on top.

7.6 Epitaxial single-layer graphene on silicon carbide

There are 2 SLG on SiC substrates. These SLG samples are homogeneous in the middle 4mm circular part; therefore, an iris with appropriate aperture was used during all the measurements.

The dynamic properties of the samples were measured by pumping them with 800 nm light. For this purpose, the samples were excited with 490 mW light at Terahertz peak amplitude, and the pump was delayed to observe carriers' decay (expectedly), as presented in Figure 7.14.

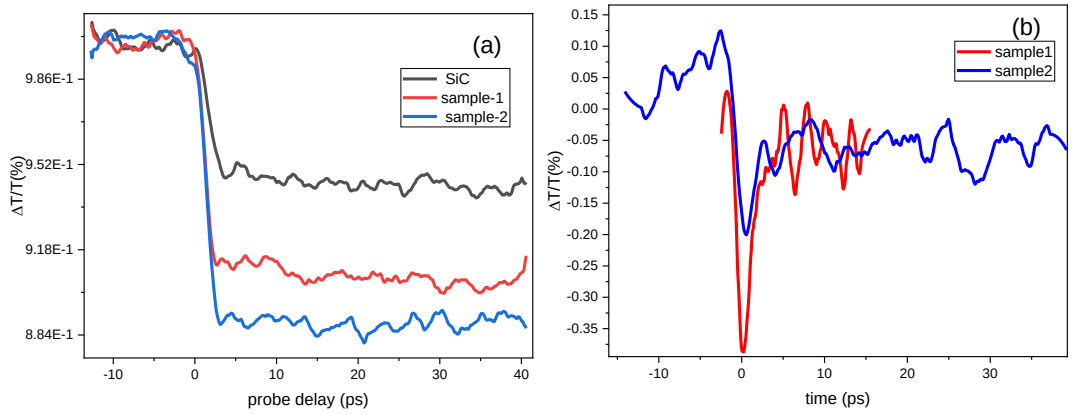

Figure 7.14. a) Differential THz transmission, $\Delta T/T_0$, of two samples of SLG on SiC and a SiC reference sample as a function of pump–probe delay recorded at a fluence of 300 μJ/cm^2. b) The derived response of the SLG layer relative to the SiC.

Figure 7.15 shows that peak amplitude remains as steady as the noise level allows before the pump light hits the sample from ~ -340 ps THz. As the pump arrived at ca. -340 ps, the carriers evolved, resulting in a decrease in the transmitted THz peak. The carriers evolved but did not decay quickly; instead, they seemed to stay constant in time, which is the behavior of semiconductors, namely SiC. We needed to extract the decay of SLG carriers from these graphs by processing the signal for all graphs to subtract the substrate response for extracting the sample spectrum from the reference spectrum, resulting in Figure 7.15. As the Figure presents, the carriers began to evolve around -340 ps, and after reaching a peak, they started decaying in ca. 1.5 ps.

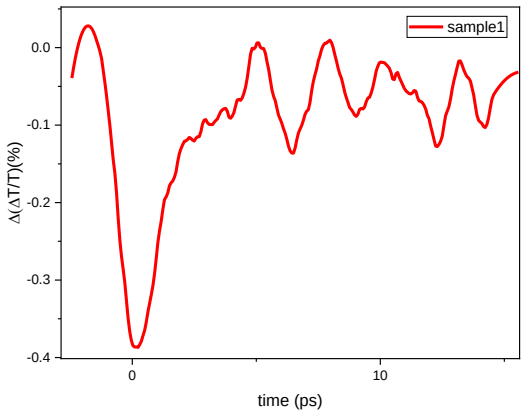

Figure 7.15 THz peak amplitude change for the SLG sample1 itself

Here, an unexpected behavior is observed by SLG, which is typical for bilayer or multilayer Graphene samples. Frenzel et al. showed that the transmitted THz signal increased in intensity upon optically pumping the sample with 800 nm light. [108] He suggests that this behavior results from increased electron-phonon scattering and population inversion by the pump that can amplify the THz probe pulse by stimulated emission. The SiC substrate, a semiconductor, may cause the unexpected behavior. Another possibility is that the SLG sample may be a bilayer or multilayer graphene. Indeed, a buffer layer consisting of Si and C atoms is formed during epitaxial growth samples before the SLG layer. Therefore, it may behave differently than conventional SLG and could cause a different response, as observed.

7.7 Commercial single-layer graphene on Si wafer

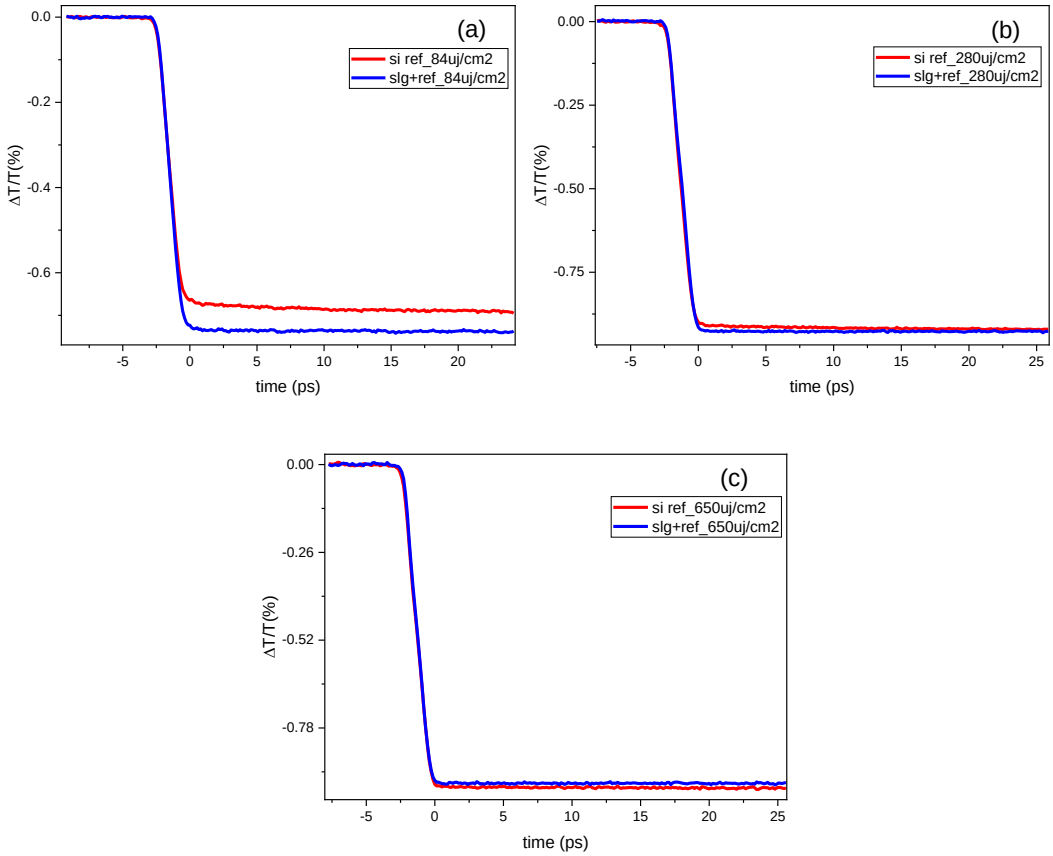

Figure 7.16 Differential THz peak transmission response, $\Delta T/T_0$, of Si/SiO_2 as reference and SLG on Si/SiO_2 as a function of pump–probe delay recorded at pump fluences of a) 84 μj/cm^2, b)300 μj/cm^2, and c) 700 μj/cm^2.

The THz response of the sample upon optical gating is given in Figure 7.16 (a), (b), and (c) with respect to fluences of a)84 μj/cm^2, b)300 μj/cm^2, and c) 700 μj/cm^2. As the optical pulse excites the sample, there was a comparably sharp and intense decrease in the THz peak amplitude for the reference and the sample owing to the effective response of the semiconducting Si substrate. The sample's response slightly

differed as it had a less strong response than the substrate. As the fluence increased, the sample tended to respond stronger up to the point that its response exceeded that of the reference, Si/SiO_2.

The reference-subtracted sole SLG responses for the commercial sample are presented in Figure 7.17. As the figure suggests, for low fluences, it was pretty hard to isolate sample response only, whereas increasing the fluence up to 300µj/cm^2 and more caused to obtain discernible sample response in which there can still be track of reference response.

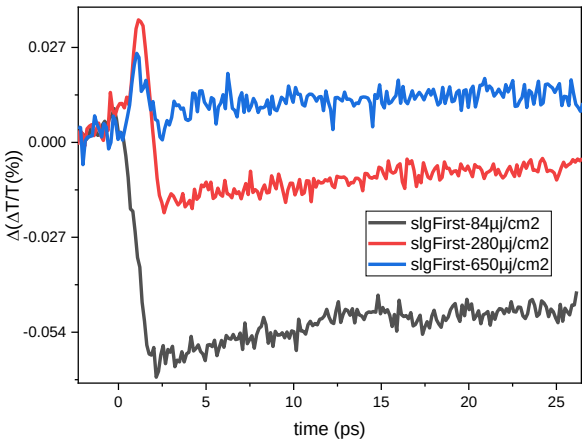

Figure 7.17. The difference in differential THz peak transmission response of the data is given in Figure 7.16. Si/SiO_2 substrate response was considered as a reference.

7.8 Multi-layer graphene, MLG850, on quartz

Figure 7.18 shows the fitted differential THz transmission, $\Delta T/T_0$, of MLG850 as a function of pump–probe delay recorded at a fluence of 700µJ/cm^2. The inset of the graph represents a long scan over 450 ps. The initial sharp response had a rise time

of 2.54ps and decaying over τ_1=6.69±0.08ps. The free carriers seem to live longer than our measuring limits.

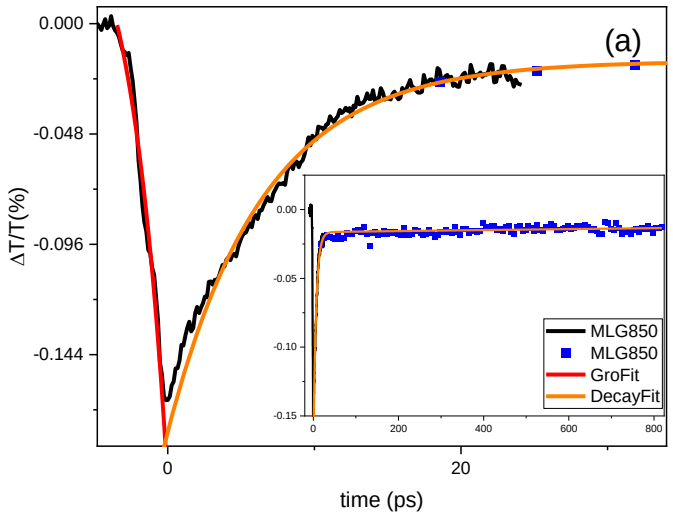

Figure 7.18 (a) Fitted differential THz transmission, $\Delta T/T_0$, of MLG850 as a function of pump–probe delay recorded at a fluence of 700 μJ/cm^2. (b) In log scale, fitted differential THz transmission, $\Delta T/T_0$, of MLG850 as a function of pump–probe delay recorded at a fluence of 700 μJ/cm^2 for a clearer representation of decay

7.9 Multi-layer graphene, MLG900, on quartz

The MLG900 sample's differential THz responses after being excited optically are given in Figure 7.19. The 400 nm excitation had a rise time of 1.16ps and triexponential decay having lifetimes of τ_1=4.89±0.07ps, τ_2=0.24±0.03ps, and τ_3=247.3±19.3ps. The free carriers still existed throughout the measurement, living longer than 450ps. On the other hand, the 800nm excitation had a rise time of 0.88ps and tri-exponential decay with lifetimes of τ_1=5.43±0.05ps and τ_2=0.44±0.06ps and τ_3=8064.2±2324.3ps. The free carriers also have long lifetimes exceeding 450ps.

Compared to the results, the 800nm excitation resulted in more carrier density, causing less momentum and scattering among the carriers, resulting in longer carrier lives.

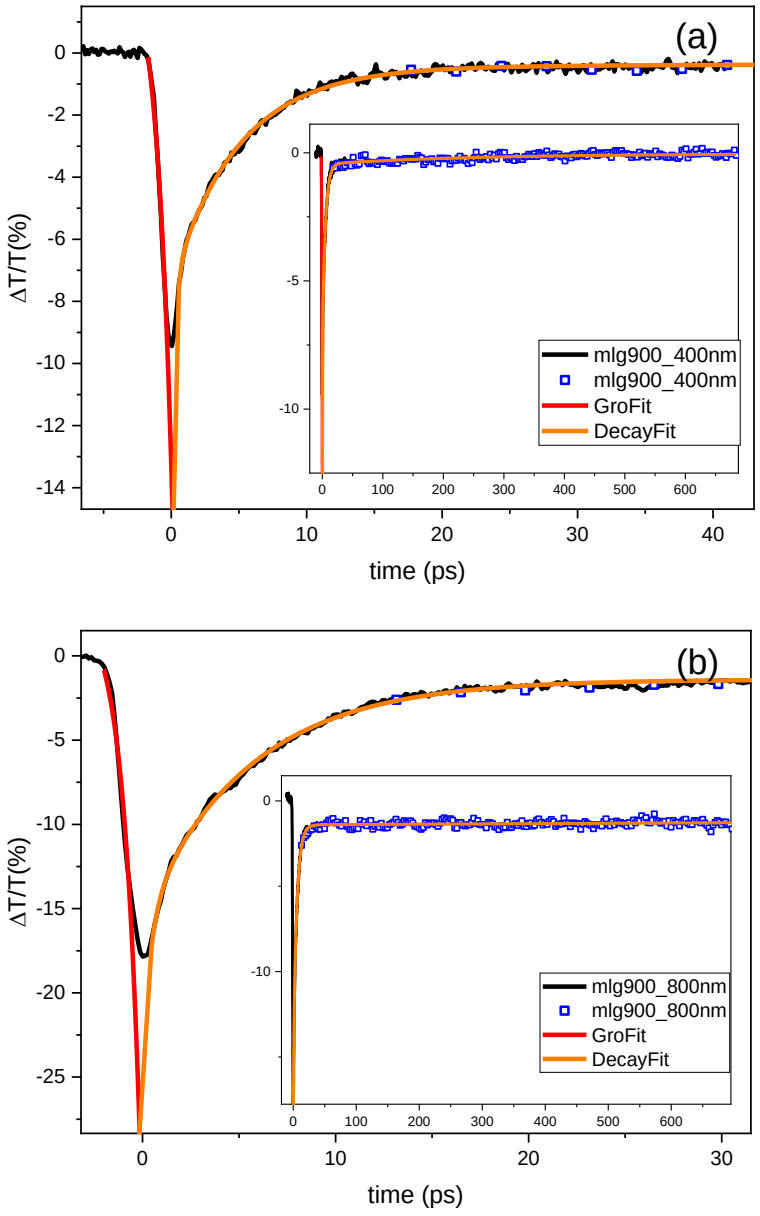

Figure 7.19 (a) Fitted Differential THz transmission, $\Delta T/T_0$, of MLG900 as a function of pump–probe delay recorded at a fluence of 230 $\mu J/cm^2$ for 400nm

excitation and (b) Fitted a fluence of 700 μJ/cm^2 for 800nm excitation. Insets show the long scans covering a 450 ps time scale and enable the observation of lived carrier dynamics.

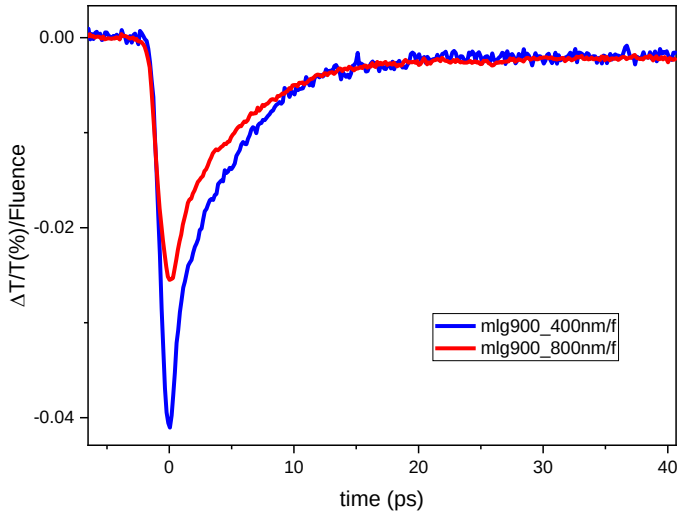

Figure 7.20. Compared differential THz signal of MLG900 for 400nm and 800nm, corrected by fluence applied

Figure 7.20 represents a comparison of THz response change upon 400nm and 800nm excitation when corrected by the applied fluence. As the figure suggests, the initial fast rise after optical excitation was almost the same for both colors, differing in their magnitude. 400nm excitation has higher energy than 800nm, leading to excitation in higher energy states. The resulting carriers were hotter and, hence, had higher mobility. This leads to a longer mean free path, resulting in less recombination and a higher magnitude initial signal. The initial fast decay resulted from the thermalization of the carriers within a couple of ps. After ca. 10ps, both 400nm and 800nm revealed similar amounts of long-lived free carriers with a similar decay fashion. Therefore, the long-lived free carrier properties for this sample were independent of the wavelength applied.

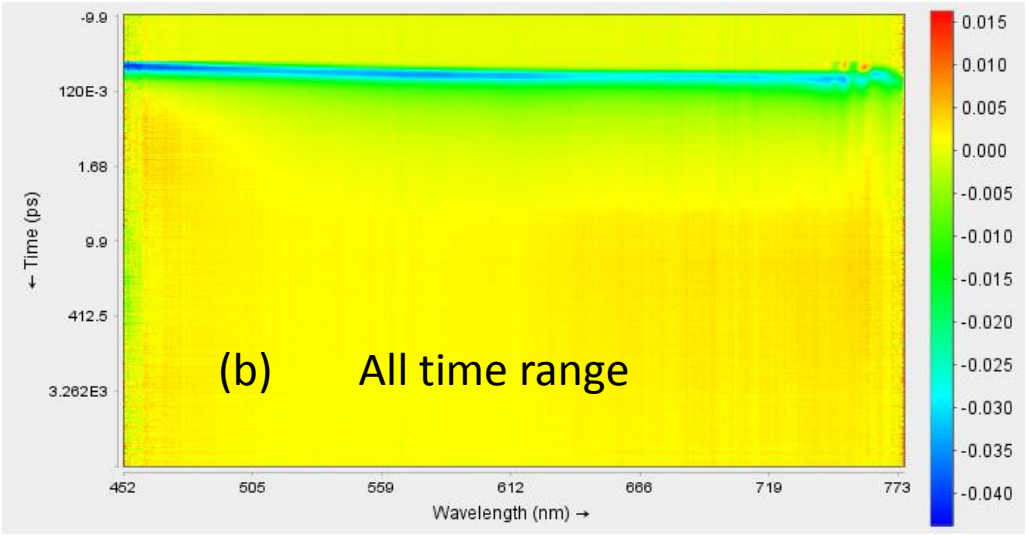

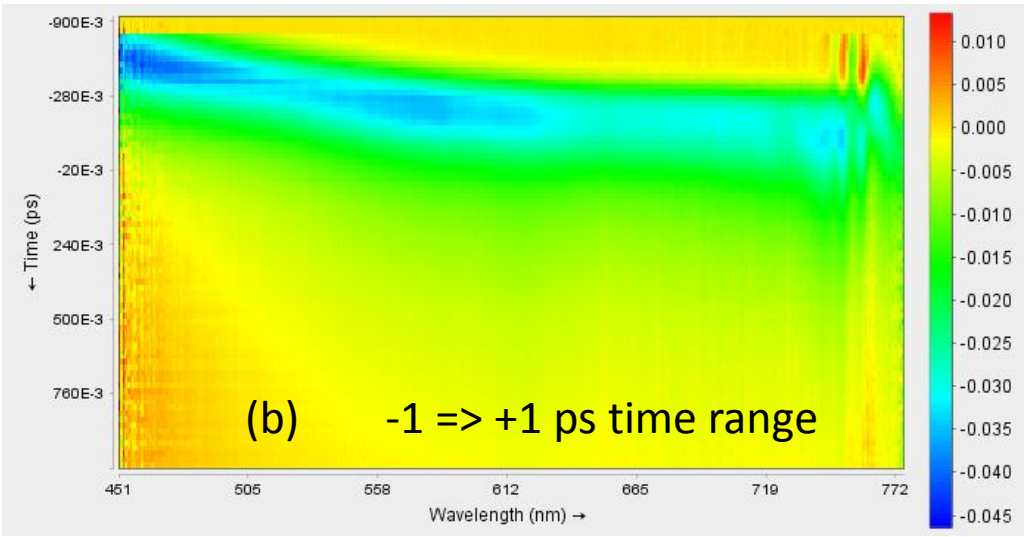

Figure 7.21. (a) and (b) TAS contour plot of 400 nm excited MLG900 sample at visible (white) probe wavelengths in ~7ns and 2 ps timespan respectively

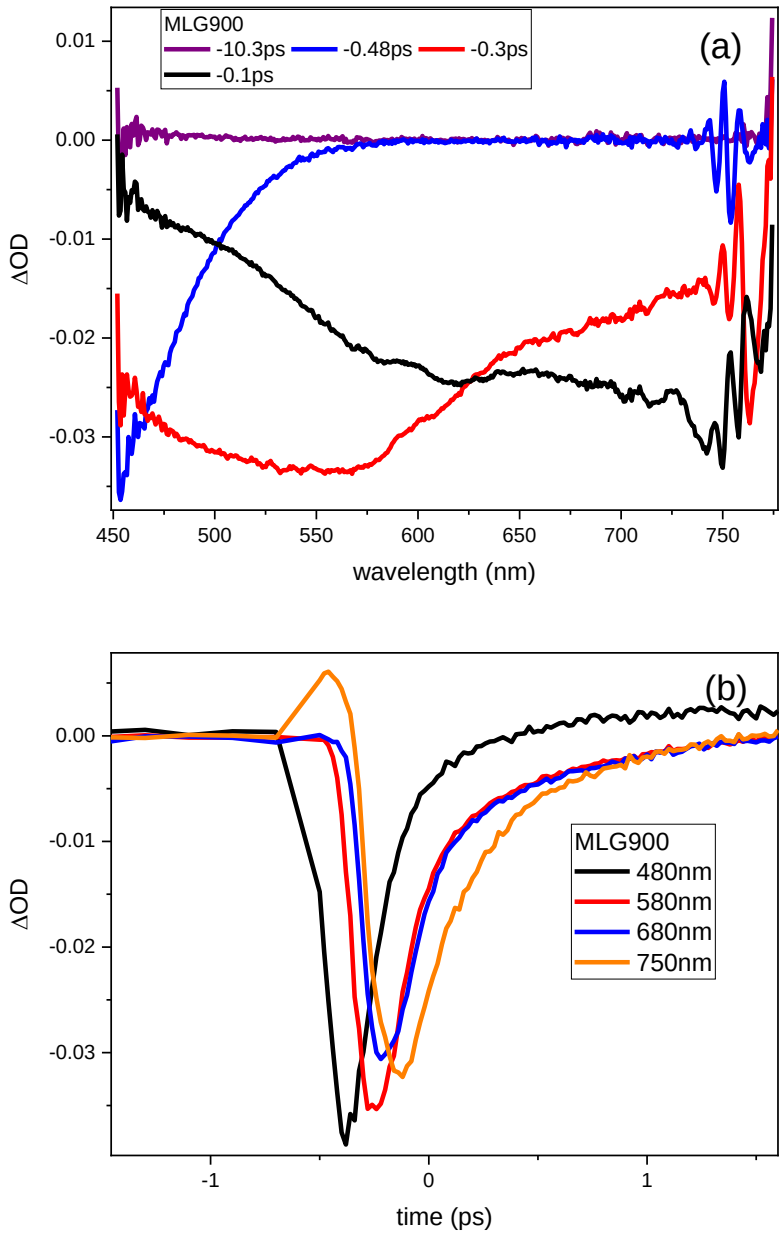

Figure 7.22 (a) Transient spectra in the visible range for different time scales (b) Pump-induced transmission of different photon energies, 480nm, 580nm, 680nm, and 750nm.

Figure 7.21(a) and (b) represent comprehensive TAS data shown as contour plots, Figure 7.22 (a) shows the transient spectra at different time scales, and (b) illustrates the extracted kinetic traces for 480nm, 580nm, 680nm, and 750 nm. In plots of Figure 7.21 (a) and (b), the y-axis shows the time in ps, whereas the x-axis displays the probe wavelengths in the visible range of the EM spectrum. As the figures suggest, the electron (hole) distributions were located at higher (lower) energies [104]; therefore, the bleaching was more dominant at shorter wavelengths. In addition to this, the negative ΔOD values at especially shorter wavelengths around 450nm in Figure 7.22 (a) also imply that the signal bleaching became more dominant for those wavelengths. On the other hand, in Figure 7.22 (b), the probe responses for the given wavelengths were different from each other. For the 480nm probe, the pump response initially caused decreased absorption, followed by a positive ΔOD component. The initial decrease in the ΔOD signal was attributed to the negative component and was most probably caused by intraband absorption due to the bleaching of the transition.[106] Similar initial response is observed for 580 nm, 680 nm, and 750nm transients, all converging to zero basis. However, the 480 nm transient crossed the zero level to generate a positive component that could be explained by intraband absorption in the literature.[106] Also, in another study in the literature, this positive behavior was attributed to thermal diffusion and shrinkage of band separation,[109] though no band separation was expected in graphene.

7.10 Multi-layer graphene, MLG950, on quartz

Figure 7.23 shows the differential THz response of sample 1 for MLG950 after optical excitation. The 400nm excitation had a rise time of 0.50ps and a single exponential decay with a lifetime of τ_1=5.60±0.04. The experiment showed that the free carriers lasted longer than 450ps. The 800nm excitation had a rise time of 1.07ps and a monoexponential decay with a lifetime of τ_1=6.47±0.04. Similarly, the

experiment showed that the free carriers lasted longer than 450ps. However, the 800nm excitation resulted in more carrier density because it caused less momentum and, therefore, less scattering among the carriers, resulting in longer carrier lives.

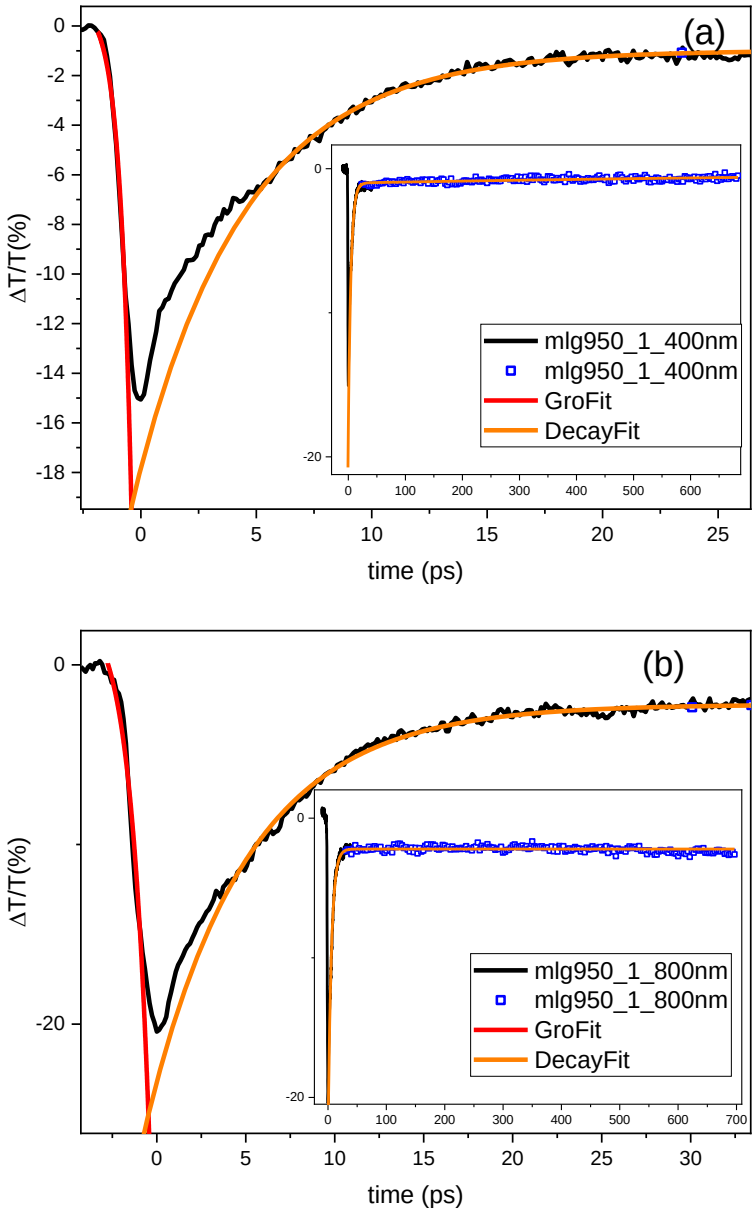

Figure 7.23. Fitted differential THz transmission, $\Delta T/T_0$, of (a) MLG950 Sample 1 as a function of pump–probe delay recorded at a fluence of 230 $\mu J/cm^2$ for 400nm

excitation and b) a fluence of 700 μJ/cm^2 for 800nm excitation. Insets show the long scans covering up to 450 ps time scale and enable the observation of lived carrier dynamics.

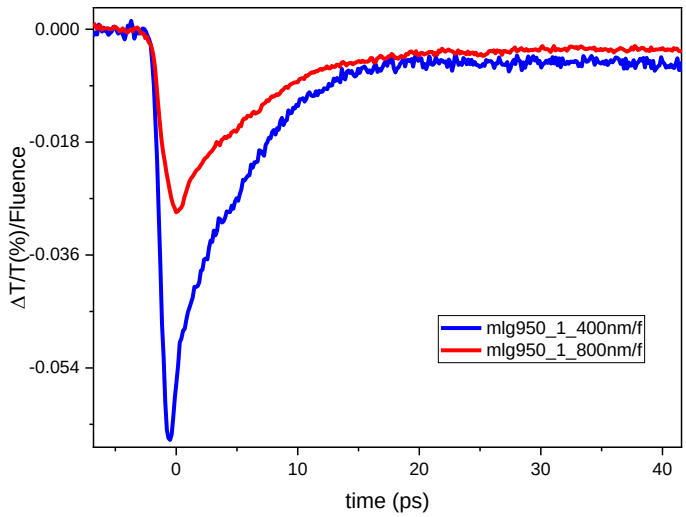

Figure 7.24. Compared differential THz signal of MLG950-1 for 400nm and 800nm, corrected by fluence applied

Figure 7.24 represents a comparison of THz transmission change upon 400nm and 800nm excitation when corrected by the applied fluence. As the figure suggests, the initial fast rise after optical excitation was almost the same for both colors, differing in their magnitude. 400nm excitation has higher energy than 800nm, leading to excitation in higher energy states. The generated carriers were hotter and, therefore, had higher mobilities. This leads to a longer mean-free path, resulting in less recombination and higher magnitude in the signal. The initial fast decay resulted from the thermalization of the carriers within a couple of ps. After 15ps, the available long-lived free carrier number was higher for the 400nm pump because, with higher pump energy, the carriers could hop to other graphene layers more easily, resulting in less recombination and a longer lifetime.

In Figure 7.25, you can see the differential THz response of sample 2 for MLG950 after optical excitation. The 400nm excitation had a rise time of 0.56ps and a triple exponential decay with a lifetime of τ_1=4.28±0.10ps, τ_2=393.2±898.7ps, and τ_3=5.37±ps. The experiment revealed that the free carriers lasted for more than 450ps. On the other hand, the 800nm excitation had a rise time of 1.07ps and a monoexponential decay with a lifetime of τ_1=6.56±0.04. Similarly, the experiment showed that the free carriers lasted more than 450ps. However, the 800nm excitation resulted in a higher carrier density because it caused less momentum and, therefore, less scattering among the carriers, resulting in longer carrier lives.

Both samples showed comparable THz dynamics, having close rise and decay times.

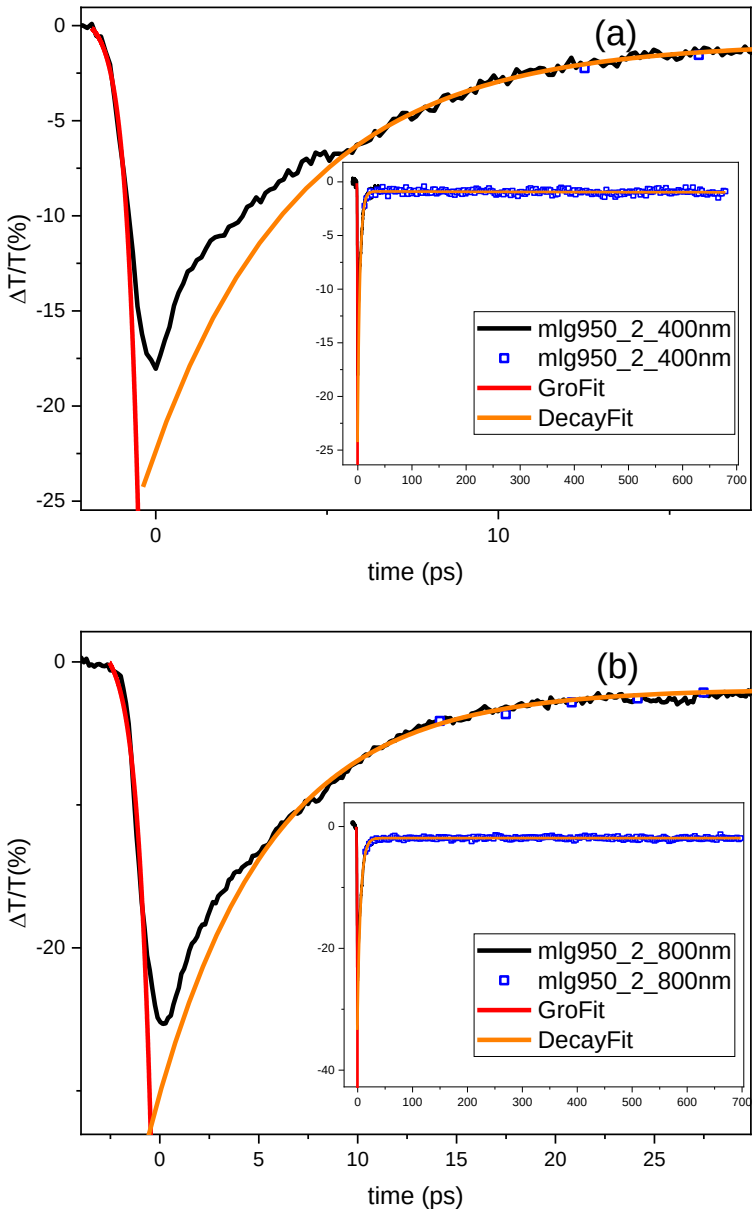

Figure 7.25. Fitted differential THz transmission, $\Delta T/T_0$, of MLG950 Sample 2 as a function of pump–probe delay recorded at a fluence of 230 μJ/cm^2 for 400nm excitation and b) a fluence of 700 μJ/cm^2 for 800nm excitation. Insets show the long scans covering up to 450 ps time scale and enable the observation of long-lived carrier dynamics.

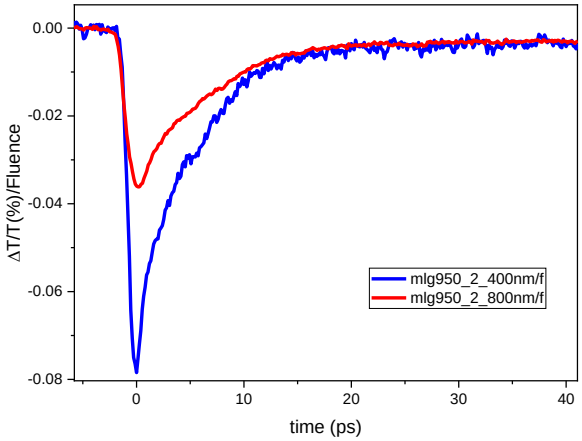

Figure 7.26. Compared differential THz signal of MGL950-2 for 400nm and 800nm, corrected by fluence applied

Figure 7.26 represents a comparison of THz response change upon 400nm and 800nm excitation when corrected by the applied fluence. As the figure suggests, the initial fast rise after optical excitation was almost the same for both colors, differing in their magnitude. 400nm excitation has higher energy than 800nm, leading to excitation in higher energy states. The resulting carriers were hotter and, hence, had higher mobility. This leads to a longer mean free path, resulting in less recombination and a higher magnitude initial signal. The initial fast decay resulted from the thermalization of the carriers within a couple of ps, which is faster for 400nm due to higher energy. After ca. 10ps, both 400nm and 800nm showed similar amounts of long-lived free carriers with similar decay fashions. Therefore, the long-lived free carrier properties were also not significantly different for this sample.

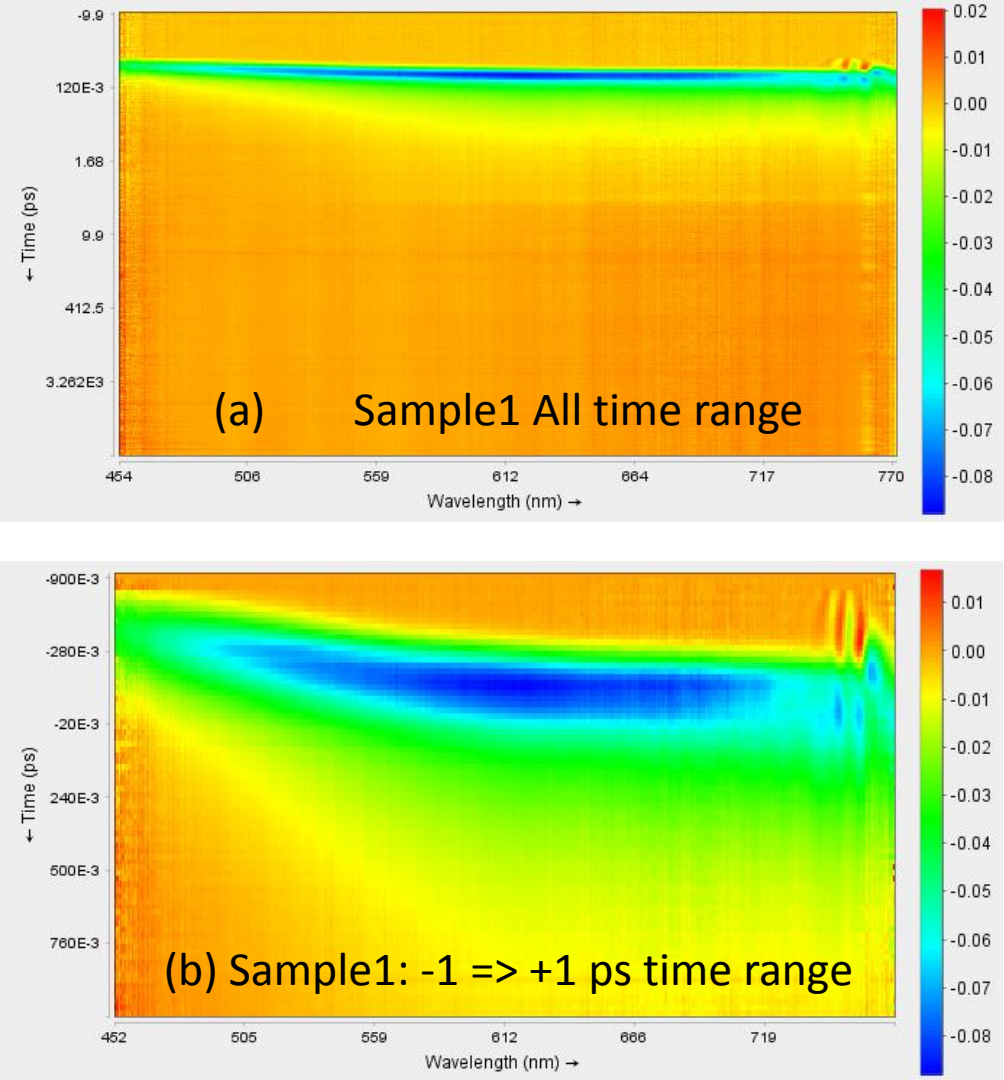

Figure 7.27. (a), (b) TAS contour plot spectrum of 400 nm excited MLG950 sample-1 at visible (white) probe wavelengths in 7ns and 2ps timespan respectively

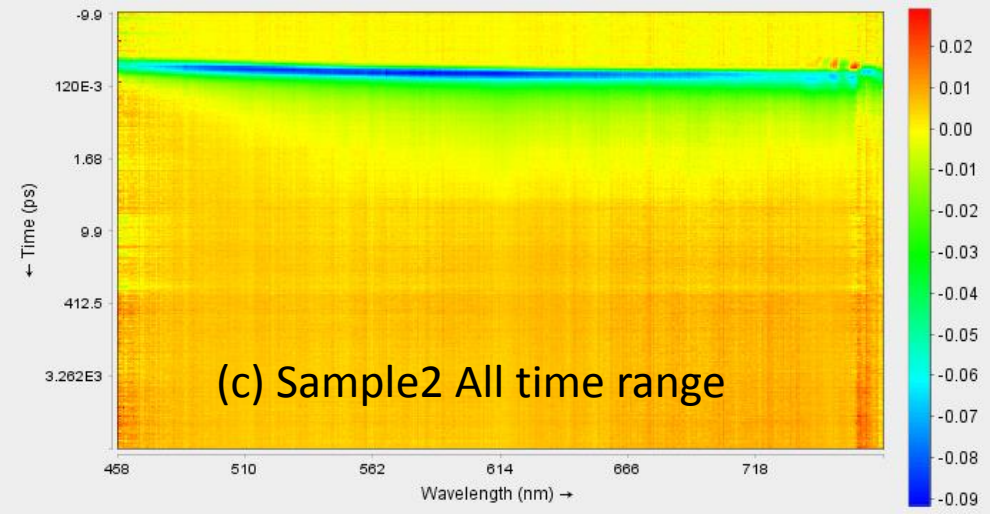

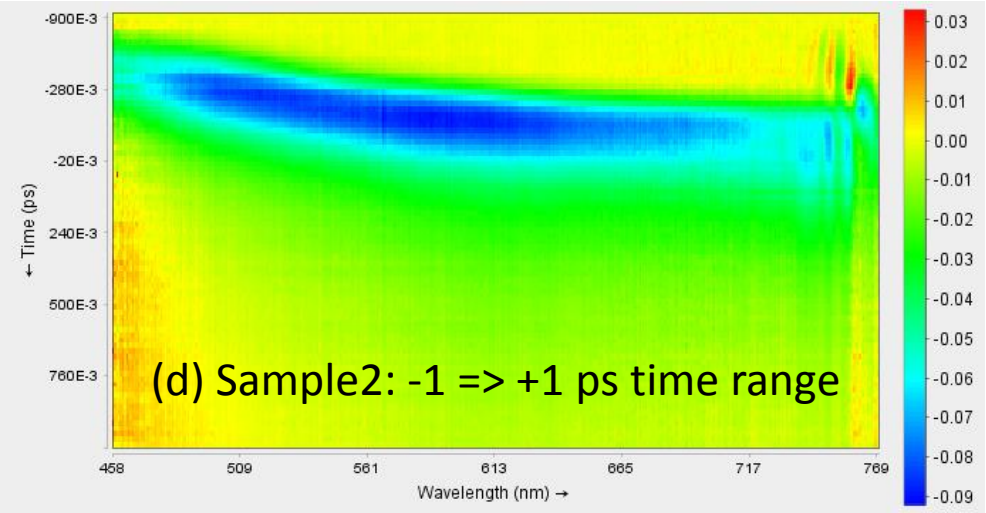

Figure 7.28. (a), (b) TAS contour plot spectrum of 400 nm excited MLG950 sample-2 at visible (white) probe wavelengths in 7ns and 2ps timespan respectively

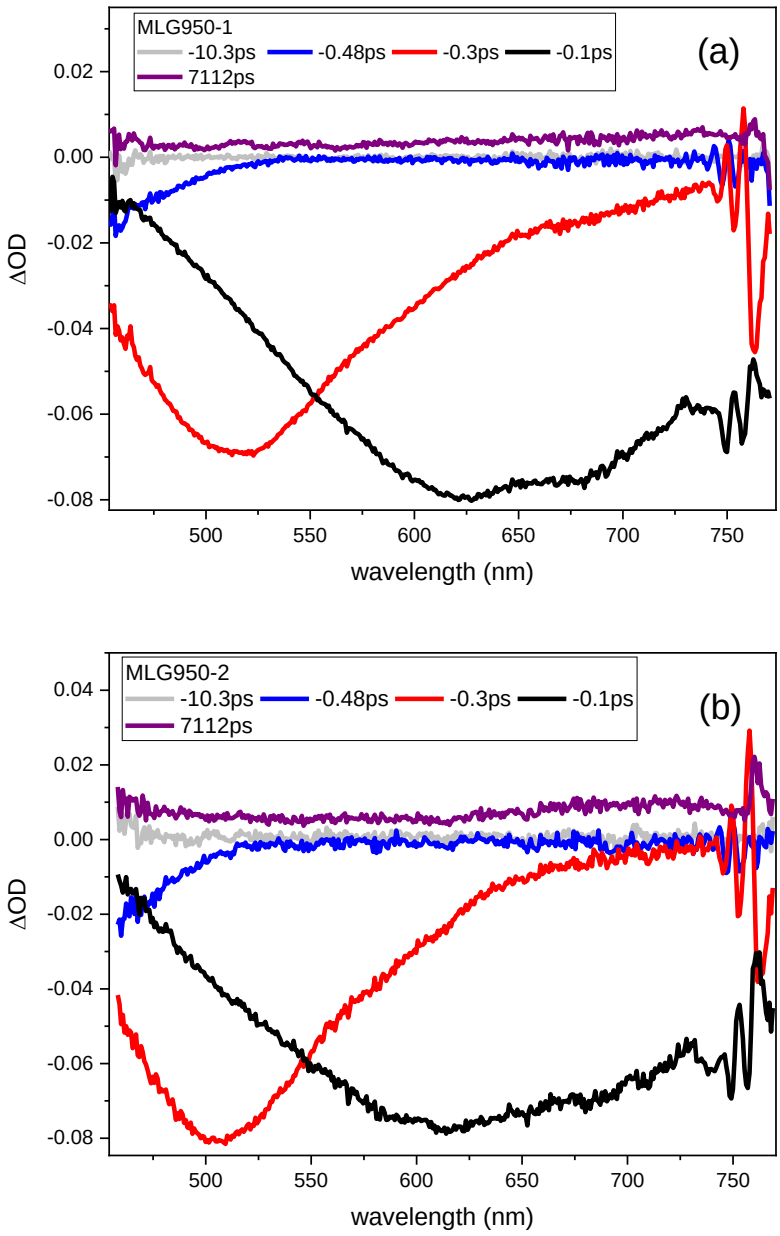

Figure 7.29. (a), (b) Transient spectra in the visible range at different time scales for MLG950 of sample-1 and 2 respectively

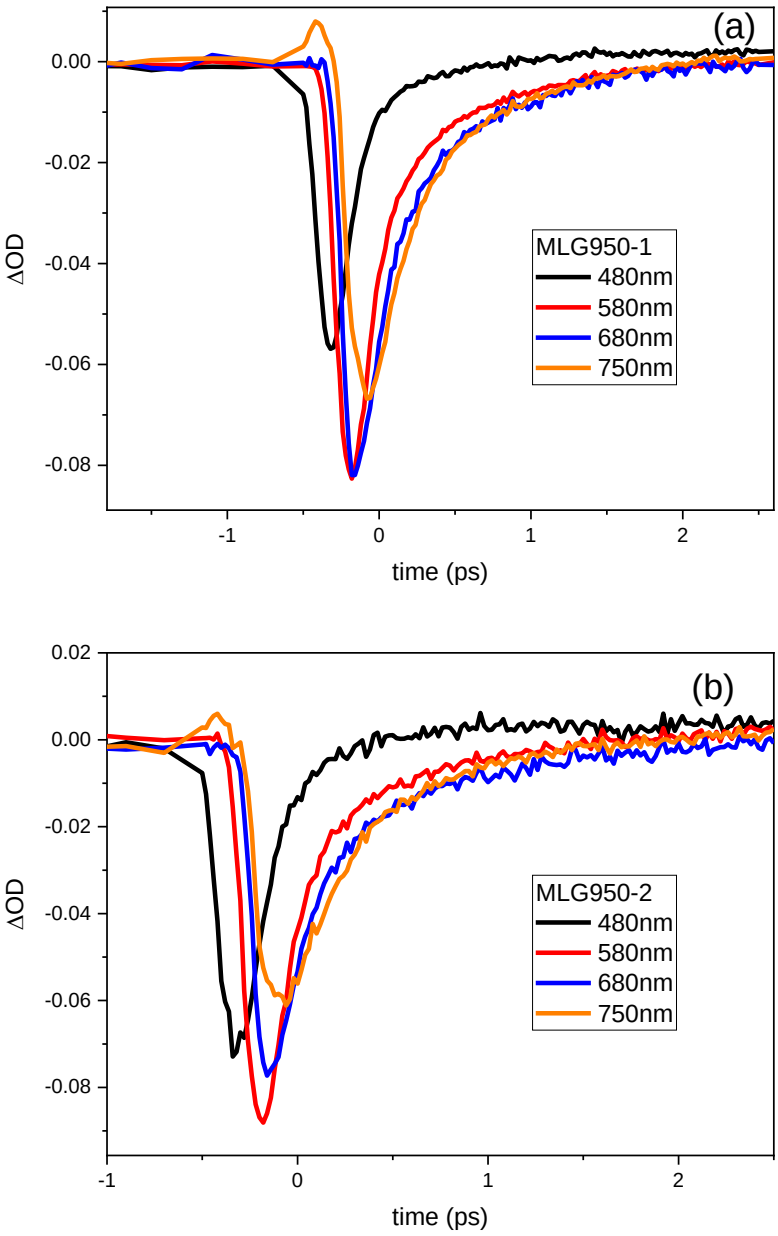

Figure 7.30. (a), (b) Pump-induced transmission of different photon energies, 480nm, 580nm, 680nm, and 750nm for MLG950 of sample-1 and 2

Figure 7.27 (a), (b) and Figure 7.28 (a), (b) represent comprehensive TAS data shown as contour plots, Figure 7.29 (a) and (b) shows the transient spectra at different time scales, and Figure 7.30 (a), (b) illustrates the extracted kinetic traces for 480nm, 580nm, 680nm, and 750 nm. Figure 7.27 (a), (b), and Figure 7.28 (a), (b), the y-axis shows the time in ps, whereas the x-axis displays the probe wavelengths in the visible range of the EM spectrum. As the figures suggest, the electron (hole) distributions were located at higher (lower) energies [104]; therefore, the bleaching was more dominant at shorter wavelengths. In addition to this, the negative ΔOD values at especially shorter wavelengths around 500nm in Figure 7.29 (a) and (b) also imply that the signal bleaching became more dominant for those wavelengths for both samples. On the other hand, in Figure 7.30 (a), (b), the probe responses for the given wavelengths were quite similar for both samples. For the 480nm, 580, and 680nm probes, the pump response initially caused decreased absorption, attributed to the intraband absorption due to the bleaching of the transition. [106] However, for the 750nm probe, a negative signal followed a slight initial positive signal. The positive signal could be attributed to oxygen incorporation into the graphene structure, possibly due to the pump-induced bleaching of the transition.[106]

Similar initial response was observed for 580 nm, 680 nm, and 750nm transients, all converging to zero basis. However, the 480 nm transient crossed the zero level to generate a positive component that could be explained by intraband absorption in the literature.[106] Also, in another study in the literature, this positive behavior was attributed to thermal diffusion and shrinkage of band separation.[109]

7.11 Multi-layer graphene, MLG1000, on quartz

Figure 7.31 presents the differential THz response of sample 1 for MLG1000 after optical excitation. The 400nm excitation had a rise time of 0.77ps and a single

exponential decay with a lifetime of τ_1=5.16±0.09ps. The experiment demonstrated that the free carriers lasted for more than 450ps. The 800nm excitation had a rise time of 2.49ps and a monoexponential decay with a lifetime of τ_1=5.29±0.07ps. Similarly, the experiment revealed that the free carriers lasted more than 450ps. However, the 800nm excitation resulted in a higher carrier density than the 400nm excitation. This was because it caused less momentum and, therefore, less scattering among the carriers, resulting in longer carrier lives.

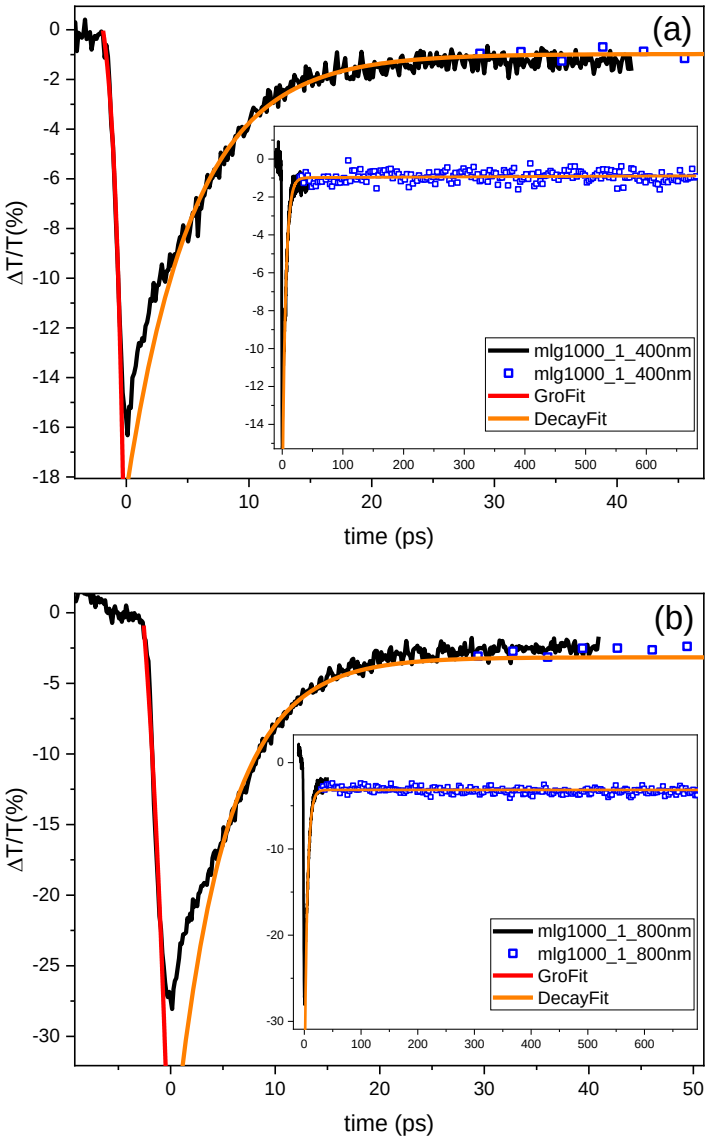

Figure 7.31. Fitted differential THz transmission, $\Delta T/T_0$, of MLG950 Sample 1 as a function of pump–probe delay recorded at a fluence of 230 μJ/cm^2 for 400nm excitation and b) a fluence of 700 μJ/cm^2 for 800nm excitation. Insets show the long scans covering up to 450 ps time scale and enable the observation of long-lived carrier dynamics.

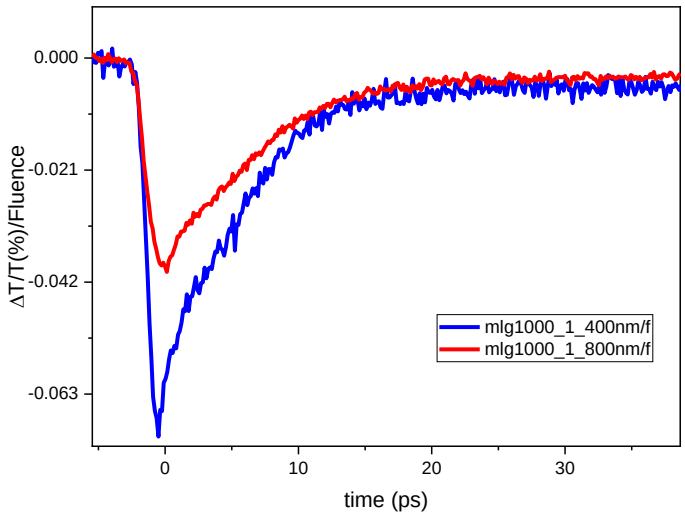

Figure 7.32. Compared differential THz signal of MLG1000-1 for 400nm and 800nm, corrected by fluence applied

Figure 7.32 represents a comparison of THz response change upon 400nm and 800nm excitation when corrected by the applied fluence. As the figure suggests, the initial fast rise after optical excitation was almost the same for both colors, differing in their intensity. 400nm excitation has higher energy than 800nm, leading to excitation in higher energy states. The resulting carriers were hotter and, hence, had higher mobility. This leads to a longer mean free path, resulting in less recombination and a higher magnitude initial signal. The initial fast decay resulted from the thermalization of the carriers within a couple of ps, which is faster for 400nm due to higher energy. After ca. 15 ps, the available free carrier number was slightly more for 400nm excitation, indicating higher pump energy that caused carriers to hop to other graphene layers more easily, resulting in less recombination.

In Figure 7.33, we can observe the differential THz response of sample 2 for MLG1000 after optical excitation. The 400nm excitation had a rise time of 0.61ps and a single exponential decay with a lifetime of τ_1=7.05±0.07ps. The experiment

demonstrated that the free carriers lasted for over 450ps. The 800nm excitation had a rise time of 1.52ps and a monoexponential decay with a lifetime of τ_1=5.79±0.08ps. Similarly, the experiment revealed that the free carriers lasted more than 450ps. However, the 800nm excitation resulted in a higher carrier density than the 400nm excitation. This was because it caused less momentum and, therefore, less scattering among the carriers, resulting in longer carrier lives.

Samples 1 and 2 showed apparent differences in their rise and decay times for their THz responses, with sample 2's slower dynamics.

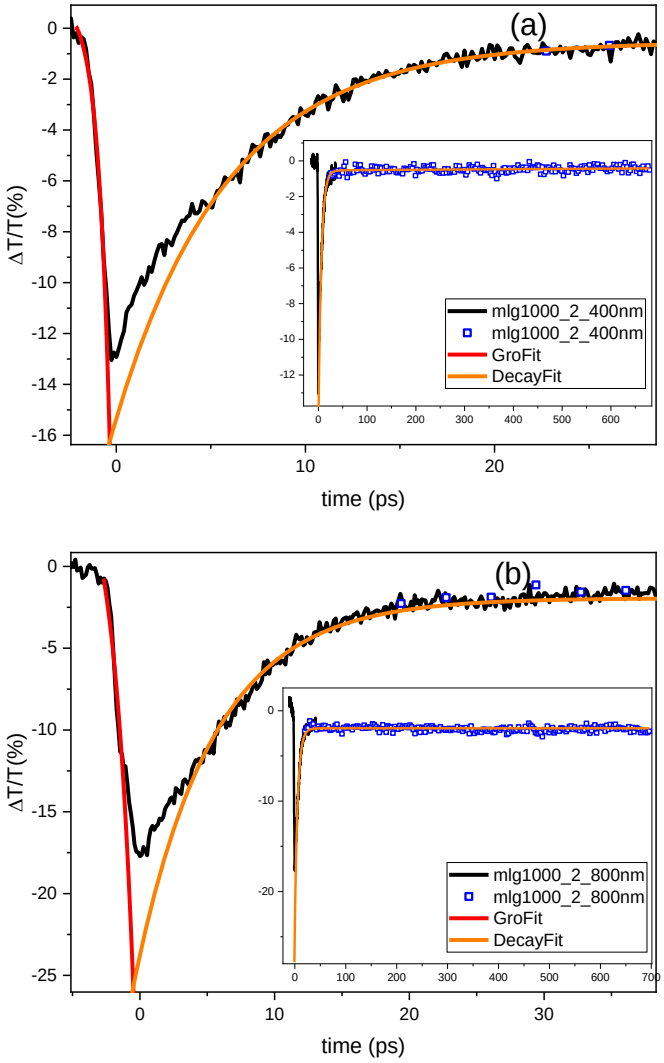

Figure 7.33. Fitted differential THz transmission, $\Delta T/T_0$, of MLG950 Sample 2 as a function of pump–probe delay recorded at a fluence of 230 μJ/cm^2 for 400nm excitation and b) a fluence of 700 μJ/cm^2 for 800nm excitation. Insets show the long scans covering up to 450 ps time scale and enable the observation of long-lived carrier dynamics.

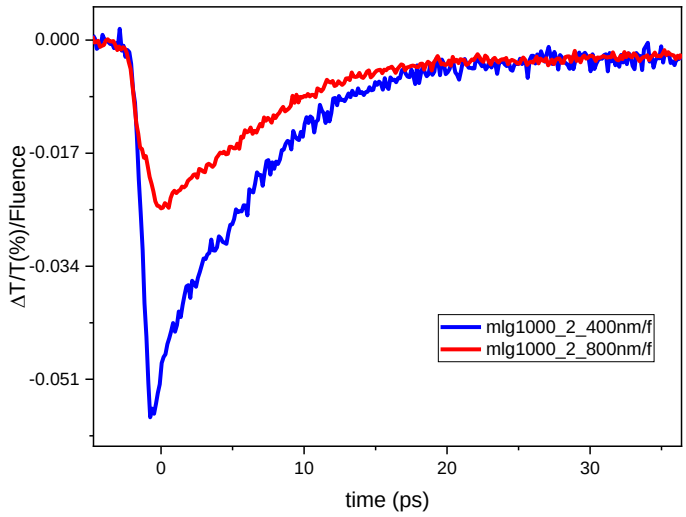

Figure 7.34. Compared differential THz signal of MLG1000-2 for 400nm and 800nm, corrected by fluence applied.

Figure 7.34 represents a comparison of THz response change upon 400nm and 800nm excitation when corrected by the applied fluence. As the figure suggests, the initial fast rise after optical excitation was almost the same for both colors, differing in intensity. 400nm excitation has higher energy than 800nm, leading to excitation in higher energy states. The generated carriers were hotter and, therefore, had higher mobility. This leads to a longer mean-free path, resulting in less recombination and higher magnitude in the signal. The initial decay resulted from the thermalization of the carriers within a couple of ps, which is faster for 400nm due to higher energy. After ca. 20ps, the available free carrier number became almost the same, indicating that pump color did not affect the amount of long-lived free carriers for this sample.

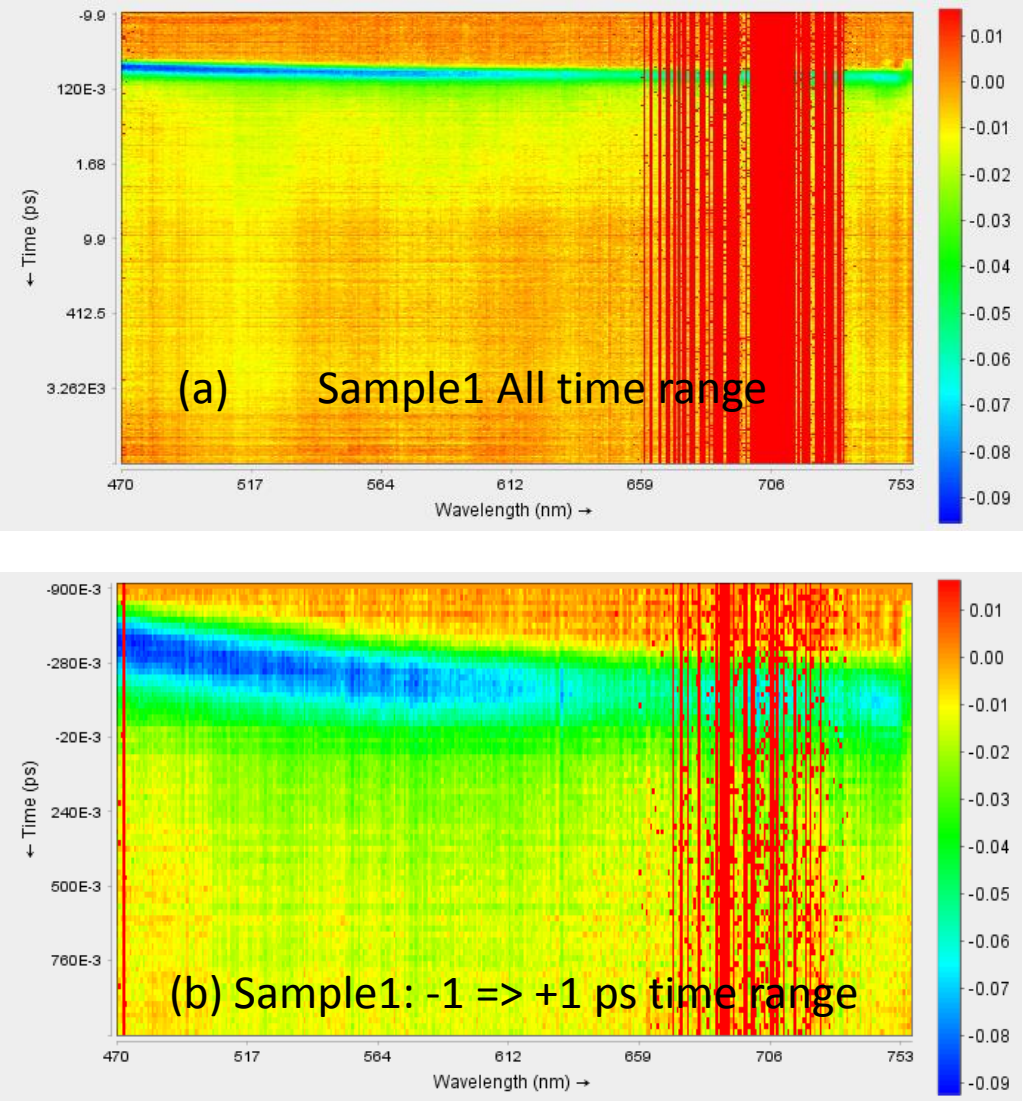

Figure 7.35. (a), (b) TAS contour plot spectrum of 400 nm excited MLG1000 sample-1 at visible (white) probe wavelengths in 7ns and 2ps timespan respectively

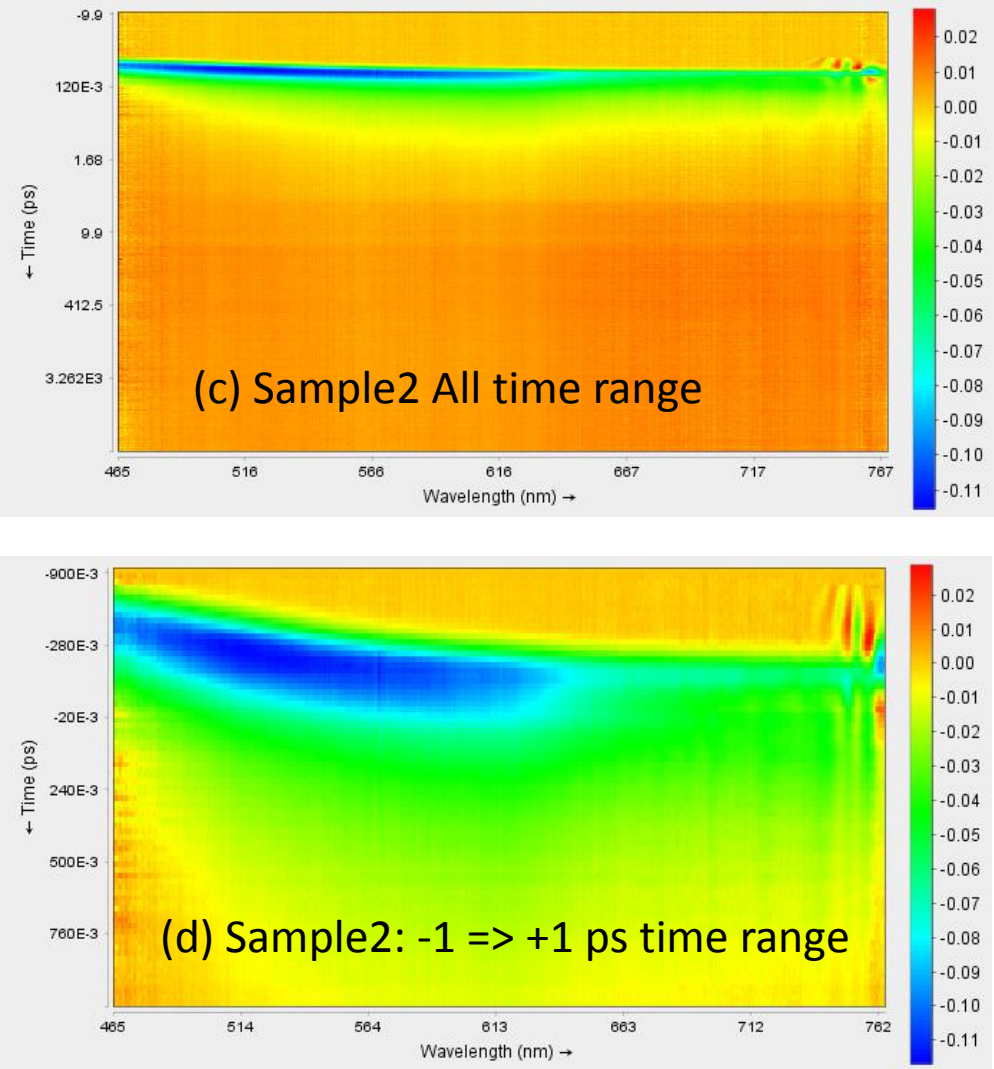

Figure 7.36. (a), (b) TAS contour plot spectrum of 400 nm excited MLG1000 sample-2 at visible (white) probe wavelengths in 7ns and 2ps timespan respectively

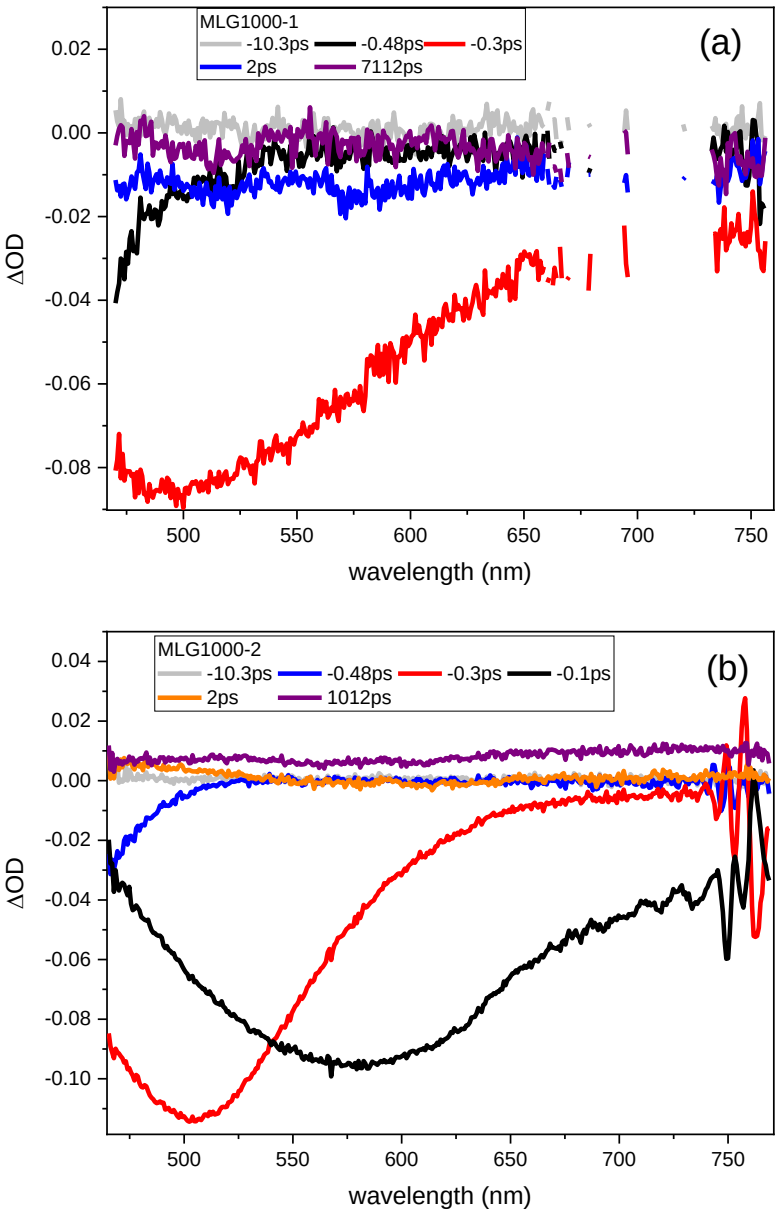

Figure 7.37. (a), (b) Transient spectra in the visible range at different time scales for MLG1000 of sample-1 and 2 respectively

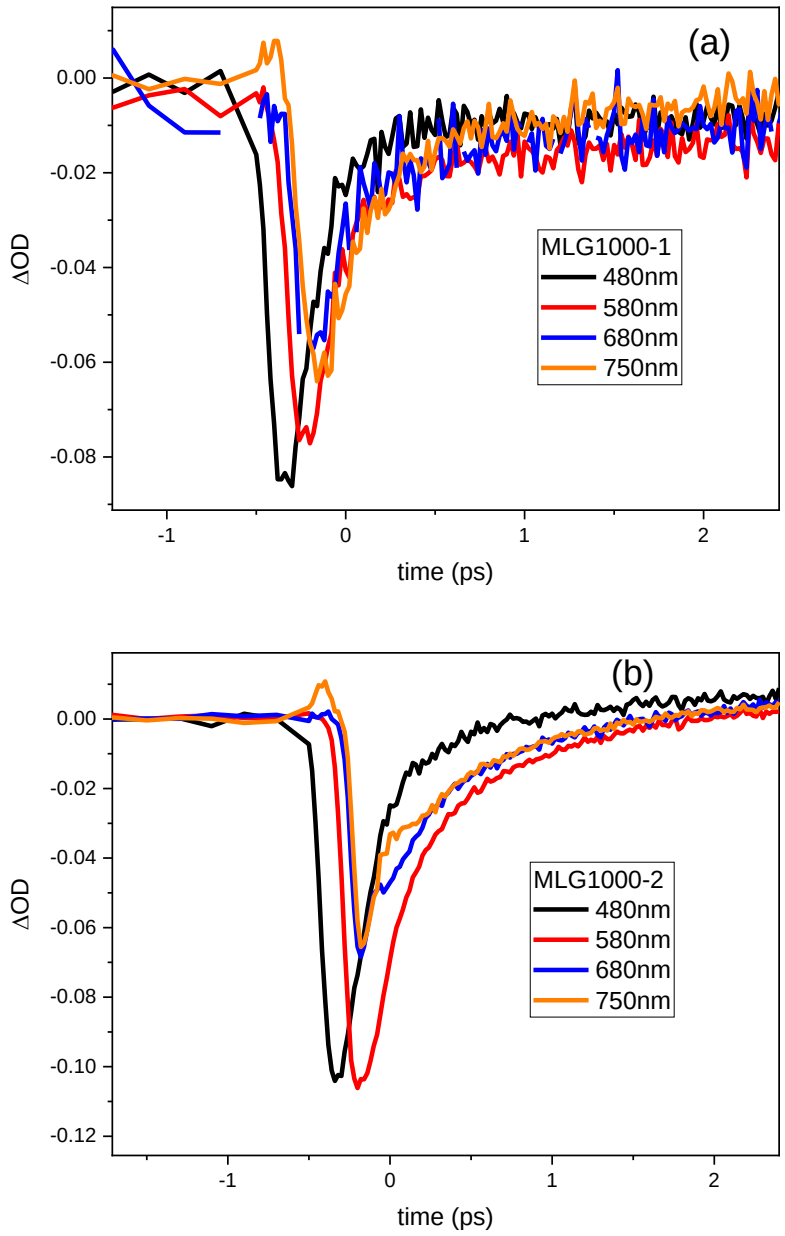

Figure 7.38. (a), (b) Pump-induced transmission of different photon energies, 480nm, 580nm, 680nm, and 750nm for MLG1000 of sample-1 and 2

Figure 7.35 (a), (b) and Figure 7.36 (a), (b) represent comprehensive TAS data shown as contour plots, Figure 7.37 (a), (b) show the transient spectra at different time scales, and Figure 7.38 (a), (b) illustrates the extracted kinetic traces for 480nm, 580nm, 680nm, and 750 nm. In plots of Figure 7.35 (a) and (b), and Figure 7.36 (a), (b) the y-axis shows the time in ps, whereas the x-axis displays the probe wavelengths in the visible range of the EM spectrum. As the figures suggest, the electron (hole) distributions were located at higher (lower) energies [104]; therefore, the bleaching was more dominant at shorter wavelengths. In addition to this, the negative ΔOD values at especially shorter wavelengths around 500nm. Figure 7.37 (a) and (b) also imply that the signal bleaching became more dominant for those wavelengths for both samples. On the other hand, in Figure 7.38 (a) and (b), the probe responses for the given wavelengths were quite similar for both samples. For the 480nm, 580, and 680nm probes, the pump response initially caused decreased absorption, which was attributed to the intraband absorption due to the bleaching of the transition. [106] However, for the 750nm probe, a negative signal followed a slight initial positive signal. The positive signal could be attributed to oxygen incorporation into the graphene structure, possibly due to the pump-induced bleaching of the transition.[106]

7.12 Multi-layer graphene on polyvinyl chloride

Figure 7.39 shows the differential THz responses of the MLG on PVC after being optically stimulated. The 800nm excitation has a rise time of 1.71ps and a triexponential decay with lifetimes of τ_1= 0.43±0.15ps; τ_2=3.32±0.06ps; τ_3=117.9±12.9 ps. The free carriers have lifetimes exceeding 450ps.

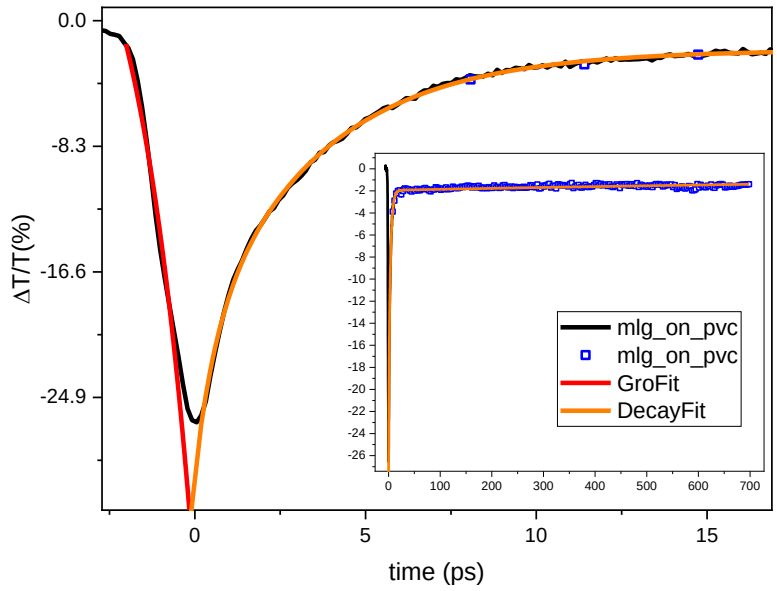

Figure 7.39. Fitted differential THz transmission, $\Delta T/T_0$, of MLG on PVC as a function of pump–probe delay recorded at a fluence of 700 $\mu J/cm^2$ at 800nm.

The graph in Figure 7.40 displays the differential THz responses of MLG on PE after optical stimulation. The 800nm excitation has a rise time of 1.21 ps and a single exponential decay with two lifetimes of τ_1= 5.04±0.03ps. The free carriers have lifetimes exceeding 450ps.

Even though they have similar graphene layers, 30 and 32 layers, their responses are quietly different. The rise and decay dynamics of MGL on PVC seem higher due to the structural differences of both substrates, probably resulting in more carrier traps.

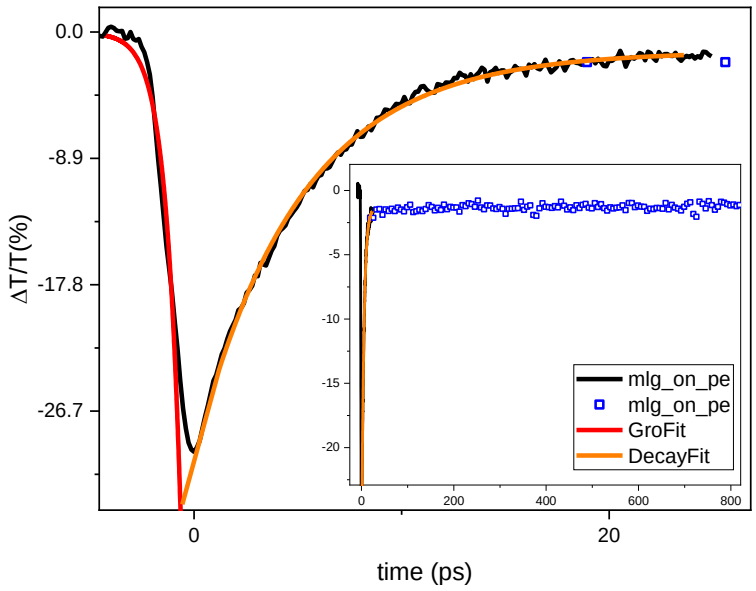

Figure 7.40. Fitted differential THz transmission, $\Delta T/T_0$, of MLG on PE as a function of pump-probe delay recorded at a fluence of 700 $\mu J/cm^2$ at 800nm

7.1 Summary of Comparison of Graphene Decay Dynamics for 400nm Photoexcitation

Table 8. Rise and decay times of multilayer graphene samples for 400nm photoexcitation

		400nm pump	
	2D material	**Rise (ps)**	**Decay (ps)**
Multi-layer graphene	MLG900	1.2±0.18	0.24±0.07 4.9±0.06 247.2±19.38
	MLG950-1	0.50±0.03	4.71±1004 1246±112
	MLG950-2	0.37±0.04	4.3±0.10 393.3±897.7
	MLG1000-1	0.77±0.12	5.42±196 5304±4386
	MLG1000-2	0.61±0.07	2251±943 5.92±3243

7.2 Summary of Comparison of Graphene Decay Dynamics for 800nm Photoexcitation

Table 9. Rise and decay times of single and multilayer graphene samples for 800nm photoexcitation

		800nm pump	
	Graphene&Substrate	**Rise (ps)**	**Decay (ps)**
Single layer graphene	SLG on PDMS	1.9±0.23	3.8±0.04
	SLG on PET	1.7±0.24	3.6±0.02
	SLG on PMMA+PDMS-1	1.2±0.12	2.9±0.04
	SLG on PMMA+PDMS-2	1.6±0.17	3.4±0.04
Multi-layer graphene	MLG850	2.5±0.71	6.48±3171 4131±1378
	MLG900	0.88±0.15	0.44±0.06 5.4±0.05 8064±2324
	MLG950-1	1.1±0.20	5.65±2866 7.06
	MLG950-2	1.07	5.78±1885 $3.18x10^{123}$

	MLG1000-1	2.5±0.91	4.93±2446 4.93±3452 1.08^{101}
	MLG1000-2	1.5±0.62	5.78±4580 9.86^{126}±0
	MLG on PVC	1.7±0.51	1986.8±99.84 0.61±0.04 3.48±0.04
	MLG on PE	0.71±0.04	5.02±2532 5.02±2934 7884±5197

7.15 2D TMDC films on Mica substrate

7.15.1 1-Layer of $MoSe_2$ + 2-Layers of $PtSe_2$ on mica

The THz dynamics of 1-Layer of $MoSe_2$ + 2-Layers of $PtSe_2$ on mica (code name of 2705) is presented in Figure 7.41. The sample was stimulated by ultrafast pulses of 400nm and 800nm wavelengths, with 195 μJ/cm^2 and 225 μJ/cm^2 fluences, respectively, and then analyzed using a THz beam. The collected data suggests that the noise level was similar to the sample response, even though multiple measurements were taken to minimize noise interference. Therefore, smoothing of

the signal was required. The dots in the figure represent the collected data, while the line represents the smoothed data using a 20-point average Savitzky-Golay filter.

When the sample was excited with 400 nm light, it exhibited an initial response with a rise time of about 1 ps and a fall time of around 1 ps. However, when excited with 800 nm light, the sample displayed a faster rise time of about 0.35 ps and a similar fall time of about 1 ps. Although both excitations resulted in relatively low THz conductivity, the conductivity was higher for the 800 nm excitation due to the greater density of states available for the $PtSe_2$. [103]

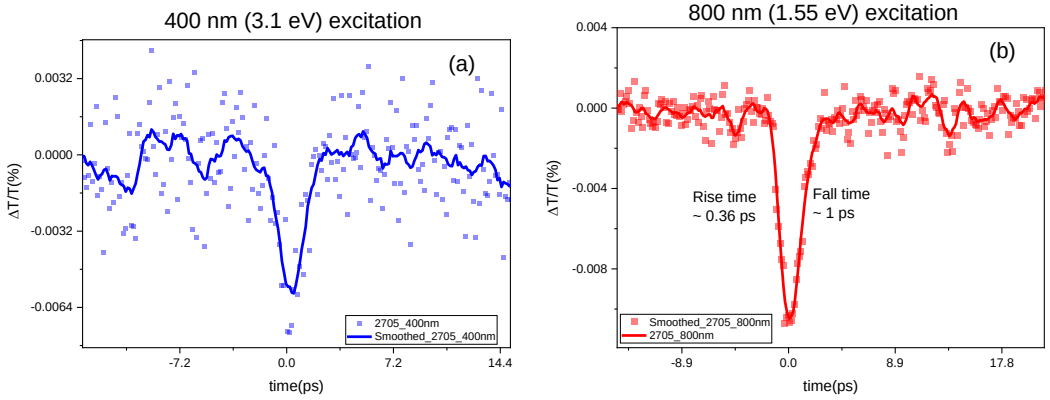

Figure 7.41 Differential THz transmission, $\Delta T/T_0$, of Sample 2705 as a function of pump–probe delay recorded **a)** at a fluence of 195μJ/cm^2 for 400nm excitation and **b)** at a fluence of 255 μJ/cm^2 for 800nm excitation.

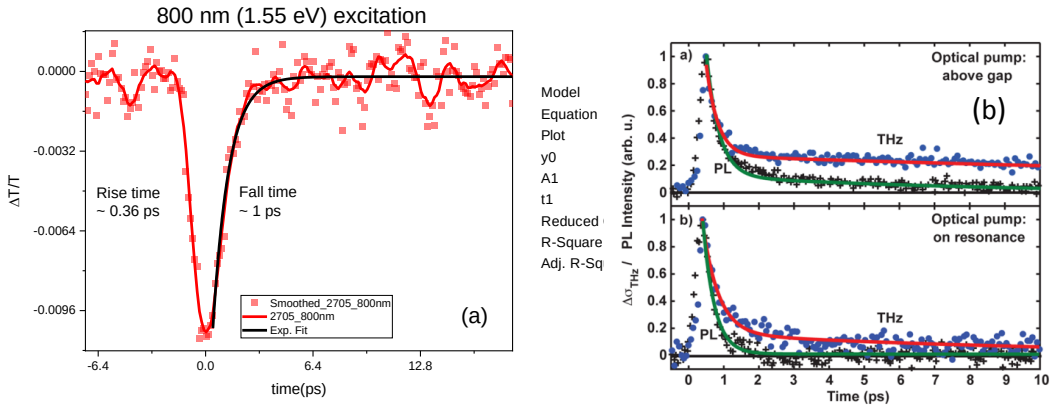

Figure 7.42 (a) Rise and fall time for 800nm (1.54 eV photons with fluence ~1x10^{14} cm^2) excited 2705 sample (b) Literature study showing above bandgap and on resonance THz conductivity of $MoSe_2$ adapted from ref. 110.

Figure 7.42 shows the 800nm excitation response of the $MoSe_2$ sample compared with the literature work.[110] The energy of the pump corresponds to on resonance excitation. Our result matched the literature study well: both shared a sharp initial rise upon photoexcitation and showed decay with a relatively short lifetime.

7.15.2 3-Layers of WSe_2 on mica

The THz dynamics of 3 layers of WSe_2 on mica (code name 2706) are presented in Figure 7.43. The experiment involved exciting a sample with ultrafast pulses of light, having wavelengths of 400 nm and 800 nm and fluences of 195 μJ/cm^2 and 225 μJ/cm^2, respectively. The sample was then probed using a THz beam. However, the signal level obtained was too low compared to the noise response. Multiple measurements consisting of 15 scans were taken to minimize noise interference. The collected data was later smoothed using a 20-point average Savitzky-Golay filter.

When exposed to 400 nm light, the sample's response was characterized by an initial rise time of approximately 0.45 picosecond, followed by a fall time of about 1.1 picoseconds. On the other hand, when exposed to 800 nm light, the sample's response was characterized by a more rapid rise time of around 0.54 picoseconds and a comparable fall time of about 0.72 picosecond. The responses observed were similar to those of Sample 2705 and graphene, although the sample had weaker levels. This could be due to the inability of the sample to generate carriers as much as graphene.

Even though both excitations resulted in relatively low THz conductivity, the conductivity was higher for the 400 nm excitation. This was attributed to the higher density of states in the WSe_2 material. [103]

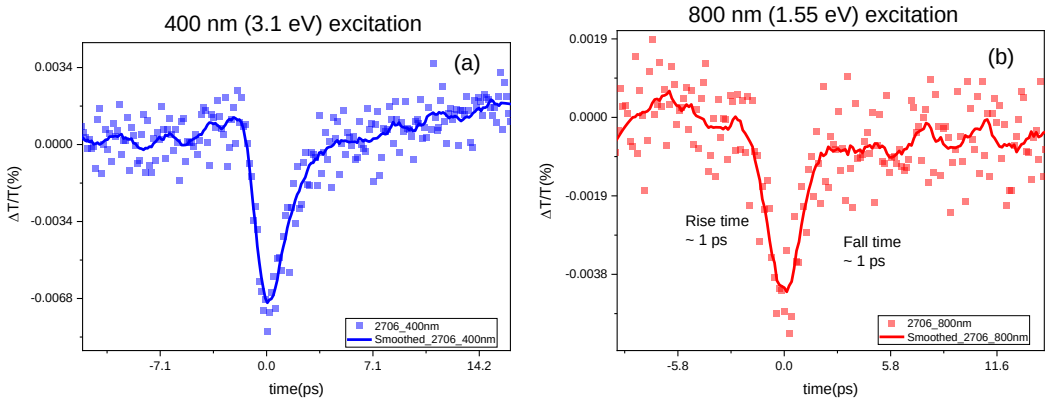

Figure 7.43 Differential THz transmission, $\Delta T/T_0$, of Sample 2706 as a function of pump–probe delay recorded **a)** at a fluence of 195μJ/cm^2 for 400nm excitation and **b)** at a fluence of 255 μJ/cm^2 for 800nm excitation.

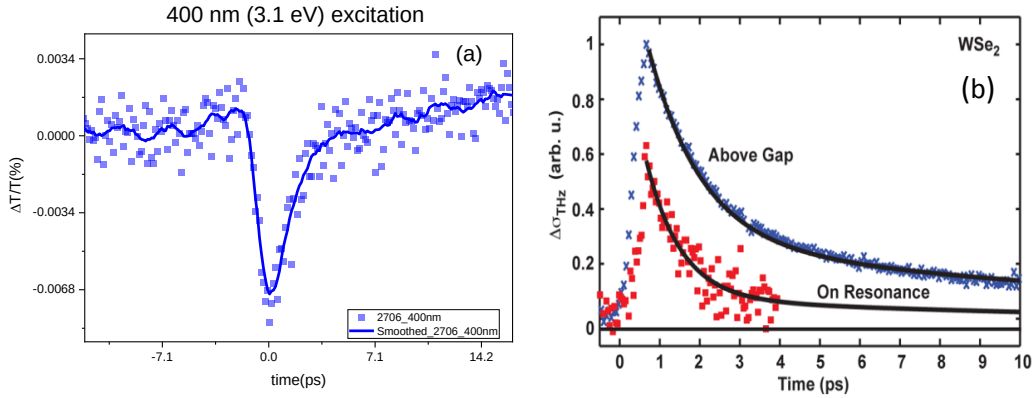

Figure 7.44 (a) Rise and fall time for 400nm (3.1 eV. photons with fluence ~4.x10^{13} /cm^2) excited 2706 sample (b) Literature study showing above bandgap and on resonance THz conductivity of WSe adapted from ref. 110, 111.

Figure 7.44 shows the 400nm excitation response of the WSe_2 sample compared with the literature work.[110] The energy of the pump corresponds to the above bandgap excitation. Our result matched well with the literature study in that both shared a sharp initial rise upon photoexcitation and showed relatively slow decay with a longer lifetime than the $MoSe_2$ sample.

7.15.3 Comparison of TMDC sample responses

Figure 7.45(a) shows the THz response of the 2705 and 2706 samples for 800nm (1.54eV) photoexcitation. The sample 2705 resulted in higher THz conductivity, possibly due to the higher density of states available for this excitation color, as seen in Figure 7.45(b). As the figure suggests, the bandgap of WSe_2 is around 1.7eV, and there is less available density of states, resulting in a lower THz response.

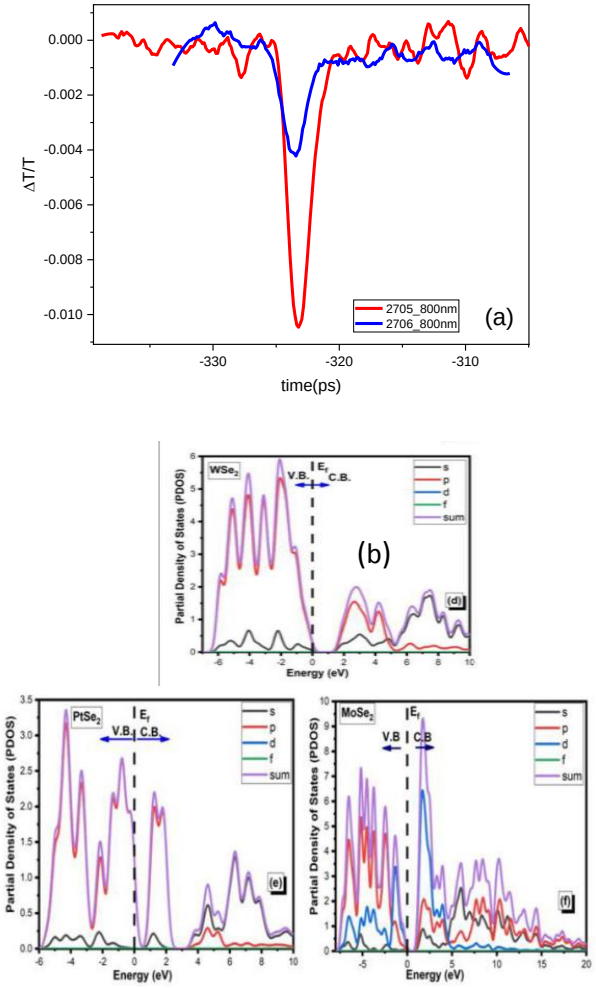

Figure 7.45 (a) Differential transmission response for samples 2705&2706 at 800nm (1.55eV) (b) Theoretical study for Density of States available for WSe_2, $PtSe_2$, and $MoSe_2$ adapted from ref. 103

On the other hand, Figure 7.46 (a) represents the THz response of the 2705 and 2706 samples for 400nm (3.09eV) photoexcitation. Sample 2705 resulted in higher THz conductivity, which could be due to the higher density of states available for this

excitation color, as seen in Figure 7.46 (b), as well as having 3 layers in total. As the figure suggests, the bandgap of 2706 is higher, and there is less available density of states, resulting in lower THz response. Also, $PtSe_2$ has a low density of states for this excitation color, and the sample's response is mainly $MoSe_2$, which has a higher density of states for 400nm.

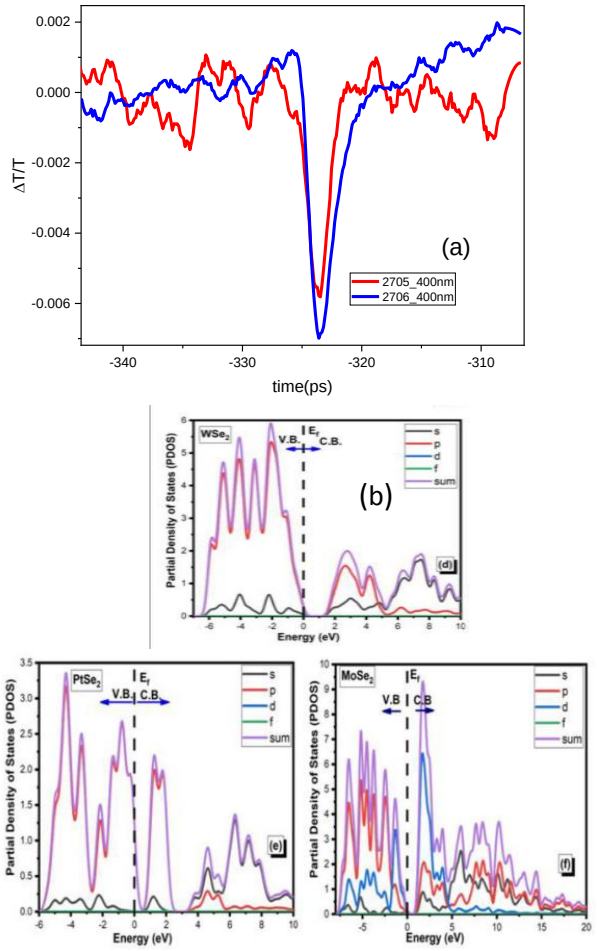

Figure 7.46 (a) Differential transmission response for samples 2705&2706 at 400nm (3.1eV) (b) Theoretical study for Density of States available for WSe2, PtSe2, and $MoSe_2$ adapted from ref. 103.

CHAPTER 8

CONCLUSION

In this thesis, three main topics were discussed. Firstly, optimization of the Terahertz systems was done in UNAM and TARLA facilities to improve the system's signal-to-noise ratios, and after successful optimization of the system at UNAM, installation of a new optical parametric amplifier along the beam path unfortunately changed the beam size and shape. Our initial attempts to recover were relatively unsuccessful. Therefore, the system was moved to an alternative facility, namely TARLA. The system was redesigned entirely according to the new beam and beam path properties, and system optimization studies were conducted. The achieved optimum S/N was improved one fold to greater than 10^4 for THz peak amplitude and bandwidth from ca. 2.5 THz to 4.5THz as compared to the previous UNAM setup.

Additionally, the samples were characterized by using THz-TDS. The single-layer graphene samples caused a ca. 4% THz signal insertion loss, whereas the multilayer samples caused a ca. 4% loss for each layer they have. The single and multilayer graphene samples and TMDC films were characterized in 0.1-3 THz for polymer substrates, 0.1-2 THz for semiconducting substrates, and 0.1-1.4 THz for Mica substrate. The polymer substrates had lower insertion loss than the semiconducting SiC and, Si/SiO_2 and quartz substrates.

Lastly, the THz conductivity behaviors of single-layer graphene samples on PET, PDMS and PMMA+PDMS, SiC, and Si/SiO_2, and multilayer graphene samples on quartz, PE, and PVC substrates, as well as TMDC films on mica substrates, were

analyzed. Single-layer graphene samples on polymer substrates showed metallic-like conductivity behavior with the longest lifetime for the PMMA+PDMS blend, even though it had the highest insertion loss due to its huge thickness compared to PET and PDMS substrates. The fast rise and decay responses of these graphene samples on polymer substrates make them suitable for high-speed applications requiring fast and reliable switching.

Single-layer graphene on a semiconducting SiC substrate resulted in a THz response, mainly dominated by the substrate. After subtracting the substrate response, the bare SLG sample exhibited a response similar to multilayer graphene, indicating there could be more than one layer of graphene or carrier doping from the interface layer or the substrate. The commercial single-layer graphene on Si/SiO_2 substrate also revealed a THz response, which is dominated by the substrate. The application of different fluences resulted in a greater sample response, also visible in the relative THz differential responses of the sample and the substrate. The subtraction of substrate response did not work well for the lowest fluence; however, the graphene response became more distinguishable with the increased fluence even though the total elimination of the substrate response was not possible. It could be concluded that semiconductor substrates are not good candidates for graphene thin film characterizations due to having their carrier responses, which tend to dominate the sample response. On the other hand, polymer substrates are good substrate candidates for their lowest insertion losses and superior surface properties, which could result in better-quality graphene.

The multilayer graphene samples on quartz and polymer substrates showed exceptional THz conductivities and carrier lifetimes >500ps. Their responses revealed a quick rise for the 400nm pump of around ~0.7ps on average and the 800nm pump a little longer as ~1.5ps on average. When corrected with their fluences, the resultant initial fast responses were almost the same for both pump colors. The

long-lived carriers, however, were in higher amounts for 400nm in general owing to their ability to excite to higher energy states and being more energetic. Therefore, the carriers gained the ability to move between the layers, tended to have longer mean free paths, and less recombination, leading to longer lifetimes. Also, the higher energy could foster the interlayer hopping of the carriers, that also causes less recombination and longer carrier lifetimes. The graphene samples of polymer substrates resulted in similar responses with their similar 30 and 32 layers of graphene. These multilayer graphene samples are good candidates for being utilized as an antenna material for THz generation, with their long-living charge carriers having high mobility.

The TMDC samples, on the other hand, revealed sharp and fast rise and fall times of around ~1ps. The first sample showed better THz conductivity for 800nm, whereas the second exhibited better THz conductivity for 400nm. The conductivity difference could be explained by their differences in the density of states. Their carrier lifetimes, however, are relatively short on the order of ~1ps, indicating probably less structural order on mica substrate. These TMDC samples are also good candidates for use as high-speed applications requiring fast and reliable switching.

The analyzed graphene and TMDC samples are good candidates for plasmonic antennas and fast response THz photodetectors, respectively, for their outstanding THz conductivity properties and quick rise and fall times.

REFERENCES

(1) Gupta, A.; Sakthivel, T.; Seal, S. Recent Development in 2D Materials beyond Graphene. *Prog. Mater. Sci.* **2015**, *73*, 44–126. https://doi.org/10.1016/j.pmatsci.2015.02.002.

(2) Zhang, S.; Ma, T.; Erdemir, A.; Li, Q. Tribology of Two-Dimensional Materials: From Mechanisms to Modulating Strategies. *Mater. Today* **2019**, *26* (June), 67–86. https://doi.org/10.1016/j.mattod.2018.12.002.

(3) Briggs, N.; Subramanian, S.; Lin, Z.; Li, X.; Zhang, X.; Zhang, K.; Xiao, K.; Geohegan, D.; Wallace, R.; Chen, L.-Q.; Terrones, M.; Ebrahimi, A.; Das, S.; Redwing, J.; Hinkle, C.; Momeni, K.; van Duin, A.; Crespi, V.; Kar, S.; Robinson, J. A. A Roadmap for Electronic Grade 2D Materials. *2D Mater.* **2019**, *6* (2), 022001. https://doi.org/10.1088/2053-1583/aaf836.

(4) Novoselov, K. S.; Mishchenko, A.; Carvalho, A.; Castro Neto, A. H. 2D Materials and van Der Waals Heterostructures. *Science (80-.).* **2016**, *353* (6298). https://doi.org/10.1126/science.aac9439.

(5) Ahn, E. C. 2D Materials for Spintronic Devices. *npj 2D Mater. Appl.* **2020**, *4* (1), 17. https://doi.org/10.1038/s41699-020-0152-0.

(6) Jayakumar, A.; Surendranath, A.; PV, M. 2D Materials for Next Generation Healthcare Applications. *Int. J. Pharm.* **2018**, *551* (1–2), 309–321. https://doi.org/10.1016/j.ijpharm.2018.09.041.

(7) Jeong, G. H.; Sasikala, S. P.; Yun, T.; Lee, G. Y.; Lee, W. J.; Kim, S. O. Nanoscale Assembly of 2D Materials for Energy and Environmental Applications. *Adv. Mater.* **2020**, *32* (35), 1–23. https://doi.org/10.1002/adma.201907006.

(8) Gopalan, P.; Sensale- Rodriguez, B. 2D Materials for Terahertz Modulation. *Adv. Opt. Mater.* **2020**, *8* (3), 1–23. https://doi.org/10.1002/adom.201900550.

(9) Aytekin, Y. S.; Köktürk, M.; Zaczek, A.; Korter, T. M.; Heilweil, E. J.; Esenturk, O. Optical Properties of Meloxicam in the Far-Infrared Spectral Region. *Chem. Phys.* **2018**, *512*, 36–43. https://doi.org/10.1016/j.chemphys.2018.04.022.

(10) Shi, J.; Li, Z.; Sang, D. K.; Xiang, Y.; Li, J.; Zhang, S.; Zhang, H. THz Photonics in Two Dimensional Materials and Metamaterials: Properties, Devices, and Prospects. *J. Mater. Chem. C* **2018**, *6* (6), 1291–1306. https://doi.org/10.1039/C7TC05460B.

(11) Mittendorff, M.; Winnerl, S.; Murphy, T. E. 2D THz Optoelectronics. *Adv. Opt. Mater.* **2021**, *9* (3), 1–30. https://doi.org/10.1002/adom.202001500.

(12) Gan, X.; Englund, D.; Van Thourhout, D.; Zhao, J. 2D Materials-Enabled Optical Modulators: From Visible to Terahertz Spectral Range. *Appl. Phys. Rev.* **2022**, *9* (2). https://doi.org/10.1063/5.0078416.

(13) Abohmra, A.; Khan, Z. U.; Abbas, H. T.; Shoaib, N.; Imran, M. A.; Abbasi, Q. H. Two-Dimensional Materials for Future Terahertz Wireless Communications. *IEEE Open J. Antennas Propag.* **2022**, *3* (January), 217–228. https://doi.org/10.1109/OJAP.2022.3143994.

(14) Chen, S.; Fan, F.; Miao, Y.; He, X.; Zhang, K.; Chang, S. Ultrasensitive Terahertz Modulation by Silicon-Grown MoS 2 Nanosheets. *Nanoscale* **2016**, *8* (8), 4713–4719. https://doi.org/10.1039/C5NR08101G.

(15) Yang, J.; Qin, H.; Zhang, K. Emerging Terahertz Photodetectors Based on Two-Dimensional Materials. *Opt. Commun.* **2018**, *406* (June 2017), 36–43.

https://doi.org/10.1016/j.optcom.2017.05.041.

(16) Wang, Y.; Wu, W.; Zhao, Z. Recent Progress and Remaining Challenges of 2D Material-Based Terahertz Detectors. *Infrared Phys. Technol.* **2019**, *102* (May), 103024. https://doi.org/10.1016/j.infrared.2019.103024.

(17) Basu, T.; Banerjee, A.; Vajandar, S. 2D Materials as THz Generators, Detectors, and Modulators: Potential Candidates for Biomedical Applications. In *Terahertz Biomedical and Healthcare Technologies*; Elsevier, 2020; pp 75–87. https://doi.org/10.1016/B978-0-12-818556-8.00004-5.

(18) Plusquellic, D. F.; Siegrist, K.; Heilweil, E. J.; Esenturk, O. Applications of Terahertz Spectroscopy in Biosystems. *ChemPhysChem* **2007**, *8* (17), 2412–2431. https://doi.org/10.1002/cphc.200700332.

(19) Woolard, D. L.; Brown, R.; Pepper, M.; Kemp, M. Terahertz Frequency Sensing and Imaging: A Time of Reckoning Future Applications? *Proc. IEEE* **2005**, *93* (10), 1722–1743. https://doi.org/10.1109/JPROC.2005.853539.

(20) Dhillon, S. S.; Vitiello, M. S.; Linfield, E. H.; Davies, A. G.; Hoffmann, M. C.; Booske, J.; Paoloni, C.; Gensch, M.; Weightman, P.; Williams, G. P.; Castro-Camus, E.; Cumming, D. R. S.; Simoens, F.; Escorcia-Carranza, I.; Grant, J.; Lucyszyn, S.; Kuwata-Gonokami, M.; Konishi, K.; Koch, M.; Schmuttenmaer, C. A.; Cocker, T. L.; Huber, R.; Markelz, A. G.; Taylor, Z. D.; Wallace, V. P.; Axel Zeitler, J.; Sibik, J.; Korter, T. M.; Ellison, B.; Rea, S.; Goldsmith, P.; Cooper, K. B.; Appleby, R.; Pardo, D.; Huggard, P. G.; Krozer, V.; Shams, H.; Fice, M.; Renaud, C.; Seeds, A.; Stöhr, A.; Naftaly, M.; Ridler, N.; Clarke, R.; Cunningham, J. E.; Johnston, M. B. The 2017 Terahertz Science and Technology Roadmap. *J. Phys. D. Appl. Phys.* **2017**,

50 (4). https://doi.org/10.1088/1361-6463/50/4/043001.

(21) Schmuttenmaer, C. A. Exploring Dynamics in the Far-Infrared with Terahertz Spectroscopy. *Chem. Rev.* **2004**, *104* (4), 1759–1780. https://doi.org/10.1021/cr020685g.

(22) Zouaghi, W.; Thomson, M. D.; Rabia, K.; Hahn, R.; Blank, V.; Roskos, H. G. Broadband Terahertz Spectroscopy: Principles, Fundamental Research and Potential for Industrial Applications. *Eur. J. Phys.* **2013**, *34* (6), S179–S199. https://doi.org/10.1088/0143-0807/34/6/S179.

(23) Ferguson, B.; Zhang, X.-C. Materials for Terahertz Science and Technology. *Nat. Mater.* **2002**, *1* (1), 26–33. https://doi.org/10.1038/nmat708.

(24) Yang, X.; Zhao, X.; Yang, K.; Liu, Y.; Liu, Y.; Fu, W.; Luo, Y. Biomedical Applications of Terahertz Spectroscopy and Imaging. *Trends Biotechnol.* **2016**, *34* (10), 810–824. https://doi.org/10.1016/j.tibtech.2016.04.008.

(25) Naftaly, M.; Miles, R. E. Terahertz Time-Domain Spectroscopy for Material Characterization. *Proc. IEEE* **2007**, *95* (8), 1658–1665. https://doi.org/10.1109/JPROC.2007.898835.

(26) Aytan, E.; Aytekin, Y. S.; Esenturk, O.; Kahraman, M. V. Fabrication and Characterization of Photocrosslinked Phase Change Materials Using Conventional and Terahertz Spectroscopy Techniques. *J. Energy Storage* **2019**, *26*, 100989. https://doi.org/10.1016/j.est.2019.100989.

(27) Shen, Y.-C. Terahertz Pulsed Spectroscopy and Imaging for Pharmaceutical Applications: A Review. *Int. J. Pharm.* **2011**, *417* (1–2), 48–60. https://doi.org/10.1016/j.ijpharm.2011.01.012.

(28) McIntosh, A. I.; Yang, B.; Goldup, S. M.; Watkinson, M.; Donnan, R. S. Terahertz Spectroscopy: A Powerful New Tool for the Chemical Sciences?

Chem. Soc. Rev. **2012**, *41* (6), 2072–2082. https://doi.org/10.1039/C1CS15277G.

(29) Kulesa, C. Terahertz Spectroscopy for Astronomy: From Comets to Cosmology. *IEEE Trans. Terahertz Sci. Technol.* **2011**, *1* (1), 232–240. https://doi.org/10.1109/TTHZ.2011.2159648.

(30) Konek, C.; Wilkinson, J.; Esenturk, O.; Heilweil, E.; Kemp, M. Terahertz Spectroscopy of Explosives and Simulants: RDX, PETN, Sugar, and L-Tartaric Acid. *Proc. SPIE* **2009**, *7311*, 73110K-1-73110K – 7. https://doi.org/10.1117/12.817913.

(31) Davies, A. G.; Burnett, A. D.; Fan, W.; Linfield, E. H.; Cunningham, J. E. Terahertz Spectroscopy of Explosives and Drugs. *Mater. Today* **2008**, *11* (3), 18–26. https://doi.org/10.1016/S1369-7021(08)70016-6.

(32) Leahy-Hoppa, M. R.; Fitch, M. J.; Osiander, R. Terahertz Spectroscopy Techniques for Explosives Detection. *Anal. Bioanal. Chem.* **2009**, *395* (2), 247–257. https://doi.org/10.1007/s00216-009-2803-z.

(33) Yu, L.; Hao, L.; Meiqiong, T.; Jiaoqi, H.; Wei, L.; Jinying, D.; Xueping, C.; Weiling, F.; Yang, Z. The Medical Application of Terahertz Technology in Non-Invasive Detection of Cells and Tissues: Opportunities and Challenges. *RSC Adv.* **2019**, *9* (17), 9354–9363. https://doi.org/10.1039/C8RA10605C.

(34) Xie, L.; Yao, Y.; Ying, Y. The Application of Terahertz Spectroscopy to Protein Detection: A Review. *Appl. Spectrosc. Rev.* **2014**, *49* (6), 448–461. https://doi.org/10.1080/05704928.2013.847845.

(35) Arik, E.; Altan, H.; Esenturk, O. Dielectric Properties of Ethanol and Gasoline Mixtures by Terahertz Spectroscopy and an Effective Method for Determination of Ethanol Content of Gasoline. *J. Phys. Chem. A* **2014**, *118*

(17), 3081–3089. https://doi.org/10.1021/jp500760t.

(36) Gowen, A. A.; O'Sullivan, C.; O'Donnell, C. P. Terahertz Time Domain Spectroscopy and Imaging: Emerging Techniques for Food Process Monitoring and Quality Control. *Trends Food Sci. Technol.* **2012**, *25* (1), 40–46. https://doi.org/10.1016/j.tifs.2011.12.006.

(37) Smith, R. M.; Arnold, M. A. Terahertz Time-Domain Spectroscopy of Solid Samples: Principles, Applications, and Challenges. *Appl. Spectrosc. Rev.* **2011**, *46* (8), 636–679. https://doi.org/10.1080/05704928.2011.614305.

(38) Borovkova, M.; Khodzitsky, M.; Demchenko, P.; Cherkasova, O.; Popov, A.; Meglinski, I. Terahertz Time-Domain Spectroscopy for Non-Invasive Assessment of Water Content in Biological Samples. *Biomed. Opt. Express* **2018**, *9* (5), 2266. https://doi.org/10.1364/BOE.9.002266.

(39) Theuer, M.; Harsha, S. S.; Molter, D.; Torosyan, G.; Beigang, R. Terahertz Time- Domain Spectroscopy of Gases, Liquids, and Solids. *ChemPhysChem* **2011**, *12* (15), 2695–2705. https://doi.org/10.1002/cphc.201100158.

(40) Molter, D.; Trierweiler, M.; Ellrich, F.; Jonuscheit, J.; Von Freymann, G. Interferometry-Aided Terahertz Time-Domain Spectroscopy. *Opt. Express* **2017**, *25* (7), 7547. https://doi.org/10.1364/OE.25.007547.

(41) van Exter, M.; Fattinger, C.; Grischkowsky, D. Terahertz Time-Domain Spectroscopy of Water Vapor. *Opt. Lett.* **1989**, *14* (20), 1128. https://doi.org/10.1364/ol.14.001128.

(42) Duvillaret, L.; Garet, F.; Coutaz, J.-L. Highly Precise Determination of Optical Constants and Sample Thickness in Terahertz Time-Domain Spectroscopy. *Appl. Opt.* **1999**, *38* (2), 409. https://doi.org/10.1364/AO.38.000409.

(43) Theuer, M.; Melinger, J. S. High-Resolution Waveguide Terahertz Time-Domain Spectroscopy. *J. Infrared, Millimeter, Terahertz Waves* **2011**, *32* (11), 1267–1284. https://doi.org/10.1007/s10762-011-9816-3.

(44) Molter, D.; Hübsch, D.; Sprenger, T.; Hens, K.; Nalpantidis, K.; Platte, F.; Torosyan, G.; Beigang, R.; Jonuscheit, J.; Freymann, G. von; Ellrich, F. Mail Inspection Based on Terahertz Time-Domain Spectroscopy. *Appl. Sci.* **2021**, *11* (3), 950. https://doi.org/10.3390/app11030950.

(45) Lane, P. A.; Cunningham, P. D.; Melinger, J. S.; Esenturk, O.; Heilweil, E. J. Hot Photocarrier Dynamics in Organic Solar Cells. *Nat. Commun.* **2015**, *6* (1), 7558. https://doi.org/10.1038/ncomms8558.

(46) Esenturk, O.; Melinger, J. S.; Heilweil, E. J. Terahertz Mobility Measurements on Poly-3-Hexylthiophene Films: Device Comparison, Molecular Weight, and Film Processing Effects. *J. Appl. Phys.* **2008**, *103* (2), 023102. https://doi.org/10.1063/1.2828028.

(47) Esenturk, O.; Melinger, J. S.; Lane, P. A.; Heilweil, E. J. Relative Photon-to-Carrier Efficiencies of Alternating Nanolayers of Zinc Phthalocyanine and C 60 Films Assessed by Time-Resolved Terahertz Spectroscopy. *J. Phys. Chem. C* **2009**, *113* (43), 18842–18850. https://doi.org/10.1021/jp904107x.

(48) Ulbricht, R.; Hendry, E.; Shan, J.; Heinz, T. F.; Bonn, M. Carrier Dynamics in Semiconductors Studied with Time-Resolved Terahertz Spectroscopy. *Rev. Mod. Phys.* **2011**, *83* (2), 543–586. https://doi.org/10.1103/RevModPhys.83.543.

(49) Lane, P. A.; Cunningham, P. D.; Melinger, J. S.; Kushto, G. P.; Esenturk, O.; Heilweil, E. J. Photoexcitation Dynamics in Films of C 60 and Zn Phthalocyanine with a Layered Nanostructure. *Phys. Rev. Lett.* **2012**, *108* (7), 1–5. https://doi.org/10.1103/PhysRevLett.108.077402.

(50) Němec, H.; Kužel, P.; Sundström, V. Charge Transport in Nanostructured Materials for Solar Energy Conversion Studied by Time-Resolved Terahertz Spectroscopy. *J. Photochem. Photobiol. A Chem.* **2010**, *215* (2–3), 123–139. https://doi.org/10.1016/j.jphotochem.2010.08.006.

(51) Savenije, T. J.; Kroeze, J. E.; Wienk, M. M.; Kroon, J. M.; Warman, J. M. Mobility and Decay Kinetics of Charge Carriers in Photoexcited PCBM/PPV Blends. *Phys. Rev. B* **2004**, *69* (15), 155205. https://doi.org/10.1103/PhysRevB.69.155205.

(52) Cabanillas-Gonzalez, J.; Virgili, T.; Gambetta, A.; Lanzani, G.; Anthopoulos, T. D.; de Leeuw, D. M. Photoinduced Transient Stark Spectroscopy in Organic Semiconductors: A Method for Charge Mobility Determination in the Picosecond Regime. *Phys. Rev. Lett.* **2006**, *96* (10), 106601. https://doi.org/10.1103/PhysRevLett.96.106601.

(53) Tsokkou, D.; Othonos, A.; Zervos, M. Carrier Dynamics and Conductivity of SnO 2 Nanowires Investigated by Time-Resolved Terahertz Spectroscopy. *Appl. Phys. Lett.* **2012**, *100* (13), 133101. https://doi.org/10.1063/1.3698097.

(54) Parkinson, P.; Lloyd-Hughes, J.; Gao, Q.; Tan, H. H.; Jagadish, C.; Johnston, M. B.; Herz, L. M. Transient Terahertz Conductivity of GaAs Nanowires. *Nano Lett.* **2007**, *7* (7), 2162–2165. https://doi.org/10.1021/nl071162x.

(55) Baxter, J. B.; Schmuttenmaer, C. A. Conductivity of ZnO Nanowires, Nanoparticles, and Thin Films Using Time-Resolved Terahertz Spectroscopy. *J. Phys. Chem. B* **2006**, *110* (50), 25229–25239. https://doi.org/10.1021/jp064399a.

(56) Baxter, J. B.; Guglietta, G. W. Terahertz Spectroscopy. *Anal. Chem.* **2011**,

83 (12), 4342–4368. https://doi.org/10.1021/ac200907z.

(57) Němec, H.; Kadlec, F.; Kužel, P. Methodology of an Optical Pump-Terahertz Probe Experiment: An Analytical Frequency-Domain Approach. *J. Chem. Phys.* **2002**, *117* (18), 8454–8466. https://doi.org/10.1063/1.1512648.

(58) Blanchard, F.; Razzari, L.; Bandulet, H.; Sharma, G.; Morandotti, R.; Kieffer, J. C.; Ozaki, T.; Reid, M.; Tiedje, H. F.; Haugen, H. K.; Hegmann, F. A. Generation of 1.5 MJ Single-Cycle Terahertz Pulses by Optical Rectification from a Large Aperture ZnTe Crystal. *Opt. Express* **2007**, *15* (20), 13212. https://doi.org/10.1364/OE.15.013212.

(59) Esh, A.; Soltani, A.; Shahabadi, M. Terahertz Detection Using Electro-Optic Effect in a ZnTe Layered Structure. In *2009 First Conference on Millimeter-Wave and Terahertz Technologies (MMWaTT)*; IEEE, 2009; pp 50–52. https://doi.org/10.1109/MMWATT.2009.5450454.

(60) Wang, X.; Song, Z.; Wen, W.; Liu, H.; Wu, J.; Dang, C.; Hossain, M.; Iqbal, M. A.; Xie, L. Potential 2D Materials with Phase Transitions: Structure, Synthesis, and Device Applications. *Adv. Mater.* **2019**, *31* (45). https://doi.org/10.1002/adma.201804682.

(61) Peng, B.; Zhang, Q.; Zhang, Y.; Zhao, Y.; Hou, S.; Yang, Y.; Dai, F.; Yi, R.; Chen, R.; Wang, J.; Zhang, L.; Chen, L.; Zhang, S.; Fang, H. Unexpected Piezoresistive Effect, Room- Temperature Ferromagnetism, and Thermal Stability of 2D B- CuI Crystals in Reduced Graphene Oxide Membrane. *Adv. Electron. Mater.* **2023**, *9* (5). https://doi.org/10.1002/aelm.202201241.

(62) Butler, S. Z.; Hollen, S. M.; Cao, L.; Cui, Y.; Gupta, J. A.; Gutiérrez, H. R.; Heinz, T. F.; Hong, S. S.; Huang, J.; Ismach, A. F.; Johnston-Halperin, E.; Kuno, M.; Plashnitsa, V. V; Robinson, R. D.; Ruoff, R. S.; Salahuddin, S.;

Shan, J.; Shi, L.; Spencer, M. G.; Terrones, M.; Windl, W.; Goldberger, J. E. Progress, Challenges, and Opportunities in Two-Dimensional Materials Beyond Graphene. *ACS Nano* **2013**, *7* (4), 2898–2926. https://doi.org/10.1021/nn400280c.

(63) Wang, L.; Zhao, X.; Lv, D.; Liu, C.; Lai, W.; Sun, C.; Su, Z.; Xu, X.; Hao, W.; Dou, S. X.; Du, Y. Promoted Photocharge Separation in 2D Lateral Epitaxial Heterostructure for Visible- Light- Driven CO 2 Photoreduction. *Adv. Mater.* **2020**, *32* (48). https://doi.org/10.1002/adma.202004311.

(64) Blonsky, M. N.; Zhuang, H. L.; Singh, A. K.; Hennig, R. G. Ab Initio Prediction of Piezoelectricity in Two-Dimensional Materials. *ACS Nano* **2015**, *9* (10), 9885–9891. https://doi.org/10.1021/acsnano.5b03394.

(65) Shanmugam, V.; Mensah, R. A.; Babu, K.; Gawusu, S.; Chanda, A.; Tu, Y.; Neisiany, R. E.; Försth, M.; Sas, G.; Das, O. A Review of the Synthesis, Properties, and Applications of 2D Materials. *Part. Part. Syst. Charact.* **2022**, *39* (6). https://doi.org/10.1002/ppsc.202200031.

(66) Bonaccorso, F.; Sun, Z.; Hasan, T.; Ferrari, A. C. Graphene Photonics and Optoelectronics. *Nat. Photonics* **2010**, *4* (9), 611–622. https://doi.org/10.1038/nphoton.2010.186.

(67) Novoselov, K. S.; Geim, A. K.; Morozov, S. V; Jiang, D.; Katsnelson, M. I.; Grigorieva, I. V; Dubonos, S. V; Firsov, A. A. Two-Dimensional Gas of Massless Dirac Fermions in Graphene. *Nature* **2005**, *438* (7065), 197–200. https://doi.org/10.1038/nature04233.

(68) Ryzhii, V.; Ryzhii, M.; Mitin, V.; Otsuji, T. Toward the Creation of Terahertz Graphene Injection Laser. *J. Appl. Phys.* **2011**, *110* (9). https://doi.org/10.1063/1.3657853.

(69) Schwierz, F. Graphene Transistors. *Nat. Nanotechnol.* **2010**, *5* (7), 487–496. https://doi.org/10.1038/nnano.2010.89.

(70) Mueller, T.; Xia, F.; Avouris, P. Graphene Photodetectors for High-Speed Optical Communications. *Nat. Photonics* **2010**, *4* (5), 297–301. https://doi.org/10.1038/nphoton.2010.40.

(71) Ryzhii, V.; Ryabova, N.; Ryzhii, M.; Baryshnikov, N.; Karasik, V.; Mitin, V.; Otsuji, T. Terahertz and Infrared Photodetectors Based on Multiple Graphene Layer and Nanoribbon Structures. *Opto-Electronics Rev.* **2012**, *20* (1), 15–25. https://doi.org/10.2478/s11772-012-0009-y.

(72) Ryzhii, M.; Ryzhii, V. Injection and Population Inversion in Electrically Induced p–n Junction in Graphene with Split Gates. *Jpn. J. Appl. Phys.* **2007**, *46* (3L), L151. https://doi.org/10.1143/JJAP.46.L151.

(73) Yadav, D.; Boubanga-Tombet, S.; Satou, A.; Tamamushi, G.; Watanabe, T.; Suemitsu, T.; Fukidome, H.; Suemitsu, M.; Duvinov, A. A.; Popov, V. V.; Ryzhii, M.; Mitin, V.; Shur, M. S.; Ryzhii, V.; Otsuji, T. Graphene-Based 2D-Heterostructures for Terahertz Lasers and Amplifiers. In *Terahertz, RF, Millimeter, and Submillimeter-Wave Technology and Applications XII*; Sadwick, L. P., Yang, T., Eds.; SPIE, 2019; Vol. 10917, p 15. https://doi.org/10.1117/12.2516494.

(74) Sensale-Rodriguez, B.; Yan, R.; Kelly, M. M.; Fang, T.; Tahy, K.; Hwang, W. S.; Jena, D.; Liu, L.; Xing, H. G. Broadband Graphene Terahertz Modulators Enabled by Intraband Transitions. *Nat. Commun.* **2012**, *3* (1), 780. https://doi.org/10.1038/ncomms1787.

(75) Kakenov, N.; Balci, O.; Takan, T.; Ozkan, V. A.; Altan, H.; Kocabas, C. Observation of Gate-Tunable Coherent Perfect Absorption of Terahertz Radiation in Graphene. *ACS Photonics* **2016**, *3* (9), 1531–1535.

https://doi.org/10.1021/acsphotonics.6b00240.

(76) Sangwan, V. K.; Hersam, M. C. Electronic Transport in Two-Dimensional Materials. *Annu. Rev. Phys. Chem.* **2018**, *69* (1), 299–325. https://doi.org/10.1146/annurev-physchem-050317-021353.

(77) Han, P.; Wang, X.; Zhang, Y. Time- Resolved Terahertz Spectroscopy Studies on 2D Van Der Waals Materials. *Adv. Opt. Mater.* **2020**, *8* (3). https://doi.org/10.1002/adom.201900533.

(78) Koppens, F. H. L.; Chang, D. E.; García de Abajo, F. J. Graphene Plasmonics: A Platform for Strong Light–Matter Interactions. *Nano Lett.* **2011**, *11* (8), 3370–3377. https://doi.org/10.1021/nl201771h.

(79) Low, T.; Avouris, P. Graphene Plasmonics for Terahertz to Mid-Infrared Applications. *ACS Nano* **2014**, *8* (2), 1086–1101. https://doi.org/10.1021/nn406627u.

(80) García de Abajo, F. J. Graphene Plasmonics: Challenges and Opportunities. *ACS Photonics* **2014**, *1* (3), 135–152. https://doi.org/10.1021/ph400147y.

(81) Zheng, B.; Yang, X.; Li, J.; Shi, C.-F.; Wang, Z.-L.; Xia, X.-H. Graphene Plasmon-Enhanced IR Biosensing for in Situ Detection of Aqueous-Phase Molecules with an Attenuated Total Reflection Mode. *Anal. Chem.* **2018**, *90* (18), 10786–10794. https://doi.org/10.1021/acs.analchem.8b01715.

(82) Ye, T.; Wang, B.; Wang, C.; Li, Z.; Zhang, Z.; Jin, K.; Wang, L.; Yin, Y. Approaching the Intrinsic Lifetime and Modulating a Graphene Plasmonic Resonance at a Few Hundred GHz. *Adv. Opt. Mater.* **2019**, *7* (11), 1900315. https://doi.org/10.1002/adom.201900315.

(83) Chen, M.; Fan, F.; Yang, L.; Wang, X.; Chang, S.-J. Tunable Terahertz Amplifier Based on Slow Light Edge Mode in Graphene Plasmonic Crystal.

IEEE J. Quantum Electron. **2017**, *53* (1), 1–6. https://doi.org/10.1109/JQE.2016.2640220.

(84) Hwang, C.; Siegel, D. A.; Mo, S.-K.; Regan, W.; Ismach, A.; Zhang, Y.; Zettl, A.; Lanzara, A. Fermi Velocity Engineering in Graphene by Substrate Modification. *Sci. Rep.* **2012**, *2* (1), 590. https://doi.org/10.1038/srep00590.

(85) Hwang, C.; Siegel, D. A.; Mo, S.-K.; Regan, W.; Ismach, A.; Zhang, Y.; Zettl, A.; Lanzara, A. Fermi Velocity Engineering in Graphene by Substrate Modification. *Sci. Rep.* **2012**, *2* (1), 590. https://doi.org/10.1038/srep00590.

(86) Dawlaty, J. M.; Shivaraman, S.; Chandrashekhar, M.; Rana, F.; Spencer, M. G. Measurement of Ultrafast Carrier Dynamics in Epitaxial Graphene. *Appl. Phys. Lett.* **2008**, *92* (4), 042116. https://doi.org/10.1063/1.2837539.

(87) Strait, J. H.; Wang, H.; Shivaraman, S.; Shields, V.; Spencer, M.; Rana, F. Very Slow Cooling Dynamics of Photoexcited Carriers in Graphene Observed by Optical-Pump Terahertz-Probe Spectroscopy. *Nano Lett.* **2011**, *11* (11), 4902–4906. https://doi.org/10.1021/nl202800h.

(88) Zhou, B.; Rasmussen, M.; Whelan, P. R.; Ji, J.; Shivayogimath, A.; Bøggild, P.; Jepsen, P. U. Non-Linear Conductivity Response of Graphene on Thin-Film PET Characterized by Transmission and Reflection Air-Plasma THz-TDS. *Sensors* **2023**, *23* (7), 3669. https://doi.org/10.3390/s23073669.

(89) Mics, Z.; Tielrooij, K.-J.; Parvez, K.; Jensen, S. A.; Ivanov, I.; Feng, X.; Müllen, K.; Bonn, M.; Turchinovich, D. Thermodynamic Picture of Ultrafast Charge Transport in Graphene. *Nat. Commun.* **2015**, *6* (1), 7655. https://doi.org/10.1038/ncomms8655.

(90) Cinquanta, E.; Pogna, E. A. A.; Gatto, L.; Stagira, S.; Vozzi, C. Charge Carrier Dynamics in 2D Materials Probed by Ultrafast THzspectroscopy.

Adv. Phys. X **2023**, *8* (1). https://doi.org/10.1080/23746149.2022.2120416.

(91) Liu, Z.; Jiang, L.; Zheng, Y. Conductivity Tensor of Graphene Dominated by Spin-Orbit Coupling Scatterers: A Comparison between the Results from Kubo and Boltzmann Transport Theories. *Sci. Rep.* **2016**, *6* (1), 23762. https://doi.org/10.1038/srep23762.

(92) Jabbarzadeh, F.; Heydari, M.; Habibzadeh-Sharif, A. A Comparative Analysis of the Accuracy of Kubo Formulations for Graphene Plasmonics. *Mater. Res. Express* **2019**, *6* (8), 086209. https://doi.org/10.1088/2053-1591/ab1e02.

(93) Falkovsky, L. A. Optical Properties of Graphene. *J. Phys. Conf. Ser.* **2008**, *129*, 012004. https://doi.org/10.1088/1742-6596/129/1/012004.

(94) Kaya, E. Construction of Terahertz Spectrometers And Their Use In Characterization of Conductivities And Modulation Behaviors of Graphene Layers, Middle East Technical University, 2017, Vol. 549.

(95) Sorokin, E. Solid-State Materials for Few-Cycle Pulse Generation and Amplification; 2004; Vol. 73, pp 3–73. https://doi.org/10.1007/978-3-540-39849-3_1.

(96) Fedorov, P. P.; Kokh, A. E.; Kononova, N. G. Barium Borate β-BaB 2 O 4 as a Material for Nonlinear Optics. *Russ. Chem. Rev.* **2002**, *71* (8), 651–671. https://doi.org/10.1070/RC2002v071n08ABEH000716.

(97) BBO crystal_Thorlabs https://www.thorlabs.com/newgrouppage9.cfm?objectgroup_id=15444.

(98) Nair, R. R.; Blake, P.; Grigorenko, A. N.; Novoselov, K. S.; Booth, T. J.; Stauber, T.; Peres, N. M. R.; Geim, A. K. Fine Structure Constant Defines Visual Transparency of Graphene. *Science (80-.).* **2008**, *320* (5881), 1308–

1308. https://doi.org/10.1126/science.1156965.

(99) Jnawali, G.; Rao, Y.; Yan, H.; Heinz, T. F. Observation of a Transient Decrease in Terahertz Conductivity of Single-Layer Graphene Induced by Ultrafast Optical Excitation. *Nano Lett.* **2013**, *13* (2), 524–530. https://doi.org/10.1021/nl303988q.

(100) Emtsev, K. V; Zakharov, A. A.; Coletti, C.; Forti, S.; Starke, U. Ambipolar Doping in Quasifree Epitaxial Graphene on SiC(0001) Controlled by Ge Intercalation. *Phys. Rev. B* **2011**, *84* (12), 125423. https://doi.org/10.1103/PhysRevB.84.125423.

(101) Goniszewski, S.; Adabi, M.; Shaforost, O.; Hanham, S. M.; Hao, L.; Klein, N. Correlation of P-Doping in CVD Graphene with Substrate Surface Charges. *Sci. Rep.* **2016**, *6* (1), 22858. https://doi.org/10.1038/srep22858.

(102) George, P. A.; Strait, J.; Dawlaty, J.; Shivaraman, S.; Chandrashekhar, M.; Rana, F.; Spencer, M. G. Ultrafast Optical-Pump Terahertz-Probe Spectroscopy of the Carrier Relaxation and Recombination Dynamics in Epitaxial Graphene. *Nano Lett.* **2008**, *8* (12), 4248–4251. https://doi.org/10.1021/nl8019399.

(103) Jameel, M. H.; Roslan, M. S. bin; Mayzan, M. Z. H. Bin; Shaaban, I. A.; Rizvi, S. Z. H.; Agam, M. A. Bin; Saleem, S.; Assiri, M. A. A Comparative DFT Study of Bandgap Engineering and Tuning of Structural, Electronic, and Optical Properties of 2D WS2, PtS2, and MoS2 between WSe2, PtSe2, and MoSe2 Materials for Photocatalytic and Solar Cell Applications. *J. Inorg. Organomet. Polym. Mater.* **2023**, No. 0123456789. https://doi.org/10.1007/s10904-023-02828-0.

(104) Oum, K.; Lenzer, T.; Scholz, M.; Jung, D. Y.; Sul, O.; Cho, B. J.; Lange, J.; Müller, A. Observation of Ultrafast Carrier Dynamics and Phonon

Relaxation of Graphene from the Deep-Ultraviolet to the Visible Region. *J. Phys. Chem. C* **2014**, *118* (12), 6454–6461. https://doi.org/10.1021/jp4072197.

(105) Auty, A. J.; Mansouriboroujeni, N.; Nagaraja, T.; Chekulaev, D.; Sorensen, C. M.; Das, S. R.; Martsinovich, N.; Chauvet, A. A. P. Ultrafast Transient Absorption Spectroscopy of Inkjet-Printed Graphene and Aerosol Gel Graphene Films: Effect of Oxygen and Morphology on Carrier Relaxation Dynamics. *J. Phys. Chem. C* **2022**, *126* (18), 7949–7955. https://doi.org/10.1021/acs.jpcc.2c01086.

(106) Winnerl, S.; Göttfert, F.; Mittendorff, M.; Schneider, H.; Helm, M.; Winzer, T.; Malic, E.; Knorr, A.; Orlita, M.; Potemski, M.; Sprinkle, M.; Berger, C.; de Heer, W. A. Time-Resolved Spectroscopy on Epitaxial Graphene in the Infrared Spectral Range: Relaxation Dynamics and Saturation Behavior. *J. Phys. Condens. Matter* **2013**, *25* (5), 054202. https://doi.org/10.1088/0953-8984/25/5/054202.

(107) Lane, P. A.; Cunningham, P. D.; Melinger, J. S.; Esenturk, O.; Heilweil, E. J. Hot Photocarrier Dynamics in Organic Solar Cells. *Nat. Commun.* **2015**, *6*, 7558. https://doi.org/10.1038/ncomms8558.

(108) Frenzel, A. J.; Lui, C. H.; Fang, W.; Nair, N. L.; Herring, P. K.; Jarillo-Herrero, P.; Kong, J.; Gedik, N. Observation of Suppressed Terahertz Absorption in Photoexcited Graphene. *Appl. Phys. Lett.* **2013**, *102* (11), 113111. https://doi.org/10.1063/1.4795858.

(109) Shang, J.; Luo, Z.; Cong, C.; Lin, J.; Yu, T.; Gurzadyan, G. G. Femtosecond UV-Pump/Visible-Probe Measurements of Carrier Dynamics in Stacked Graphene Films. *Appl. Phys. Lett.* **2010**, *97* (16). https://doi.org/10.1063/1.3504704.

(110) Docherty, C. J.; Parkinson, P.; Joyce, H. J.; Chiu, M.-H.; Chen, C.-H.; Lee, M.-Y.; Li, L.-J.; Herz, L. M.; Johnston, M. B. Ultrafast Transient Terahertz Conductivity of Monolayer MoS 2 and WSe 2 Grown by Chemical Vapor Deposition. *ACS Nano* **2014**, *8* (11), 11147–11153. https://doi.org/10.1021/nn5034746.

(111) Pavoni, E.; Mohebbi, E.; Zampa, G. M.; Stipa, P.; Pierantoni, L.; Laudadio, E.; Mencarelli, D. First Principles Study of WSe 2 and the Effect of V Doping on the Optical and Electronic Properties. *Mater. Adv.* **2024**, *5* (6), 2230–2237. https://doi.org/10.1039/D3MA00940H.

CURRICULUM VITAE

Surname, Name: Aytekin, Yusuf Samet

EDUCATION

Degree	Institution	Year of Graduation
MS	METU Chemistry	2016
BS	METU Chemistry	2013
High School	Halide Edip High School, Ankara	2008

FOREIGN LANGUAGES

Advanced English, Beginner German

PUBLICATIONS

1. Aytekin, Y. S., Köktürk, M. & Esenturk, O. Analysis of active pharmaceutical ingredients by terahertz spectroscopy. NATO Science for Peace and Security Series B: Physics and Biophysics vol. PartF1 (2017).

2. Aytekin, Y. S. et al. Optical properties of Meloxicam in the far-infrared spectral region. Chem. Phys. 512, 36–43 (2018).

3. Aytan, E., Aytekin, Y. S., Esenturk, O. & Kahraman, M. V. Fabrication and characterization of photocrosslinked phase change materials by using conventional and terahertz spectroscopy techniques. J. Energy Storage 26, 100989 (2019).

4. Aytan, E., Aytekin, Y. S., Akbal Aytan, T., Esenturk, O. & Kahraman, M. V. Facile application of terahertz spectroscopy in UV-coated and phase change material loaded MPS. Polym. Bull. 81, 2447–2464 (2024)

Aikido, Running, Accordion, Chess, Camping, Bicycle, Trekking